



**STRUCTURAL COMPOSITION AND MECHANICAL
PERFORMANCES OF POLY (VINYL ALCOHOL)
MATERIALS: EXPERIMENTAL AND MOLECULAR
DYNAMICS SIMULATION STUDIES**

A Thesis submitted by

Lujuan Li, MEng

For the award of
Doctor of philosophy

2021

ABSTRACT

The addition of small molecules can significantly influence the macroscopic mechanical property and microscopic chain dynamics of poly(vinyl alcohol) (PVA) materials. However, to date the mechanical mechanism behind remains not well understood experimentally and theoretically. The goal of this work is to gain an in-depth understanding of the effects of structures and content of small molecules on physical structures and dynamics properties of PVA composites by a combined use of molecular dynamics (MD) simulation and experimental methods. Three kinds of small molecules are assessed: water, 2,4,5,6-tetraaminopyrimidine (4N-2456), and phytic acid (PA).

First, we systematically examine the governing effect of water content on the mechanical property, glass transition, free volume, and intermolecular interactions by combining experimental and MD simulation. Our results show that the presence of water significantly reduces the mechanical strength of PVA, and only 1.8 wt% of water reduces the tensile strength by $\sim 32\%$ but notably increases the plasticity of PVA by ~ 2.5 times. Meanwhile, the inclusion of water remarkably lowers the glass transition temperature, increases free volume, and promotes the relaxation and mobility of PVA chains. This is mainly because the presence of water gives rise to both the plasticization and even lubricating effect on the PVA chains. This work unravels how water governs the mechanical performances of the PVA.

Then, we study the hydrogen-bond cross-linking effect of 4N-2456 molecules on the structure, chain dynamics and mechanical properties of the PVA matrix. It is found that the addition of 4N-2456 leads to a nonlinear decrease of the free volume of PVA. A critical concentration about 5.0 wt% is identified, resulting in the formation of 4N-2456 clusters. At this concentration, the PVA chains show a relatively slow mobility, a higher glass transition temperature and higher elastic

modulus. A further increase in the 4N-2456 concentration leads to aggregation, and conversely weakens the hydrogen-bond interactions between PVA chains. Our work offers an understanding of how the 4N-2456 molecules influence the PVA chain dynamics and mechanical properties of the PVA matrix on molecular level.

Finally, we explore the structure, chain dynamics and mechanical properties of PVA/PA composite films showing a certain antibacterial capability by combining MD simulation and experimental investigations. We show that the addition of 10 wt% PA endows PVA with a good antibacterial capability. The number of PVA-PA H-bonds per PA molecule and that of total H-bonds show different PA content dependence. The PVA composite film containing 1.9 wt% of PA shows a lower free volume and a smaller diffusion coefficient, and the highest strength and ductility. Meanwhile, the glass transition temperature (T_g) of PVA reaches the maximum value at ca. 1.25 wt% of PA. This work reveals how small molecules affect structure and mechanical properties of polymers and contributes to expanding practical applications of PVA/PA in many industrial sectors (e.g., packaging).

This work offers an in-depth understanding of how small molecules affect physical structure and mechanical properties of polymers through intermolecular interactions between small molecules and the polymer matrix. This work is expected to contribute to the creation of mechanically strong, tough and ductile polymeric materials, ultimately expanding the real-world applications of polymers in industries.

CERTIFICATION OF THESIS

This Thesis is the work of Lujuan Li except where otherwise acknowledged, with the majority of the authorship of the papers presented as a Thesis by Publication undertaken by the Student. The work is original and has not previously been submitted for any other award, except where acknowledged.

Principal Supervisor: Hao Wang

Associate Supervisor: Pingan Song

Associate Supervisor: Chuncheng Zuo

Student and supervisors' signatures of endorsement are held at the University.

ACKNOWLEDGEMENTS

I would like to thank all our present and former colleagues, who helped me in one way or another to finish this work.

First, I would like to thank these people especially my principal supervisor Dr. Hao Wang and associate professor Dr. Pingan Song. They have provided guidance and always made the time for discussions whenever I needed assistance. They always worked energetically and gave me much encouragement to explore the research problem.

I am greatly indebted to Mr. Xiaodong Xu from Zhejiang A& F University. His assistance in experiment made me confident with my research. Our family gave me a tremendous support during this endeavor. Many thanks to Chuncheng Zuo and Zhiguang Xu who provided the computational resource to complete this thesis. I'd like to thank Zhengping Fang from NingboTech University and Lei Liu from the University of Southern Queensland for their time and support in proofreading this thesis. Xin Qiao and Yang Yang has freely given their time to contribute to many suggestions of this thesis. Special thanks to my son Lulin Cao who always made me relax with his innocent smile. Many thanks to my husband who always support me during my research. I thank the people who reviewed the manuscript for their suggestions. I would like to thank the financial support through the USQ Jiaying University Postgraduate Research Scholarship during my research.

Finally, I want to thank my coworkers and friends in our team. They made the time for discussion and I have gain confidence in my research.

PUBLICATIONS DURING CANDIDATURE

1. **L. Li**, X. Xu, L. Liu, P. Song, Q. Cao, Z. Xu, Z. Fang, H. Wang, Water governs the mechanical properties of poly(vinyl alcohol). *Polymer*, 2021, 213, 123330.
2. **L. Li**, X. Xu, P. Song, Q. Cao, X. Qiao, Z. Xu, Y. Yang, C. Zuo, H. Wang, Insights into the hydrogen-bond cross-linking effects of small multiamine molecules on physical and mechanical properties of poly(vinly alcohol) by molecular dynamics simulations. *Modelling and Simulation in Materials Science and Engineering*, 2021, 29, 035012 .
3. **L. Li**, X. Xu, B. Wang, P. Song, Q. Cao, Y. Yang, Z. Xu, H. Wang, Structure, chain dynamics and mechanical properties of transparent and antibacterial poly(vinyl alcohol)/phytic acid composite films. *Composites Communications*, 2021, under review.

TABLE OF CONTENTS

ABSTRACT.....	i
CERTIFICATION OF THESIS.....	iii
ACKNOWLEDGEMENTS	iv
PUBLICATIONS DURING CANDIDATURE	v
TABLE OF CONTENTS	vi
LIST OF FIGURES.....	x
LIST OF TABLES.....	xiv
LIST OF ABBREVIATIONS.....	xv
LIST OF SYMBOLS	xvii
CHAPTER 1: INTRODUCTION	1
1.1 Background and research motivation.....	1
1.2 Research gaps	3
1.3 Problem statement	3
1.4 Research aim	4
1.5 Research objectives	4
1.6 Significance of research	4
1.7 Research scope	5
1.8 Thesis outline.....	5
CHAPTER 2: LITERATURE REVIEW	8
2.1 Introduction	8
2.2 Methods of creating PVA based nanocomposite	10
2.2.1 Nanofiller.....	10

2.2.2 Electron beam or γ -radiation	12
2.2.3 Freezing/thawing alternation	13
2.2.4 Hydrogen-bond cross-linking	13
2.4 Molecular dynamics simulation of PVA.....	20
2.5 Calculation of mechanical properties	23
2.6 Identified research limitations	24
 CHAPTER 3: WATER GOVERNS THE MECHANICAL PROPERTIES OF POLY(VINYL ALCOHOL).....	
3.1 Introduction	26
3.2 Experimental	29
3.2.1 Raw Materials.....	29
3.2.2 Fabrication of PVA films	31
3.2.3 Characterizations	32
3.2.4 Molecular Dynamics Simulations.....	35
3.2.5 Establishment of Initial Model Systems	36
3.2.6 Calculation of Properties	37
3.3 Results and discussions	38
3.3.1 Experimental design	38
3.3.2 Mechanical performances.....	41
3.3.3 Glass transition temperatures and free volume	46
3.3.4 Relaxation and Dynamics of PVA chains	51
3.3.5 Intermolecular interactions and interchain distances	59
3.4 Conclusions	63
 CHAPTER 4: INSIGHTS INTO THE HYDROGEN-BOND CROSS-LINKING EFFECTS OF SMALL MULTIAMINE MOLECULES ON PHYSICAL AND MECHANICAL PROPERTIES OF POLY(VINYL ALCOHOL) BY MOLECULAR D	

YNAMICS SIMULATIONS.....	65
4.1 Introduction	65
4.2 Simulation Methods	68
4.2.1 Preparation of initial model system	68
4.2.2 Molecular dynamics simulations	69
4.2.3 Calculation of properties	70
4.3 Results and Discussion	72
4.3.1 H-bond interactions	72
4.3.2 Free volume	73
4.3.3 Mobility of PVA chains	77
4.3.4 Glass transition temperature	82
4.3.5 Mechanical performances	85
4.4 Conclusions	86
 CHAPTER 5: STRUCTURE, CHAIN DYNAMICS AND MECHANICAL PRO PERTIES OF TRANSPARENT AND ANTIBACTERIAL POLY(VINYL ALC OHOL)/PHYTIC ACID COMPOSITE FILMS.....	88
5.1 Introduction	88
5.2 Experimental	90
5.3 Results and Discussion	95
5.3.1 Optical and Antibacterial Properties	95
5.3.2 HB Interactions between PVA and PA	95
5.3.3 Structure and chain dynamics	100
5.3.4 Mechanical properties.....	108
5.4 Conclusions	112
 CHAPTER 6: CONCLUSIONS AND FUTURE RESEARCH	114
6.1 Conclusion.....	114
6.2 Future research	115

REFERENCES.....	118
APPENDIX A	136
APPENDIX B	164

LIST OF FIGURES

Figure 2.1 Molecular structure of PVA	9
Figure 2.2 View of the interaction between PVA and ND	11
Figure 2.3 Schematic illustration of the chain scission induced by electron beam	12
Figure 2.4 Schematic illustration of crosslinking PVA formed by freezing and thawing way	13
Figure 2.5 Structure evolution of the hierarchical spider silk from macroscopic to nanoscopic.....	14
Figure 2.6 (a) Graphene oxide paper added with H ₂ O and (b) graphene oxide paper grafted with PVA.....	16
Figure 2.7 The variation of storage modulus with time and water content in experiment and simulation	17
Figure 2.8 (a) The improved Young's modulus, strain and stress of the PVA hybrid melamine composite (b) schematic representation of interactions between Melamine and PVA.	18
Figure 2.9 (a) Snapshot of the creation of the hydrogen bond network by mixing small multiamines and (b) the curve of tensile stress-strain	19
Figure 3.1 Representative tensile curves of the PVA films redrawn according to the work published previously	30
Figure 3.2 (a) illustration for the preparation of PVA films with control water content, and (b) models for molecular dynamic simulation of the PVA/water binary system.....	31
Figure 3.3 (a) Typical tensile stress-strain curves, (b) tensile strength, (c) elastic modulus, and (d) strain at failure of PVA films with varied water content (ϕ)....	40
Figure 3.4 (a) The first heating cycle of PVA with various water content, and the	

experimental, simulated and theoretical (b) Tg values, and (c) of FFV of PVA as a function of water content.	44
Figure 3.5 Snapshots of FFV for PVA with various water contentswater content calculated by MD simulation. (a) PVA, (b) PVA-1.0, (c) PVA-2.5, (d) PVA-5.0, (e) PVA-10, (f) PVA-15, (g) PVA-20, and (h) PVA-30. (The blue cloud and gray cloud represent the outside or free volume	45
Figure 3.6 Frequency dependence of (a) storage modulus (G') and (b) loss factor (tanδ) at 25 oC for PVA films with varied water content.....	50
Figure 3.7 MSD as functions of simulation time for (a) PVA and (b) water and (c) their diffusion coefficient (D) at 300 K.....	54
Figure 3.8 Snapshots of MD simulation showing the motion trajectory of extracted PVA chains from (a) PVA-1.0 and (b) PVA-10 after 1ps, 99 ps and 197 ps. One PVA chain is marked in yellow with one carbon atom and highlighted in dark blue for showing the movement of PVA chains. The three numbers in the brackets refer to x, y and z coordinates of the marked carbon atom, respectively.	55
Figure 3.9 H-bond interactions between PVA and water. (a) ATR-IR spectra, (b) relative H-bond density for PVA films as a function of water content. (c) Experimental and (d) simulated (at 300 K) changes in the number (#) of different H-bonds of PVA films as a function of water content.....	56
Figure 3.10 Illustration of dominant H-bond interactions in the PVA with increasing water content.....	57
Figure 3.11 Radial distribution functions (RDFs) of samples with various water content showing intermolecular distance for (a) $g_{C-C}(r)$ between PVA chains, (b) $g_{H-O}(r)$ between PVA chains and water molecules and (c) the interaction between water and PVA.....	58
Figure 4.1 Molecular models for the simulations of PVA/4N-2456 composites.	68
Figure 4.2 Number of H-bonds as a function of the 4N-2456 concentration at 300	

K.....	72
Figure 4.3 Schematic of the method of drawing a Connolly surface with radius R_p . The atoms are represented as hard spheres with vdW radius.....	74
Figure 4.4 Fraction of free volume of the composite system as a function of the 4N-2456 concentration (ϕ).....	75
Figure 4.5 Simulation snapshots of the composite system for various 4N-2456 concentration a) pure PVA, b) 0.5 wt%, c) 1 wt%, d) 2 wt%, e) 5 wt%, f) 10 wt%, g) 15 wt%, h) 20 wt%. The bubbles represent the free volume.	76
Figure 4.6 Radial distribution functions of the PVA backbone carbons at various 4N-2456 concentrations for (a) intramolecular $g_{C-C}^{intra}(r)$ and (b) intermolecular $g_{C-C}^{inter}(r)$	78
Figure 4.7 $g_{N-N}^{inter}(r)\phi_\omega$ as a function of the radial distance. $g_{N-N}^{inter}(r)$ is radial distribution function for the N atoms from 4N-2456 molecules. $\phi_\omega = \phi / \phi_m$ is the ratio of the 4N-2456 concentrations, and $\phi_m = 20wt\%$ is the maximum 4N-2456 concentration in the present simulations.	79
Figure 4.8 Mobility of the PVA chains at different 4N-2456 concentrations: (a) mean square displacement (MSD) and (b) diffusion coefficient (D).	81
Figure 4.9 The density as a function of temperature for calculation of glass transition temperature T_g of the pure PVA.....	84
Figure 4.10 The glass transition temperature T_g of the composites as a function of the 4N-2456 concentration.....	84
Figure 5.1 a) Illustration for the preparation process of PVA/PA composite films. b) UV-vis spectra of PVA and its PA composite films. c) Antibacterial properties of PVA and its PA composite films against <i>E. coli</i> and <i>S. aureus</i>	94
Figure 5.2 (a) snapshot of PVA/PA composites and (b) Non-bonded interaction energy between PVA and PA.....	96

Figure 5.3 H-bond number of each hydroxyl group on (a) PVA and (b) PA as a function of the PA concentration	97
Figure 5.4 normalized H-bond density of PVA/PA composites by comparing the peak area of O-H stretching (3100-3650 cm^{-1}) and that of C-H absorption.....	98
Figure 5.5 (a) Intra- and (b) inter-molecular RDF for the PVA backbones at different PA concentrations	101
Figure 5.6 (a) fraction volume fraction and (b) polymer volume fraction of PVA/PA composites as a function of the PA concentration (ϕ_w).	102
Figure 5.7 (a) MSD curves of PVA chains in the composites as a function of time and (b) dependence of D on the PA concentration	104
Figure 5. 8 (a) change of backbone torsion of PVA chains, and (b) snapshots for the torsion change of PVA backbones from $t=440$ to 490 ps	105
Figure 5.9 (a) Plots of temperature dependence of density, and (b) glass transition temperature (T_g) values of PVA/PA composites as a function of PA concentrations, obtained by MD, DSC and MDA techniques.....	106
Figure 5.10 Stress-strain curves of PVA and PVA/PA composites obtained from (a) MD simulations and (b) experiments. (c) Elastic modulus PVA/PA composites as a function of PA concentrations.	110
Figure 5.11 Snapshots under the tensile deformation of the 9.6PA sample at tensile strain of 1.0%, 27% and 33% during uniaxial tension.	111

LIST OF TABLES

Table 2.1 The three types of hydrogen bond interaction: strong, moderate and weak	15
Table 2.1 Detailed mechanical properties including tensile strength, modulus, stain at failure, obtained from tensile tests as well as elastic modulus predicted by MD simulation.	41
Table 2.2 Dynamic mechanical properties of PVA films with varied water content by controlling the relative humidity (RH) of the sample chamber and as-obtained characteristic relaxation times (τ_r).	51
Table 4.1 The model systems with different 4N-2456 concentrations.	69
Table 4.2 Glass transition temperatures of the composite systems for various 4N- 2456 concentrations.	85
Table 4.3 Mechanical properties of the composite systems at various 4N-2456 concentrations.	86
Table 5.1 Detailed mechanical properties including tensile strength, elastic modulus, stain at failure, obtained from tensile tests and MD simulations.	111

LIST OF ABBREVIATIONS

HB	Hydrogen Bonding
PVA	Poly(vinly alcohol)
D	Donator
A	Acceptor
MD	Molecular Dynamic
ND	Nano-Diamond
CN	Carbon Nanotube
MWCNTs	Multi-Walled Carbon Nanotubes
AIM	Atoms In Molecules
1N-4	4-Aminopyrimidine
2N-24	2,4-Diaminopyrimidine
3N-246	2,4,6-Triaminopyrimidine
4N-2456	2,4,5,6-Tetraaminopyrimidine
3N-MA	Melamine
DMA	Dynamic Mechanical Analyzer
QENS	Quasi-Elastic Neutron Scattering
DFT	Density Functional Theory
AFM	Atomic Force Microscopy
TGA	Thermogravimetric Analysis
DSC	Differential Scanning Calorimetry
PALS	Positron Annihilation Lifetime Spectroscopy
mg	Milligram
Tg	Glass Transition Temperature
PALS	Positron Annihilation Lifetime Spectroscopy
Ps	Positronium
o-Ps	Ortho-positronium

p-Ps	Para-positronium
ps	Picosecond
R	Mean Radius
ΔR	Delta Radius
FFV	Fraction Free Volume
IR	Infrared
ATR	Attenuated Total Reflectance
NPT	Constant Number, Pressure and Temperature Ensemble
RDF	Radial Distribution Function
MSD	Mean Square Displacement
vdW	van der Waals
PME	Particle Mesh Ewald

LIST OF SYMBOLS

N_{cr}	Optimal Number of HB Clusters
\mathbf{r}	Position
\mathbf{v}	Velocity
\mathbf{a}	Acceleration
\mathbf{b}	Derivative of the acceleration
δt	Delta time
t	Time
\mathbf{a}^c	Corrected Acceleration
\mathbf{r}^p	New position
$c_0, c_1, \text{ and } c_3$	Coefficients of Taylor Formula
wt%	Weight Percent
°C	Degree Celsius
μm	Micrometre
h	Hour
min	Minutes
τ_3	Lifetime
V_f	Free Volume
α_f	Free Volume Expansion Coefficient
K	Kelvins
Pa	Atmospheric Pressure Unit
ε	Strain Tensor
σ	Stress Tensor
\mathbf{C}	Stiffness Matrix
λ	Lamé Constant
E_Y	Young's Modulus
v_0	Occupied Volume

ϕ_w	Water Content
σ_y^a	Yield Strength
σ_m^a	Tensile Strength
E^a	Elastic Modulus
ϵ_b^a	Strain at Break
τ^a	Toughness
E_s^a	Elastic Modulus by MD
w	Mass Fractions
ϕ_N	2,4,5,6-Tetraaminopyrimidine Content
$^{\circ}\text{C}$	Centigrade
RH	Relative Humidity
τ_r	Relaxation Times
G'	Storage Modulus
Tan δ	Loss Factor
T	Measurement Temperature
D	Diffusion Coefficient
d	Diameter of Free Volume Cavities
γ	Poisson Ratio
G	Shear Modulus
R_p	Probe Radius

CHAPTER 1: INTRODUCTION

The content of this chapter gives an outline of the background and research motivation followed by giving research gaps, problem statement, research aim and objectives, scope of research and significance of the current research. This chapter presents the arrangement of the following chapters of the thesis.

1.1 Background and research motivation

In the last decades, lightweight polymeric materials have been gradually replacing traditional metal and ceramic materials in many fields, and thus it is highly attractive to design new polymeric materials with high and also tunable mechanical properties. With the increasing development in cosmonautics, automobile, and tissue engineering (Bonderer, Studart, & Gauckler, 2008; T. Guo, Heng, Wang, Wang, & Jiang, 2016; Wan et al., 2015), it has been desirable to develop polymer materials with high-strength, great-toughness and/or large ductility. For example, graphene oxides nanosheets have been used to successfully increase the strength and stiffness of polymer nanocomposites by mimicking the hierarchical structure of nature materials, such as nacre, but most of which are brittle, showing an extremely low breaking strain ($\leq 10\%$) (Q. Cheng, Jiang, & Tang, 2014; Q. Cheng, Wu, Li, Jiang, & Tang, 2013). This is largely because of the mutually exclusive mechanical mechanisms between strength and toughness as well as ductility (Barthelat, Yin, & Buehler, 2016; Ritchie, 2011). On the other hand, the strategy of modifying polymers by adding nanoscale or microscale modifiers usually make the final polymer material achieve high toughness and large ductility but relatively low tensile strength (H. Liu, Chen, Liu, Estep, & Zhang, 2010; Y. Sun & He, 2013; S. Wu, Guo, Kraska, Stuehn, & Mai, 2013). As a result, it remains a grand challenge to achieve a combination of high-strength,

great-toughness, and large- ductility in the polymer composite.

In nature, biological protein fibers, including byssus cuticle of marine mussels and spider silk, exhibit a unique combination of high strength and large ductility (S. Keten, Xu, Ihle, & Buehler, 2010). Researches reveal that the nanoscale separated structure, consisting of dense dopamine-Fe ion containing cross linking in the granules found in a continuous protein matrix, have a significant role in determining the mechanical properties of the byssus cuticle of marine mussels by providing a remarkable combination of stiffness and large breaking strain (about 100%) (Harrington, Masic, Holten-Andersen, Waite, & Fratzl, 2010; Holten-Andersen, Fantner, Hohlbauch, Waite, & Zok, 2007; Holten-Andersen et al., 2009; Priemel, Degtyar, Dean, & Harrington, 2017). When the cuticles are exposed to high strains, the granules provide cohesion between the long byssus cuticles, enabling the cuticles to extend significantly and prevent the crack propagation by forming of generous dispersed microcracks. For spider silk, it is the antiparallel β -sheet nanocrystals contained in the highly conserved poly-(Gly-Ala) and poly-Ala regions in the soft protein matrix, giving rise to nanoconfinement, that controls high strength and great toughness (S. Keten et al., 2010). Therefore, this is intriguing that advanced polymeric materials show enhanced toughness, greater tensile strength and larger ductility by creating a similar β -sheet nanocrystals or granular structure within polymer chains.

Recently, increasing global awareness of microplastics has significantly driven the creation of high-performance biodegradable polymeric materials to replace traditional non-biodegradable counterparts. As one water-soluble biodegradable polymer, poly (vinyl alcohol) (PVA) has growingly found extensive applications in packaging, optical film, and agricultural technology fields (F. Müller-Plathe, 1998; Pan, Peng, & Jiang, 2007). The ideal formula of the or PVOH is $[\text{CH}_2\text{CH}(\text{OH})]_n$ and it has been always desirable to develop mechanically strong, tough and ductile PVA materials to expand its practical applications in industries.

There is a wide industry uses of the PVA in 3D Printing to support the 3D structure, in the water transfer printing process and as an embolization agent in medical procedures. Despite great advances in reinforcement and toughening of PVA, some challenging research gaps, in particular the correlation between structural composition and mechanical performances, remains to be filled so far.

1.2 Research gaps

Despite some advances made in the creation of strong and tough PVA materials, to the best knowledge of the author, there still exist some significant research questions to be answered:

- (i) Although it is widely recognized that PVA is highly moisture/water sensitive, it remains unclear how water content impact intermolecular hydrogen-bond (HB) interactions, physical structure, and mechanical properties of PVA, i.e., the structure-property relationship;
- (ii) Small multiamine molecules have been reported to be highly effective in enhancing overall mechanical properties (strength, modulus, toughness and ductility) of PVA through HB cross-linking, but there has been a lack of insightful understanding in the mechanical mechanisms behind by combining experimental and molecular dynamic (MD) simulations; and
- (iii) It has been unclear whether other small molecules capable of forming HB can improve mechanical properties of PVA, and how they impact.

1.3 Problem statement

Previous studies on improving mechanical performances of PVA heavily rely on macrostructure design, the investigation of the molecular mechanism is limited. In addition, there is a lack of a systematic understanding of the structure-performance correlation in PVA materials by combining MD simulation and

experimental studies.

1.4 Research aim

Therefore, the main aim of this thesis is to understand how the added small molecules (i.e., water, multiamine, and phytic acid) affect the intermolecular HB, polymeric chain dynamics, and the final mechanical properties of PVA materials.

1.5 Research objectives

The main objective of this project is to investigate the relationship between the structural composition and mechanical properties of PVA materials. The detailed objectives of this research are:

- To investigate the HB network, polymer dynamics, and mechanical properties of pure PVA and its blends containing a varied amount of water, 2,4,5,6-Tetraaminopyrimidine, and phytic acid by using MD simulation and/or experiment;
- To examine the formation and damage of local HB structure as well as chain conformation transitions;
- To validate the simulated results with the experimental data of PVA materials and to provide some guidelines for creating mechanically robust PVA materials.

Hence, this study is designed to assess mechanical performances of PVA by introducing different small molecules to alter the physical structure. These results can contribute to understanding the relationship between microscopic molecular details (such as HB networks and the intermolecular interactions) and macroscopic mechanical performances.

1.6 Significance of research

- Understand impacts of small molecules on intermolecular HB

interactions, glass transition, free volume, chain movements of polymer (here, PVA);

- Unveil the correlation between intermolecular HB interactions, polymer chain dynamics, and mechanical properties of PVA;
- Gain an in-depth insight into the governing effect of HB interactions on the overall performances of polymers at a molecular level; and
- Contribute to the design of mechanically robust polymeric materials via manipulating intermolecular interactions.

1.7 Research scope

This thesis focuses on understanding how small molecules impact physical structure and mechanical properties of polymeric materials by applying a combined experimental and MD simulation method. The MD data are used to deepen the understanding of experiment results which in turn can be used to validate simulated results. The scope of the study will be focused on the PVA materials containing different small molecules with an ability to form extensive intermolecular HB with PVA. The impacts of small molecules on intermolecular HB interactions, glass transition, free volume, chain mobility and mechanical property of PVA are systematically studied to understand the relationship between physical composition and mechanical properties of PVA.

1.8 Thesis outline

The thesis outline is provided separately for each chapter as follows:

Chapter 2: Literature review

This chapter provides a general review on existing literatures on strategies for improving mechanical performances (i.e., strength, extensibility, and toughness) of PVA materials as well as challenges with these strategies. Among them, the spider-silk-inspired hydrogen-bond cross-linking approach can achieve

simultaneous enhancements in mechanical strength, modulus, ductility, and toughness of PVA by adding small molecules as cross-linkers. However, there has been a lack of an in-depth understanding on the correlation between physical composition and mechanical performance of PVA materials, which remains to be addressed.

Chapter 3: Water governs the mechanical properties of poly(vinyl alcohol)

This chapter aims to address how water molecules control the macroscopic mechanical properties and microscopic chain dynamics of PVA. The study will provide a fundamental insight into the molecular mechanism behind by which water content governs the mechanical performance of PVA experimentally and theoretically. This work has comprehensively evaluated the effect of water content on mechanical properties, intermolecular HB interactions, and chain dynamics of PVA.

Chapter 4: Insights into the Hydrogen-Bond Cross-linking Effects of Small Multiamine Molecules on Poly(vinyl alcohol) by Molecular Dynamics Simulations

Our previous study has demonstrated that small organic multiamine is able to significantly improve overall mechanical performances of PVA through the H-bond cross-linking effect, but the mechanical mechanism remains unclear. This chapter aims to build the relationship between multiamine and PVA. The work offers an understanding of how the tetraaminopyrimidine (4N-2456) molecule influences the PVA chain dynamics and mechanical properties of the PVA matrix on a molecular level.

Chapter 5: Structure, Chain Dynamics and Mechanical Properties of Transparent Poly(vinyl alcohol)/Phytic Acid Composite Films with Improved Antibacterial Properties

As a bioderived polyhydroxy molecule, phytic acid (PA) is expected to form extensive H-bond interactions with PVA and to ultimately impact physical

structure and mechanical properties of PVA. This chapter aims to investigate the impact of PVA on the optical, antibacterial, H-bond interactions, structure, glass transition temperature and mechanical properties of PVA. This work will provide an insight into the relationship between the intermolecular interactions and chain dynamics and macroscopic properties of PVA/PA composites.

Chapter 6: Finally, a summary of our findings is given.

CHAPTER 2: LITERATURE REVIEW

2.1 Introduction

As a water-soluble biodegradable polymer, inexpensive PVA has been extensively applied in biomedical engineering (Chiessi, Cavalieri, & Paradossi, 2007), membrane separation packaging and agricultural technology fields (Florian Müller-Plathe, 1998; Pan et al., 2007). Because of the existence of hydroxyl groups in the chemical structure of PVA (Figure 2.1), the hydrogen-bond (HB) plays a key role in controlling the overall properties of PVA, such as the thermal stability, degradability, water-solubility, and mechanical properties.

Regarding HB, it is generally formed through electrostatic interactions among one hydrogen atom and two other heavy atoms. In the traditional D—H···A system, where D is a proton donator and A is an acceptor. HB is built between the hydrogen atom and the more negatively charged atom. It is noteworthy that the strength of the HB is stronger than the van der Waals interaction but weaker than the covalent bond. Recently, some research have been conducted to investigate how the unique weak HB network governs the structure and mechanical properties of the materials (Hongbin Li, Zhang, Weiqing Xu, & Zhang, 2000; Medhekar, Ramasubramaniam, Ruoff, & Shenoy, 2010). Hence, it is essential to understand how hydrogen bonds affect overall properties of PVA.

In recent years, physical and chemical features of PVA-based materials have been reported experimentally (Otsuka & Suzuki, 2010; Song, Xu, & Guo, 2013; Song, Xu, Lu, & Guo, 2015a, 2015b) and theoretically (Chiessi, Francesca Cavalieri, & Paradossi, 2007; Florian Müller-Plathe, 1998; Tesei, Paradossi, & Chiessi, 2012). Typically, the mechanical performances of PVA materials can be tailored by blending with many kinds of polymers, nanoparticles and small organic molecules. However, the molecular mechanisms of these PVA-based materials are

rather complicated and remain unclear. Moreover, there is a lack of the understanding of the influence of the HB network on the dynamics of PVA chains and its physical properties, such as water solubility, strength, and stiffness. The experimental research is difficult to explain and to predict the results at a molecular level. Therefore, it is necessary to combine experiment studies and MD simulations to gain a better understanding of the physical structures and mechanical performance of PVA composites.

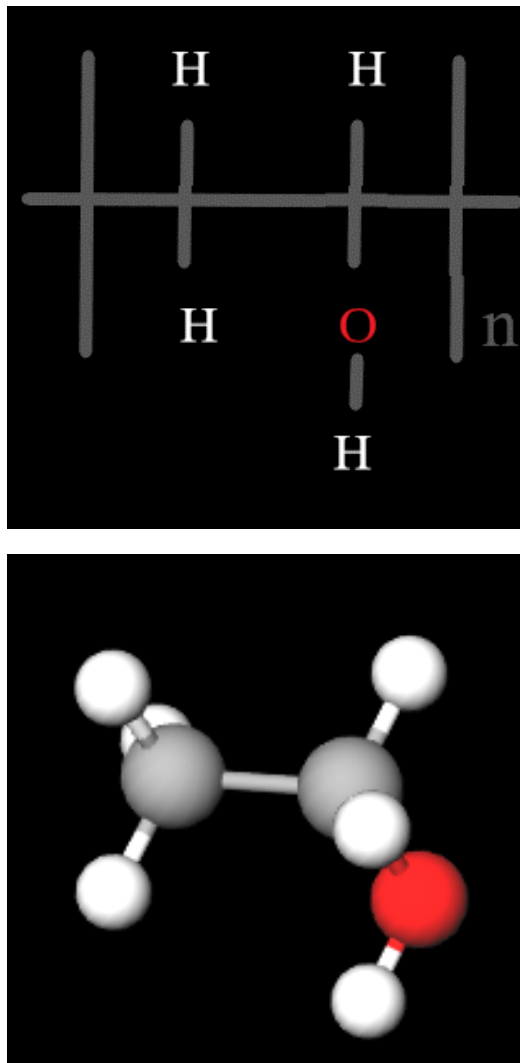


Figure 2.1 Molecular structure of PVA

2.2 Methods of creating PVA based nanocomposite

Last several years have witnessed the rapid use of PVA as packaging materials for electric & electronics and chemical materials, and optical films for electronic devices. For the applications of PVA in these sectors, it is necessary to improve its thermal and mechanical properties without compromising its biodegradability. Generally, the microscopic structure of polymer materials has fundamental effects on the thermal and mechanical properties. For PVA, abundant functional hydroxyl groups have been reported to strongly determine the macroscopic performance of PVA. For example, introducing PVA chains into graphene oxide paper resulting in increased stiffness of the composite because the enhanced cooperativity HB network (Compton et al., 2012).

2.2.1 Nanofiller

The formation of polymer nanocomposites has led to enhanced mechanical properties. For instance, graphene has been extensively used to reinforce polymers to achieve improved mechanical properties, thermal stability, gas barrier and the conductivity (Ackbarow & Buehler, 2008; Potts, Dreyer, Bielawski, & Ruoff, 2011). However, the absence of covalent bonding or non-covalent binding interactions (typically HB) in graphene/polymer composites often leads to poor dispersion (Potts et al., 2011). Moreover, these polymer nanostructured materials often show reduced ductility and toughness relative to the polymer bulk (Ackbarow & Buehler, 2008; Ritchie, 2011).

Recently, Morimune et al. has successfully achieved remarkably improved mechanical properties of PVA nanocomposite by adding nano-diamond (ND) particles (Morimune, Kotera, Nishino, Goto, & Hata, 2011) (Figure 2.2). Meanwhile, effects of carbon nanotube (CNTs) and modified CNTs on the mechanical, thermal stability, swelling ability and electric conductivity properties

of PVA nanocomposite films have been studied. Despite a certain improvement in electric conductivity, other properties are not significantly changed (Konidari, Soulas, Papadokostaki, & Sanopoulou, 2012). Upon the addition of multi-walled carbon nanotubes (MWCNTs), the structural variation is discovered in PVA matrix accompanied with the function change (Hamdy M. Zidan, Abdelrazek, Abdelghany, & Tarabiah, 2018). In addition, the crystalline of the nanocomposite PVA was reported to change with increasing contents of CrF₃ and MnCl₂ nanoparticles, and shows that the degree of crystallinity strongly relied on the interactions between the nanoparticles and PVA (H. M. Zidan, 2003).

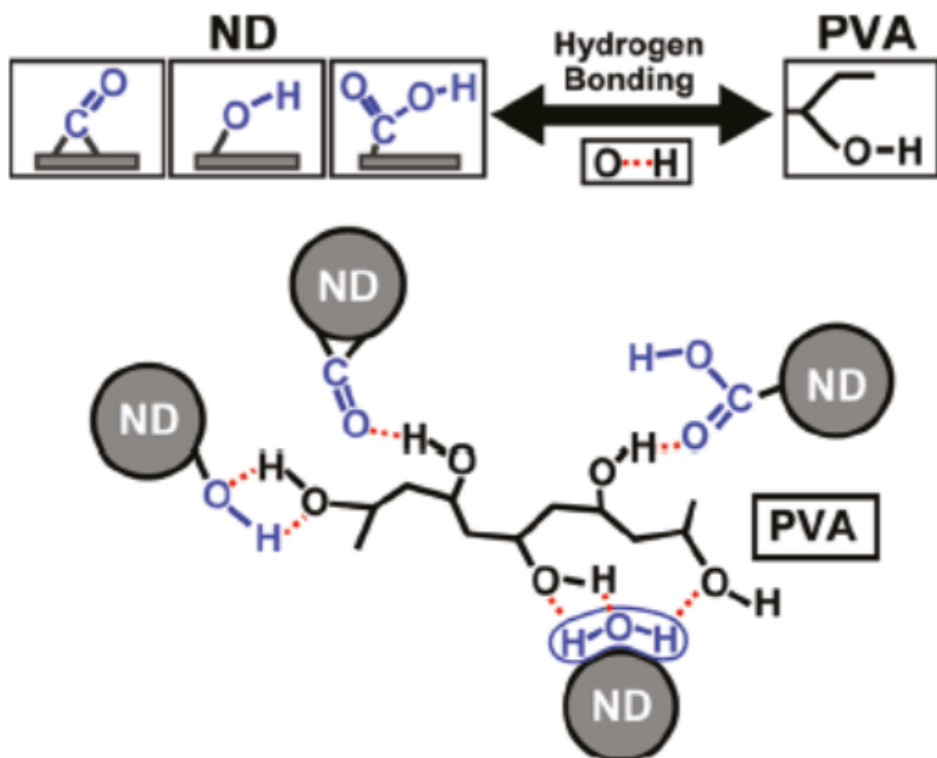


Figure 2.2 View of the interaction between PVA and ND

(Morimune et al., 2011)

2.2.2 Electron beam or γ -radiation

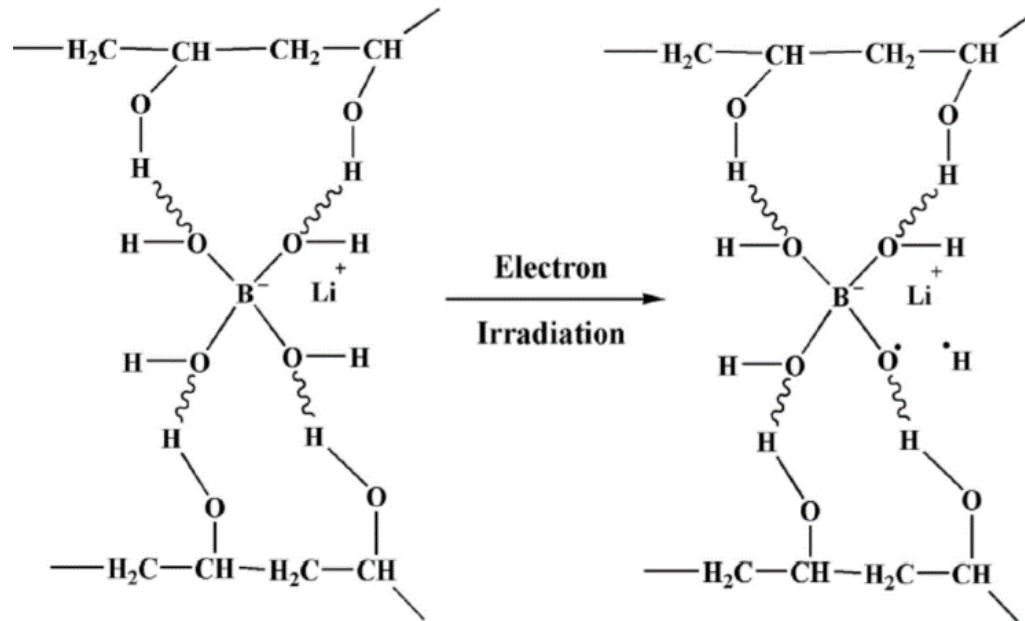


Figure 2.3 Schematic illustration of the chain scission induced by electron beam

(Ismayil, Ravindrachary, Sanjeev, & Praveena, 2018)

Another approach for improving the mechanical properties and thermal stability is radiation via electron beam or γ -radiation, which is a pollution-free method to alter the structure of polymers (Figure 2.3). In recent years, this method has been employed to enhance properties of PVA nanocomposites. Rad et al. (Shokuhi Rad & Ebrahimi, 2017) studied the effect of electron beam irradiation on the mechanical and thermal properties of PVA-clay nanocomposites. They found that the irradiation enhanced the elastic modulus and tensile strength at a dose of 100 kGy but the mechanical properties decreased at a higher dose of irradiation. Cross-linking or chain interruption of polymers usually occurs during irradiation (Rao, Rao, & Shridhar, 2002). These reactions can affect the overall performances, such as dielectric, thermal, mechanical and optical properties, of polymer nanocomposite. Ismayil et al. (Ismayil et al., 2018) found that the structure modification of PVA/Li₂B₄O₇ was induced by irradiation and the ion transport rate increased with increasing free volume sizes. Meanwhile, homogeneous PVA-montmorillonite nanocomposites can be also obtained by appropriate irradiation

(Abd Alla, Nizam El-Din, & El-Naggar, 2006).

2.2.3 Freezing/thawing alternation

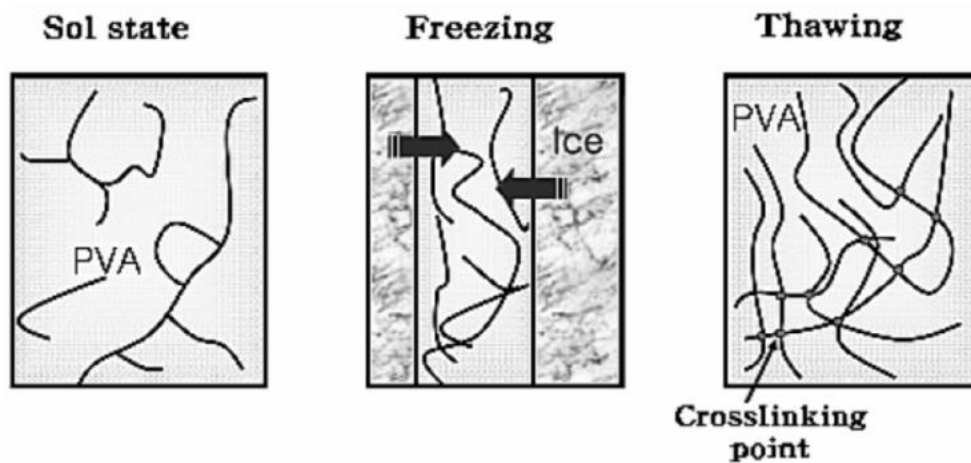


Figure 2.4 Schematic illustration of crosslinking PVA formed by freezing and thawing way
(*Poly (vinyl alcohol)(pva)-based polymer membranes, 2009*)

The freezing/thawing cycle method has recently emerged as an effective strategy for improving mechanical properties of PVA (see Figure 2.4). The resultant PVA materials prepared by this method usually exhibit better mechanical properties and thermal stability than the PVA counterparts cross-linked by chemical or radiation methods because the final networks are crosslinked in three dimensions (Hassan & Peppas, 2000). Additionally, the effect of freezing/thawing cycles on the diffusion properties of PVA film is examined and these properties can be tuned by varying the number of the cycles. In addition, the final properties of the PVA materials by this method are strongly determined by the polymer molecular weight, solution concentrations, the time and number of freezing and thawing cycles (Hassan & Peppas, 2000; Simões & De Oliveira, 2010).

2.2.4 Hydrogen-bond cross-linking

In nature, some protein materials possess sophisticated hierarchical structures which enable highly specific functions and outstanding mechanical properties

(high strength and great toughness). The mechanical strength of protein materials consisting of the basic secondary structures is found to largely depend on the strength of HB clusters. For instance, the secondary structure is composed of assemblies of HBs (Sinan Keten, Xu, Ihle, & Buehler, 1998). Although the HBs are much weaker compared to covalence bonds, the formation of HBs cluster in the secondary structures enhances the strength and robustness of protein materials.

As a typical example, spider silk exhibits extraordinary mechanical features, namely a unique combination of high-strength, large-extensibility, and great-toughness, thus regarded as the strongest polymer materials in nature. Recent research has revealed that the extraordinary mechanical properties of spider silk are the result of high density of hydrogen-bonded β -sheet nanocrystal confined in the primary silk protein molecules (Porter, Vollrath, & Shao, 2005). The study reveals that the strength of a single HB is weak, but significantly increase when multiple HBs cooperate. As a result, HB-bonded sheet exhibits a strong, tough, and resilient mechanical behavior (S. Keten et al., 2010).

In essence, the nanoconfinement of silk protein molecules owing to the high cohesive energy density of HBs determines the high modulus and high strength of silk (see Figure 2.5). The optimal number N_{cr} of of HB clusters is approximate four based on the energetic analysis in reference (Sinan Keten & Buehler, 2009). Therefore, the mechanical property of HB network is not only related to the strength of a single HB, but also the cooperating manner of HBs.

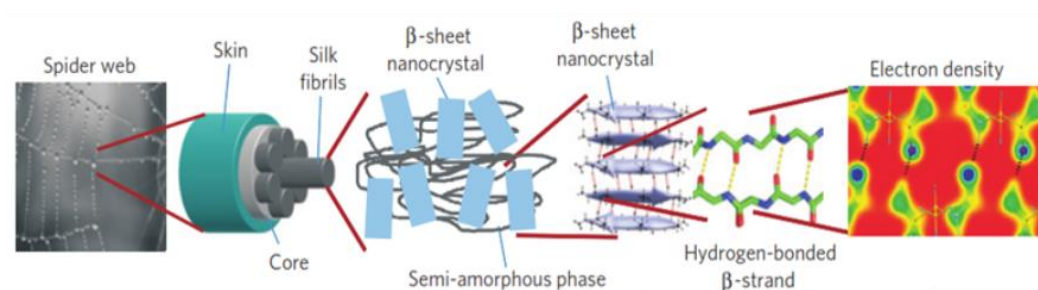


Figure 2.5 Structure evolution of the hierarchical spider silk from macroscopic to nanoscopic

(Compton et al., 2012)

Advances in both experimental and theoretical calculations make it possible to investigate the nature of HB. Theory of Atoms in Molecules (AIM) proposed by Bader is the one of acceptable ways to understand the HB (Bader, 1994).

In a recent research, the ‘hydrogen bridge’ has been proposed to define the interaction of HB in a variety of systems, and related strength is dependent on the distance, angle, and direction of atoms (table 2.1) (Gautam R. Desiraju, 2002; Grabowski, 2006). These interactions in aqueous solution are one of the typical examples, and several theoretical methods have been developed to calculate the structure and energetics of HB in water (G. R. Desiraju & Steiner, 1999; Honegger & Leutwyler, 1988; Jeffrey, 1997; Smith, Swanton, Pople, Iii, & Radom, 1990).

Table 2.1 The three types of hydrogen bond interaction: strong, moderate and weak (Grabowski, 2006)

H-bond parameters	Strong	Moderate	Weak
Interaction type	Strongly covalent	Mostly electrostatic	Electrostatic/dispersed
Bond lengths (H···Y[Å])	1.2–1.5	1.5–2.2	>2.2
Lengthening of X–H (Å)	0.08–0.25	0.02–0.08	<0.02
X–H Vs. H···Y	X–H ≈ H···Y	X–H < H···Y	X–H << H···Y
H-bond length (X·Y [Å])	2.2–2.5	2.5–3.2	>3.2
Directionality	Strong	Moderate	Weak
H-bond angles (°)	170–180	>130	>90
H-bond strength (kcal/mol)	15–40	4–15	<4
Relative Infrared shift (cm ⁻¹)	25%	10–25%	<10%

Despite great advances in the understanding of HB, there remains a lack of systematical investigation of the structure and the formation of the hydrogen bond in various materials at both the experimental and theoretical levels. Recently, some work on HB cover a range of from biological systems to synthetic materials by various methods (Grabowski, 2006). The mechanical properties of graphene oxide paper in water and grafted with PVA nanocomposites were examined using experimental and computational methods (Compton et al., 2012). The water molecules inside the graphene oxide paper were found to contribute to the stress modulus through hydrogen-bond interactions, and the addition of PVA into nanocomposites enhanced the modulus owing to the enhancement of the

hydrogen-bond network (Figure 2.6 and Figure 2.7). However, the mechanical properties of hydrogen bond in PVA composites remain unclear.

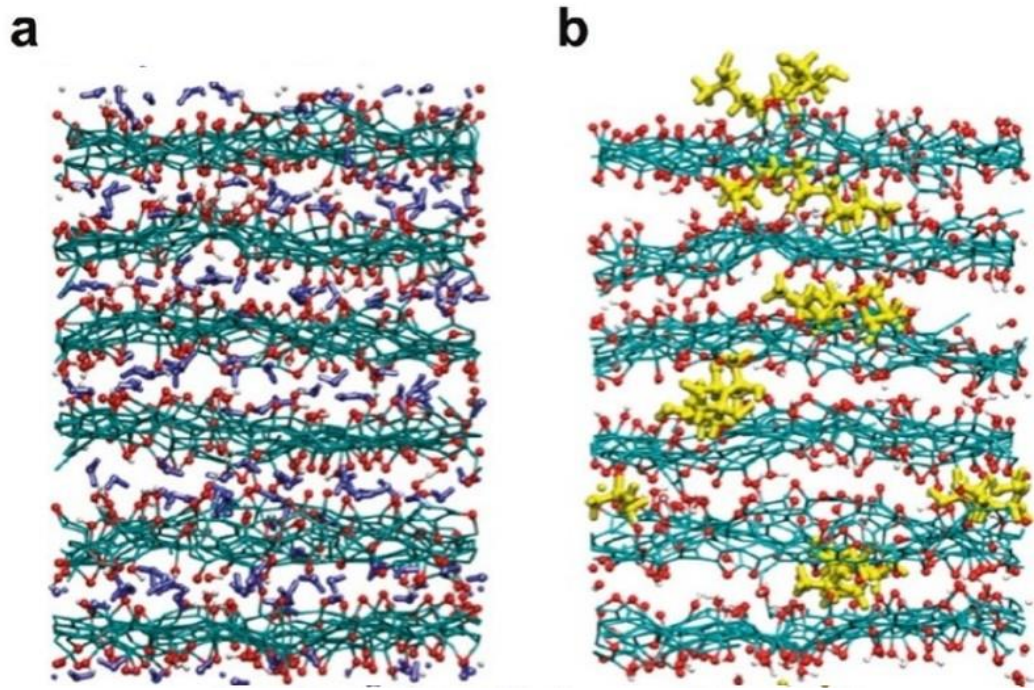


Figure 2.6 (a) Graphene oxide paper added with H₂O and (b) graphene oxide paper grafted with PVA

(Compton et al., 2012)

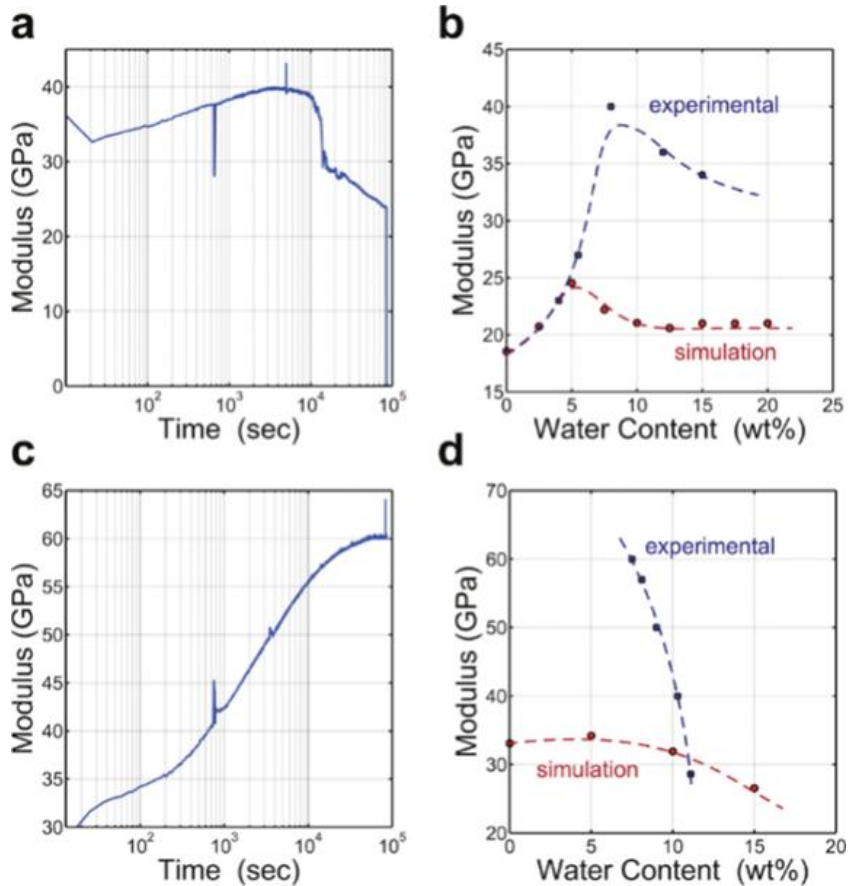


Figure 2.7 The variation of storage modulus with time and water content in experiment and simulation

(Compton et al., 2012)

Inspired by the molecular mechanical mechanism of spider silk, Song PA et al. (Song et al., 2013) exploited melamine molecules as a hydrogen-bond crosslinker to improve strength, extensibility and toughness of PVA as a loading level less than 1.0 wt% in 2013 (see Figure 2.7). In a following work in 2015 (Song et al., 2015a), they further investigated the HB network by adding small multi-amines (1N-4, 2N-24, 3N-246 and 4N-2456) into PVA, which shows enhanced stiffness and toughness because of hydrogen-bond crosslink effects of small molecules. However, the corresponding mechanical mechanism remain not well-understood so far. In addition, they achieved dramatically improved thermal stability of PVA by mixing a small amount of the multi-amine molecules (Song et al., 2015b), (see Figure 2.8). Their results indicated a relationship between

hydrogen bond networks and thermal stability of PVA.

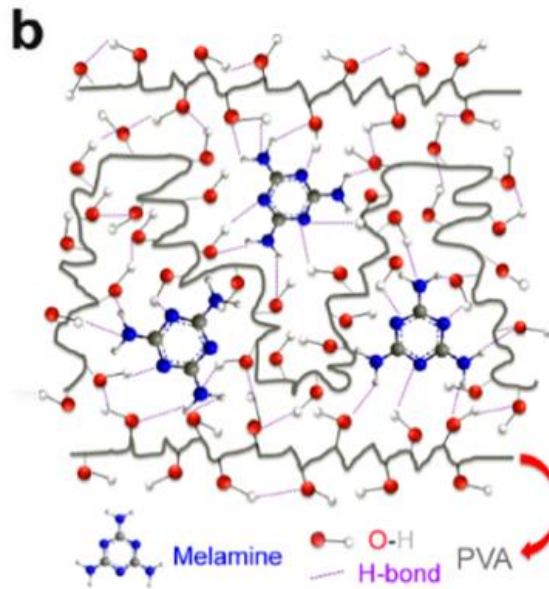
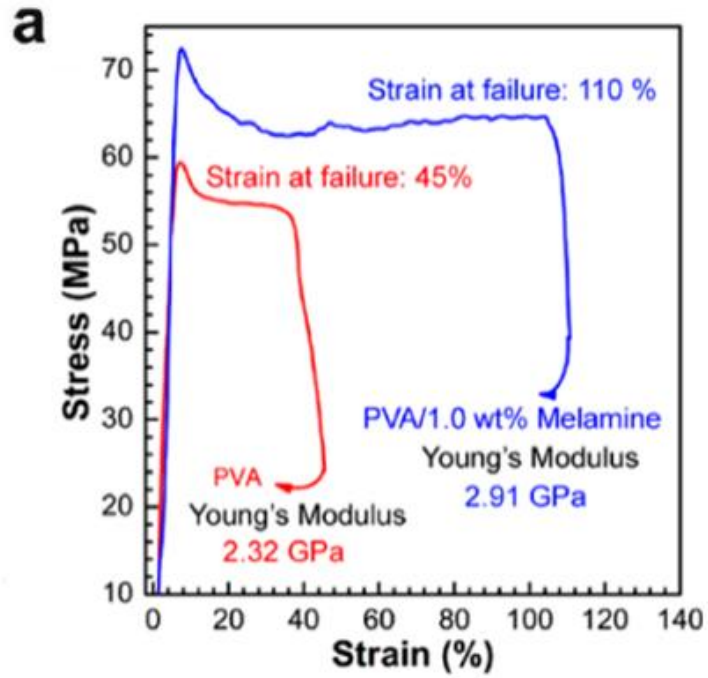


Figure 2.8 (a) The improved Young's modulus, strain and stress of the PVA hybrid melamine composite (b) schematic representation of interactions between Melamine and PVA.

(Song et al., 2013)

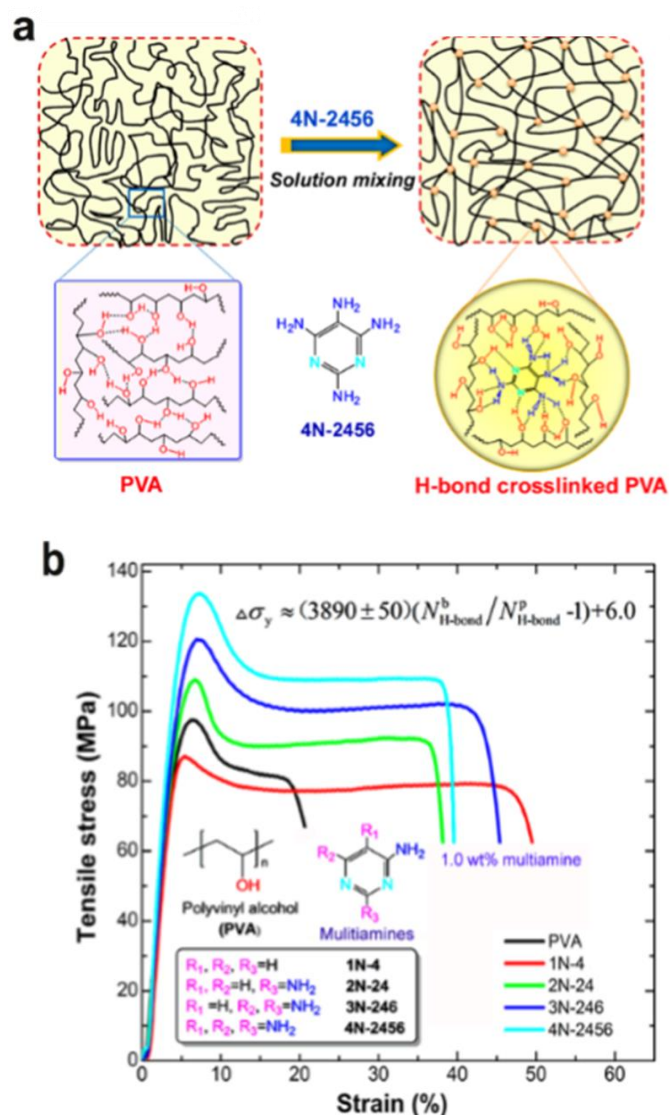


Figure 2.9 (a) Snapshot of the creation of the hydrogen bond network by mixing small multiamines and (b) the curve of tensile stress-strain (Song et al., 2015a)

These previous results clearly show that mechanical and thermal stability of PVA materials are strongly dependent on the HB network. Although some progresses have been made in understanding the molecular mechanisms behind, the role of HB network on mechanical properties of PVA nanocomposite remains yet to be explored on a molecular level. Previous work has shown that these molecular mechanisms can be unveiled through a combination of experiment and MD simulations method (Florian Müller-Plathe, 1998; Sacristan & Mijangos, 2008;

Tesei et al., 2012; Wolf & Suter, 1984).

2.4 Molecular dynamics simulation of PVA

In addition to extensive experimental studies, enormous efforts have been made on the HB network of PVA systems by using MD simulations (Florian Müller-Plathe, 1998; Sacristan & Mijangos, 2008; Tesei et al., 2012; Wolf & Suter, 1984). Afterwards, the system of a single PVA chain (21 to 161 repeating units) with the hundreds of water molecules at different temperatures are simulated to investigate the conformational features. At the same time, Müller-Plathe investigated the diffusion of water in PVA materials with different water content (66-97%) (Florian Müller-Plathe, 1998; Tesei et al., 2012).

Recently, the MD simulation on a PVA oligomer (3% w/w) in very diluted aqueous solution has been conducted to study the structural and dynamic features, and to test the robustness of MD force field (Tesei et al., 2012). Another work analyzed the effect of cross-linking density on the glass transition of PVA with adding 1,2-ethanediol (25% and 90%) (Bermejo & Ugarte, 2010), and the results showed that an increase in cross-linking degree resulted in the increase of glass transition temperatures.

Wu et al. simulated glass transition of the PVA/water (21%) system and found that the HB number decreased with rising temperatures (C. Wu, 2010). The MD simulations on HB and strain features on graphene oxide paper have also recently been reported (Compton et al., 2012; Solercrespo et al., 2018). Very recently, the MD simulation reveals the effects of plasticizer content (10%-40%) on the elastic modulus of PVA (Ni, Wang, & Zhao, 2018).

In classical molecular dynamics simulations, the popular integral algorithms include Verlet, Velocity-Verlet, Leap-Frog, and Predictor-Corrector to get the positions and velocities of the particles contained in the model system.

The Verlet integration algorithm was proposed by Loup Verlet in 1967 (Verlet,

1967). This method obtains the position $\mathbf{r}(t+\delta t)$ at the time $t+\delta t$ through the position $\mathbf{r}(t)$ and the acceleration $\mathbf{a}(t)$ at time t as well as the position $\mathbf{r}(t-\delta t)$ at time $t-\delta t$:

$$\mathbf{r}(t+\delta t) = 2\mathbf{r}(t) - \mathbf{r}(t-\delta t) + \delta t^2 \mathbf{a}(t) \quad (2.1)$$

The velocity is updated using the values at the times $t-\delta t$ and $t+\delta t$:

$$\mathbf{v}(t) = \frac{1}{2\delta t} (\mathbf{r}(t+\delta t) - \mathbf{r}(t-\delta t)) \quad (2.2)$$

In the Verlet algorithm, the positions are advanced in one single step via equation (2.1). The errors for the positions and velocities are of order four and two, respectively. It is simple to implement and to show energy conservation well. However, the velocity disappears in the process of updating the position and is only as the result of the calculation. In addition, it can be seen from the equation (2.1) that there are zero-order and second-order terms of δt , but there is no first-order term. The discontinuity of this order may lead to the reduction of numerical precision.

Some modified algorithms have later emerged for these shortcomings of the Verlet algorithm. For example, the Leap-Forg integration is one of the modified Verlet algorithms (Marcussvanberg, 1997). In the Leap-Forg method, the particle position can be calculated:

$$\mathbf{r}(t+\delta t) = \mathbf{r}(t) + \delta t \mathbf{v}\left(t + \frac{1}{2}\delta t\right) \quad (2.3)$$

The particle velocity at half time step is given by

$$\mathbf{v}\left(t + \frac{1}{2}\delta t\right) = \mathbf{v}\left(t - \frac{1}{2}\delta t\right) + \delta t \mathbf{a}(t) \quad (2.4)$$

As can be seen from the difference format above, the calculation of coordinates and velocity in the Leapfrog algorithm cannot be kept in synchronization. In order to get the velocity at the current moment, the average of the velocities needs to be calculated at two moments:

$$\mathbf{v}(t) = \frac{1}{2} \left(\mathbf{v} \left(t + \frac{1}{2} \delta t \right) + \mathbf{v} \left(t - \frac{1}{2} \delta t \right) \right) \quad (2.5)$$

The Velocity-Verlet algorithm overcomes the unsynchronization of coordinate and velocity calculations in the Leap-Frog method, which is the most used algorithm in molecular dynamics simulation (Spreiter & Walter, 1998). In this method, we update the positions and velocities using both the current and new values of the acceleration:

$$\mathbf{r}(t + \delta t) = \mathbf{r}(t) + \delta t \mathbf{v}(t) + \frac{1}{2} \delta t^2 \mathbf{a}(t) \quad (2.6)$$

$$\mathbf{a}(t + \delta t) = \mathbf{F}(t + \delta t) / m \quad (2.7)$$

$$\mathbf{v}(t + \delta t) = \mathbf{v}(t) + \frac{1}{2} \delta t [\mathbf{a}(t) + \mathbf{a}(t + \delta t)] \quad (2.8)$$

Another advantage of this algorithm is that it only needs to store the position and velocity information at the current time step during the simulation process, thereby reducing the space occupied during the running of the program. Moreover, the Velocity-Verlet algorithm is numerically stable, and conserves energy well at relatively large time steps.

The Predictor-Corrector algorithm is derived based on the Taylor expansion (Butcher, 2010). Here we use the third-order prediction-correction algorithm as an example to briefly introduce the calculation steps of the algorithm. First, given the position \mathbf{r} , the velocity \mathbf{v} , the acceleration \mathbf{a} , and the derivative of the acceleration \mathbf{b} with respect to time at time t , these quantities at time $t + \delta t$ can be predicted by the following formula:

$$\mathbf{r}^p(t + \delta t) = \mathbf{r}(t) + \delta t \mathbf{v}(t) + \frac{1}{2} \delta t^2 \mathbf{a}(t) + \frac{1}{6} \delta t^3 \mathbf{b}(t) \quad (2.9)$$

$$\mathbf{v}^p(t + \delta t) = \mathbf{v}(t) + \delta t \mathbf{a}(t) + \frac{1}{2} \delta t^2 \mathbf{b}(t) \quad (2.10)$$

$$\mathbf{a}^p(t + \delta t) = \mathbf{a}(t) + \delta t \mathbf{b}(t) \quad (2.11)$$

$$\mathbf{b}^p(t + \delta t) = \mathbf{b}(t) \quad (2.12)$$

The superscript p represents the predicted value of these quantities. According to the new position \mathbf{r}^p , the corrected acceleration \mathbf{a}^c can be obtained by the equation of motion, and the difference $\Delta\mathbf{a}(t + \delta t)$ between the corrected and predicted accelerations can be calculated. According to the difference of the accelerations, the corrected values of these quantities can be obtained:

$$\mathbf{r}^c(t + \delta t) = \mathbf{r}^p(t + \delta t) + c_0\Delta\mathbf{a}(t + \delta t) \quad (2.13)$$

$$\mathbf{v}^c(t + \delta t) = \mathbf{v}^p(t + \delta t) + c_1\Delta\mathbf{a}(t + \delta t) \quad (2.14)$$

$$\mathbf{a}^c(t + \delta t) = \mathbf{a}^p(t + \delta t) + c_2\Delta\mathbf{a}(t + \delta t) \quad (2.15)$$

$$\mathbf{b}^c(t + \delta t) = \mathbf{b}^p(t + \delta t) + c_3\Delta\mathbf{a}(t + \delta t) \quad (2.16)$$

where the coefficients c_0 , c_1 , c_2 , and c_3 are dependent on the differential equation and the expansion order of the Taylor formula. The third-order or higher-order Predictor-Corrector algorithm is more complex in construction than the Verlet algorithm and consumes more computer memory. If we only complete one iteration, the higher-order algorithm may not improve the computational accuracy over the low-order Verlet-type algorithm. Moreover, multiple iterations can lead to a large increase in the amount of computation.

2.5 Calculation of mechanical properties

To investigate mechanical properties of PVA materials, both theoretical and computational modelling have become increasingly important in the development of advanced materials for industrial and scientific applications, besides experimental methods. Experimentally, tensile tests can be performed by electromechanical testing machine (Ni et al., 2018); the hardness and elastic modulus of polymer films are obtained by nanoindentation test system or dynamic mechanical analyzer (DMA) (Compton et al., 2012; Song et al., 2015a); The dynamical features can be assessed with incoherent quasi-elastic neutron

scattering (QENS) (Chiessi, Francesca Cavalieri, et al., 2007; Paradossi, Finelli, Natali, Telling, & Chiessi, 2011). Previously, density functional theory (DFT) has been used to calculate the elastic and shear modulus (S. Keten et al., 2010), and the elastic constants from MD simulation, experimental results and DFT calculations were compared. In classical MD simulation, mechanical properties of samples are usually determined using the static, dynamic or fluctuation methods (Bermejo & Ugarte, 2010; Gusev, Zehnder, & Suter, 1996; Ni et al., 2018; Theodorou & Suter, 1986).

2.6 Identified research limitations

Previous work has shown that great advances have been made in experimental and simulation studies on PVA materials. Experimentally, the high degree of HB cross-linking can improve the strength and toughness of PVA polymer. The effect of HB network on the mechanical features has been well-predicted, but the related physical mechanisms are still not well-explained. Regarding simulation, the structural and dynamical features of PVA in aqueous solution have been well-investigated. The number of HB of PVA systems can be tuned by adjusting the concentrations of added molecules. Despite great advances in existing experimental and simulation studies, there are still significant research gaps to be filled.

For experimental studies, the HB effects lack quantitative accuracy. For simulation investigations, to date little work has been carried out to investigate the effects of density of hydroxyl group on the formation of HB network by using MD simulation. Moreover, most of MD simulations only focus on diluted solutions of PVA, and the PVA chains for simulations possess relatively low degrees of polymerization. Most importantly, the relationship between the structure of HB and mechanical properties of PVA has remained unclear so far. Therefore, it is critical to gain a more in-depth systematic understanding on effects of physical

compositions on their mechanical performances by a combined experimental and MD simulation method.

As such, the purpose of this thesis is to clarify how the HB impact physical structural composition and mechanical properties of PVA materials as well as their relationships. To achieve this goal, three molecules, (i.e., water, 2,4,5,6-tetraaminopyrimidine (4N-2456) and phytic acid) with different number of hydroxyl groups have been selected. We choose these three molecules mainly due to two reasons: 1) although they possess very different elements, they can form HBs with PVA. We want to explore the role of HB in different PVA-based composites. 2) We have designed the related experiments about these molecules. Therefore, the MD simulations for the composites of PVA with these three molecules can be carried out to make comparison with the experiments. Firstly, we explore the relationship between HB network and mechanical properties for PVA materials with different water content. This part will uncover the governing effect of water content on mechanical properties of PVA. Secondly, effects of the 4N-2456 contents on the HB network and mechanical properties of PVA are investigated theoretically and compared with available experimental results. Finally, a combined experimental and MD simulation method is applied to investigate the impacts of HB networks on physical structures and mechanical properties of PVA/phytic acid systems.

CHAPTER 3: WATER GOVERNS THE MECHANICAL PROPERTIES OF POLY(VINYL ALCOHOL)

This is from the publication resulted from my PhD:

L. Li, X. Xu, L. Liu, P. Song, Q. Cao, Z. Xu, Z. Fang, H. Wang, Water governs the mechanical properties of poly(vinyl alcohol). *Polymer*, 2021, 213, 123330.

3.1 Introduction

Poly (vinyl alcohol) (PVA) features good biodegradability, water solubility, and, high mechanical properties, and thus has found extensive industrial applications in drug delivery (Chiessi, Francesca Cavalieri, et al., 2007) , membranes separation system (Florian Müller-Plathe, 1998; Pan et al., 2007), packaging (Chiessi, Cavalieri, & Paradossi, 2005; Jahanshahi, Rahimpour, & Mortazavian, 2012; Jose, Shehzad, & Al-Harthi, 2014), tissue engineering (Anseth et al., 2002), and hydrogels and microgels (Howard, Craig, FitzGerald, & Wanless, 2010; Kleinen & Richtering, 2011b; Städler et al., 2009). Recent research interests are focused on the design of mechanically robust PVA materials towards the applications such as high-performance films, fibers, and artificial ligaments and muscles (P. A. Song & H. Wang, 2020). Until now, a number of reinforcement agents have been explored to create strong PVA materials, including Mxene (Ling et al., 2014), graphene oxides (X. Yao et al., 2019), carbon nanotubes (Cui, Li, & Wang, 2020; Park & Lee, 2018), nanoparticles (Morimune et al., 2011; Song et al., 2018), small molecules (X. Huang et al., 2020; Song et al., 2013; Song et al., 2015a) and organic polymers (Song et al., 2017; Xiao Zhang, Liu, Yang, & Qiu, 2019). Unfortunately, as-used PVA matrices in the different conditions often exhibit very

different mechanical behavior during tensile tests (see Figure 3.1). This, however, renders it impossible to accurately compare the mechanical performances of the final PVA composites reinforced by different reinforcement agents.

More interestingly, such mechanical behaviors of PVA are clearly independent of the endopathic factors, such as the molecular weight and degree of hydrolysis, and the exopathic factors like the tensile rates during testing (see Figure 3.1). Therefore, there should exist another key factor that governs the mechanical properties of PVA behind. Our previous work has indicated that the different tensile behavior in PVA bulk is probably due to the drying conditions during the films preparation, which leads to different water content in PVA (Song et al., 2013; Song et al., 2015a). It is well known that water can have a significant impact on the mechanical behavior of PVA due to its high moisture sensitivity. Therefore, it is of paramount significance to reveal how water content (or the degree of hydration) affect the mechanical properties of PVA. Up to date such long-standing intriguing question has never been answered satisfactorily.

To date, molecular dynamics (MD) simulations have been intensively employed to unveil the effect of water content on the structure, glass transition and dynamics of PVA chain (Bermejo & Ugarte, 2008; Florian Müller-Plathe, 1998; Shi & Han, 2018; Tesei et al., 2012; Wolf & Suter, 1984; C. Wu, 2010). By contrast, only few experiments have been carried out to partially understand this phenomenon so far (Briscoe, Luckham, & Zhu, 2000; Hodge, Edward, & Simon, 1996; R. M. Hodge, T. J. Bastow, G. H. Edward, G. P. Simon, & A. J. Hill, 1996; Hongbin Li et al., 2000). Zhang et al. pioneered to use atomic force microscopy (AFM) to determine the elastic modulus of PVA in water and found that the HB governs the modulus of PVA (Hongbin Li et al., 2000). Briscoe et al. found that the viscosity of aqueous PVA solutions depend on the HB interactions (Briscoe et al., 2000). In addition, Hodge et al. revealed that the plasticization effect of water was due to the increased free volume of water, which caused the lubrication effect

once the water molecules disrupted the HB interactions among PVA chains (R. Hodge, G. H. Edward, et al., 1996; R. M. Hodge et al., 1996).

Given the above literature analyses, although great advances have been made on PVA systems containing various water content, three key questions remain unveiled. Specifically: (i) How do water content govern mechanical properties (tensile strength, elastic modulus, and ductility as well as toughness) of PVA? which has been ignored by materials scientists so far. This research gap makes it impossible to evaluate the mechanical reinforcement effect of different fillers on the PVA matrix accurately due to different water content (H. K. F. Cheng et al., 2012; Ling et al., 2014; Morimune et al., 2011; Song et al., 2018; Song et al., 2017; Song et al., 2013; Song et al., 2015a; Xiefei Zhang et al., 2003; Xiao Zhang et al., 2019) (see Figure 3.1); (ii) Current work mainly relies on the use of the MD simulation to understand the impact of water content on structure, glass transition and chain dynamics of PVA (Bermejo & Ugarte, 2008; Shi & Han, 2018; Song et al., 2015b; Tesei et al., 2012; Wolf & Suter, 1984; C. Wu, 2010), but lacks corresponding experimental validations; and (iii) to date only few experimental investigations have been performed on the effect of water on elastic modulus (Hongbin Li et al., 2000), viscosity (Briscoe et al., 2000), free volume and HB (R. Hodge, T. Bastow, G. Edward, G. Simon, & A. Hill, 1996; R. Hodge, G. H. Edward, et al., 1996) of PVA. Hence, there remains an urgent lack of an in-depth comprehensive insights on how water content govern the mechanical properties (strength, modulus, ductility, toughness) and molecular movements of PVA as well as their intermolecular H-bond interactions.

This study aims to employ MD simulation and experiment to understand the impact of water content on the mechanical property, glass transition, free volume, chain movements of PVA as well as their intermolecular HB interactions. Our results show that both tensile strength and elastic modulus of PVA steadily decrease while the strain-at-break increases first and then decreases with

increasing water content (up to 20 wt%). Only 1.8 wt% water can lead to a brittle-ductile transition during tension. The presence of water molecules can disrupt the HB interactions among PVA chains by replacing H-bonds between water and PVA, leading to reduced mechanical strength and elastic modulus, a decreased glass transition temperature and an increased mobility of PVA chains. This work helps us to understand the relationship between the water content and the mechanical performance of PVA, and the plasticization effect of water on PVA.

3.2 Experimental

3.2.1 Raw Materials

PVA with a Mw of $\sim 2.7 \times 10^4$ was purchased from Sigma-Aldrich, and its degree of hydrolysis was 98.0-98.8 %.

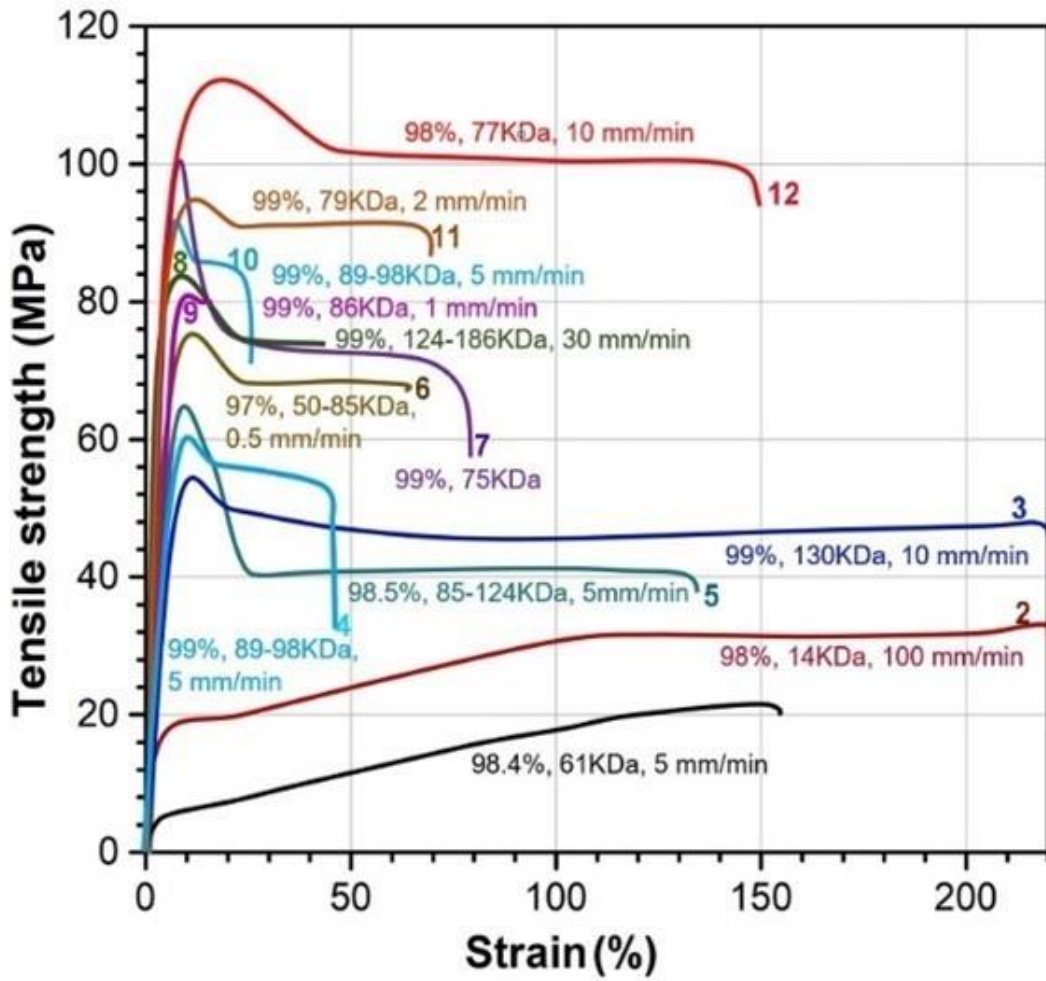


Figure 3.1 Representative tensile curves of the PVA films redrawn according to the work published previously

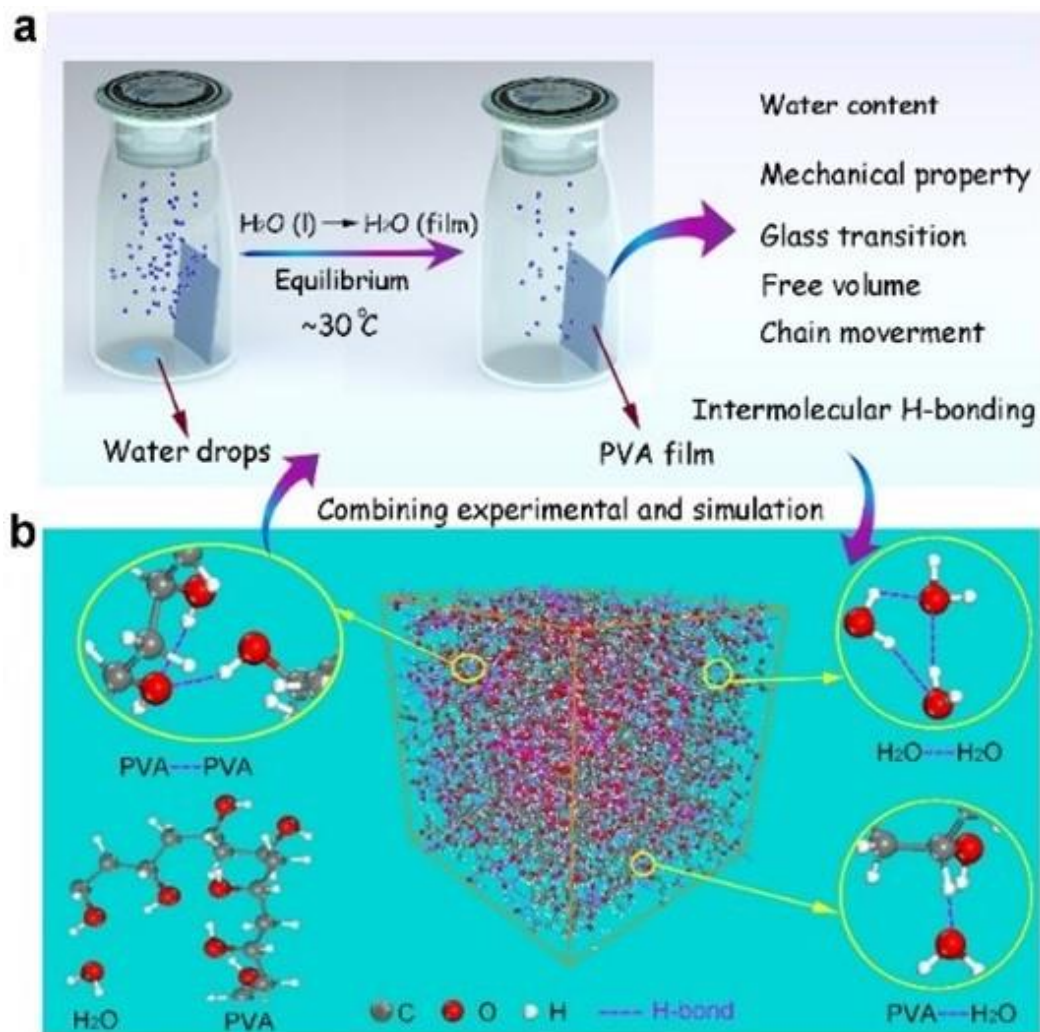


Figure 3.2 (a) illustration for the preparation of PVA films with control water content, and (b) models for molecular dynamic simulation of the PVA/water binary system.

3.2.2 Fabrication of PVA films

2.0 g PVA granules were dissolved in 38 g deionized water by heating to 70 °C to prepare a 5 wt% aqueous PVA solution. After cooling down to room temperature, the solution was slowly decanted into a glass mold followed by drying for 48 h at ambient temperature and then 3 h at 50 °C in an oven. These dry PVA films with typical thickness of 70 (± 10) μm were then cut into rectangular samples.

All the PVA films were dried at 80 °C under reduced pressure for 24 h to obtain absolutely dry PVA films (see the process in Figure 3.2a). All the dry films

were then divided into 9 groups and put into a glass bottle. A predesigned 1.0, 2.5, 5, 10, 15, 20, 30 and 40 wt% water was added into each bottle which were then sealed. The samples were designated as PVA-x, where x refers to the predesigned water content by mass fraction. The dry PVA was still named as PVA. The PVA films were kept in the sealed bottle at ambient temperature for a week to ensure the water content reach an equilibrium. The real water content in the predesigned PVA-x film was determined by the thermogravimetric analysis carried out in N₂ condition. After that x was replaced by real water content respectively. For example, 25 mg deionized water was injected into a 100 cm³ bottle containing 1 g of completely dry PVA film, then named PVA-2.5, and renamed as the PVA-1.8 according to its real water content (~1.8 wt%).

3.2.3 Characterizations

The tensile tests were measured on a SANS universal testing machine (CMT 6000) with a capacity of 200 N using a test rate of 5 mm/min at 23 ± 2 °C under a relative humidity of 30 %. As-prepared tensile specimens of PVA films were 30 mm long, 5 mm wide and 70 (±10) μm in thickness with a gauge length of 10 mm. The mechanical data reported in this work were the mean of quintuplicate measurements. Thermogravimetric analysis (TGA) was conducted using a Netzsch TG 209F1 Libra (TGA, Germany) at a heating rate of 3 °C/min in a temperature range of 35 ~ 180 °C in nitrogen to determine the real water content of PVA films. Each specimen was measured twice, namely, before and after tensile testing, and the average was reported as the real water content of the PVA film.

Differential scanning calorimetry (DSC) measurements were performed on a TA Q2000 instrument (DSC, USA). Typically, ~7 mg PVA were encapsulated in an aluminum pan, cooled down to - 40 °C, and held for 5 minutes before further process. After that all samples were heated from - 40 °C to 240 °C at scanning rate of 10 °C/min and kept 240 °C for 3 minutes (1st cycle), and then cooled to 10 °C at

the same rate and left for 3 minutes (2nd cycle) followed by reheating to 240 °C at the same rate (3rd cycle). The glass transition temperature (T_g) was determined as the midpoint of two tangent lines of the first cycle, and the enthalpy of vaporization of water and the melting enthalpy of PVA was obtained by integrating the peak of vaporization and melting using the TA universal analysis software using both 1st and 3rd cycle curve.

Positron annihilation lifetime spectroscopy (PALS) measurements were performed using a conventional Ortec fast-fast coincident spectrometer at room temperature (26°C). A ²²Na positron source was placed between two identical samples with a 15 mm in width, 15 mm in length and 1.0 mm in thickness. A million counts were collected from annihilation events. The time resolution of the spectrometer is about 270 ps (FWHM). The measurements were performed in a nitrogen atmosphere to avoid oxygen interference (Consolati, Genco, Pegoraro, & Zanderighi, 1996). For PVA-water systems, all of the PALS measurements were analyzed into three mean lifetimes, intensities, using PALSFIT (Olsen, Kirkegaard, Pedersen, & Eldrup, 2007).

When a positron is injected into polymer, two different states may exist, free positron and positron-electron bounded state (Ps). Ps can be divided into ortho-positronium (o-Ps) and para-positronium (p-Ps), due to the spin combination state of positron and electron. The shortest lifetime is the self-annihilation of para-positronium ($\tau_1 \sim 125$ ps). The intermediate lifetime ($\tau_2 \sim 400$ ps) is attributed to the annihilation of free positrons and positron-molecule species. The longest component ($\tau_3 > 600$ ps) was primarily due to the annihilation of ortho-positronium. Based on the fact that o-Ps is preferentially localized in lower electron density region before the annihilation occurs, such as a defect or free volume holes, and the mean lifetime of ortho-positronium are largely affected by the size and concentration of cavities. The most used model is a spherical well (with a radius of $R+\Delta R$) that has an infinite potential barrier with a homogeneous electron layer

in the region of $R < r < R + \Delta R$. Then, the correlation between the mean radius (R) of the free volume holes and the o-Ps lifetime (τ_3) can be expressed using the following semi-empirical equation (Tao, 1972):

$$\tau_3 = \frac{1}{2} \left[1 - \frac{R}{R + \Delta R} + \sin\left(\frac{2\pi R}{R + \Delta R}\right) \right]^{-1} \quad (3.1)$$

where R and τ_3 are expressed in the units of angstroms and nanoseconds, respectively. ΔR has been empirically found to be 1.656 Å (Jean, 1990). Based on spherical approximation, the mean volume of free volume holes can be calculated by this equation:

$$V_f = \frac{4}{3} \pi R^3 \quad (3.2)$$

where R is obtained from τ_3 using equation (3.1). Due to the correlation between the relative intensity of o-Ps annihilation (I_3) and the concentration of free volume holes, a semi-empirical equation has been summarized to determine the fraction free volume (FFV) in the following expression:

$$FFV = CV_f I_3 \quad (3.3)$$

where free volume V_f is in the units of Å³, and the relative annihilation intensity of o-Ps (I_3 in %) is obtained from PALS measurement. C is the empirical parameter that can be determined by calibrating with other physical parameters (Y. Wang, Nakanishi, Jean, & Sandreczki, 1990), such as free volume expansion coefficient (α_f). For each sample with T_g below measuring temperature (26°C), the fraction of free volume (FFV) also can be calculated using the following equation:

$$FFV = 0.025 + (T - T_g) \alpha_f \quad (3.4)$$

where it is assumed that the fraction of free volume at T_g is 0.025, the thermal free volume expansion coefficient (α_f) used in this work is $4.8 \times 10^{-4} \text{ K}^{-1}$ (Sperling, 2005). Then the mean value of parameter C can be obtained by above equation (3.3) and equation (3.4) simultaneously.

Infrared (IR) spectra of PVA films were recorded on a Thermo Nicolet iS10,

(Thermo Scientific, Germany) using the attenuated total reflectance (ATR) mode and the measurement was carried out at high-resolution spectra 2.0 cm⁻¹ resolution and 64 scans in the range of 675 to 4000 cm⁻¹. The IR spectrum of liquid water was recorded by dipping one drop of water on a KBr disk. To identify the H-bond types in water and PVA, the stretching vibration of hydroxyl groups (O-H) was analyzed by using peak analyzer fitting in the Origin 2017 software in the range of 3000 to 3800 cm⁻¹ based on Gauss formula (Equation 3.5 and 3.6, shown below) according to the previously-reported principles (X. Guo, Wu, & Yan, 2018; L F, Brown, & Richmond, 2001).

$$y = y_0 + \frac{A}{w \cdot \sqrt{\pi/2}} e^{-\frac{2(x-x_c)^2}{w^2}} \quad (3.5)$$

$$w = \text{FWHM} / \sqrt{\ln 4} \quad (3.6)$$

where y_0 was the baseline offset of the fitting curve, x_c was the peak position, A was the total peak area, FWHM was the full width at half maximum of the fitting peak. The x_c values of these peaks were kept constant, while the values of A and w were allowed to vary in the fitting process. And the peak position x_c is determined by IR subtraction spectrum (see supporting information Figure AS11).

3.2.4 Molecular Dynamics Simulations

In classical MD simulations, the positions and velocities of particles contained in the model system evolve as a function of time. The equations of motion are integrated using the Verlet velocity algorithm with a time step of 1 fs through the Materials Studio 8.0. The potential energy formalism which governing how the particles interact is an important ingredient in the MD simulations. In our case, we used the high-quality COMPASS force field (Condensed-phase Optimized Molecular Potential for Atomistic Simulation Studies), which has successfully applied on the prediction of the structural and dynamic features for many polymer materials (Shen et al., 2018; C. Wu & Xu, 2007). For the water

model, a simple three-point model is used in the COMPASS force field. The parameters including the bond length, bond angle and atom charges are similar to the TIP3P model. However, the bond-bond and bond-angle cross terms are also included. The system energy can be approximately estimated as the sum of different contributions. These contributions include the bonded and non-bonded interactions (see Figure 3.2b).

3.2.5 Establishment of Initial Model Systems

The structures of water and one single PVA chain with the repeat units of $n=99$ was generated for the PVA-H₂O system. Because as-used PVA in this work has a degree of hydrolysis of 98.0-98.8 %, the number of repeat units of the PVA chain was set to $n=97$ and two of the repeat units, namely, -CH₂-CHOH-, were replaced by -CH₂-CH(O) CH₃- for more precise calculation, such as T_g and elastic modulus. To obtain the minimum energy structure, we performed an energy minimization of the system through the conjugate gradient method algorithm to obtain appropriate input configuration for the following simulations. Then, model systems with different water content ($\phi= 0$ wt%, 1 wt%, 5 wt%, 10 wt%, 15 wt%, 20 wt%, 30 wt%) were constructed containing ten PVA chains in each system. The initial value of density for the configurations was assigned as 1.0 g/cm³. The periodic boundary conditions (PBC) were used to avoid surface effects. A set of ten configurations for each case were generated at the same time. Figure 3.2 shows the composition of PVA and water molecules in the amorphous cells. The size of the PBC box changes for different cases and simulation stages (such as deforming the box for calculation of mechanical properties). As an example, the box size at equilibrium is about 40.93 Å × 40.93 Å × 40.93 Å for 10 wt%.

The initial velocities of the atoms are generated by a temperature-dependent Gaussian distribution. The summation method to calculate long rang electrostatic interactions used the Ewald method with the accuracy of 0.001 kcal/mol. The

cutoff distance is set to 9.5 Å. To avoid being trapped in the local energy minimum conformations, one cycle anneal dynamics procedure was conducted. During the process, we use NPT (constant number, pressure and temperature) to ensemble and the temperature and pressure are controlled using Andersen and Berendsen methods, respectively. In the annealing cycles, the initial temperature was 300 K and the highest temperature was 500 K with 10 numbers of ramps per cycle. The simulation for each ramp was 10000-time steps at the pressure of 0.0001 GPa. And then the NPT simulations run 500 ps to obtain the equilibrium density at 300 K. Finally, we collected the production data for another NPT simulations for 20ns to analyze the trajectories of simulations and calculate the related system properties.

3.2.6 Calculation of Properties

The elastic moduli of PVA films can be calculated using static (Theodorou & Suter, 1986) or dynamic methods (D. Brown & J. H. R. Clarke, 1991). This work presented here was conducted with the dynamic method. In the method, the mechanical properties were evaluated through analyzed stress-strain curves. The strain rate set at $\dot{\epsilon}=10^8 \text{ s}^{-1}$. In the range of elastic deformation, the strain tensor ϵ can be simplified by neglecting the second order terms in the derivatives of displacement. The stress tensor σ changes linearly with ϵ . They are symmetric tensors: $\epsilon_{LM} = \epsilon_{ML}$, $\sigma_{LM} = \sigma_{ML}$. The relationship between strain and stress is expressed according to Hook's law in the range of elastic deformation: $\sigma_{LM} = C_{LMNL} \epsilon_{NK}$. By introducing the Voigt notation, the stiffness tensor for an isotropic material is simplified to

$$C = \begin{bmatrix} 2\mu + \lambda & \lambda & \lambda & 0 & 0 & 0 \\ \lambda & 2\mu + \lambda & \lambda & 0 & 0 & 0 \\ \lambda & \lambda & 2\mu + \lambda & 0 & 0 & 0 \\ 0 & 0 & 0 & \mu & 0 & 0 \\ 0 & 0 & 0 & 0 & \mu & 0 \\ 0 & 0 & 0 & 0 & 0 & \mu \end{bmatrix} \quad (3.7)$$

where, λ and μ are the Lamé constants. The Young's modulus (E) can be calculated

by λ and μ :

$$E = \mu \frac{3\lambda + 2\mu}{\lambda + \mu} \quad (3.8)$$

Through analysis of strain-stress curves, we can obtain the Lamé constants and further calculate the elastic constant.

The T_g of a semicrystalline polymer can be calculated through measuring FFV, mean square displacement (MSD), network topology density or molecular energy components. The free volume theory (Wei, Zhang, Wang, & Yang, 2017; Xie et al., 2018) was used to characterize the interactions of molecules. The FFV at 300 K can be calculated by the following equation 3.9.

$$FFV = \frac{v_f}{v_f + v_o} 100\% \quad (3.9)$$

where v_f and v_o are the free volume and the occupied volume, respectively.

The H-bonds are formed between three atoms through electrostatic interactions. In the traditional X-H---Y system, X and Y are donator and acceptor, respectively. Hence, the H-bonds were built between the hydrogen atom and two negatively charged atoms. The strength of the H-bonds is stronger than the van der Waals interaction but weaker than the covalent bond. In our simulations, the H-bonds were geometrically defined according to the criterion (Joseph & Aluru, 2008; Y. Tamai, H. Tanaka, & K. Nakanishi, 1996). The distance between X---Y is lower than $r=0.35$ nm and the angle of X-H--Y is less than $\theta=30^\circ$. Herein, the value of r corresponds to the first minimum of radial distribution between X and Y.

3.3 Results and discussions

3.3.1 Experimental design

Previously published research has been focusing on the effect of water on the plasticization of PVA, either by MD simulations (Bermejo & Ugarte, 2008; Tesei et al., 2012; Wolf & Suter, 1984; C. Wu, 2010) or by experimental (Briscoe et al., 2000; R. Hodge, G. H. Edward, et al., 1996; R. M. Hodge et al., 1996; Hongbin Li

et al., 2000). In order to systematically investigate the effect of water content on the mechanical properties, molecular movement and intermolecular interactions of PVA, a series of PVA films with varied water content are prepared by sealing the dried PVA films in a glass bottle containing pre-designed water content (see Figure 3.2a). The actual water content in the final PVA films are determined by TGA (see Figure AS1), with their digital images films presented in Figure AS2. It was observed that the PVA film became soft and plasticine-like for PVA- 17.5 and even sticky at a water content of 30.2 wt%. In order to accurately evaluate the mechanical properties of PVA, the real water content is controlled at less than 20 wt%. Mechanical performances, T_g , FFV, the relaxation and intermolecular HB interactions of PVA are fully examined. MD simulations are used to calculate these parameters (see Figure 3.2b), and the simulated values are then compared with the experimental results. This is designed to achieve a more comprehensive understanding on how water determines the mechanical properties of PVA.

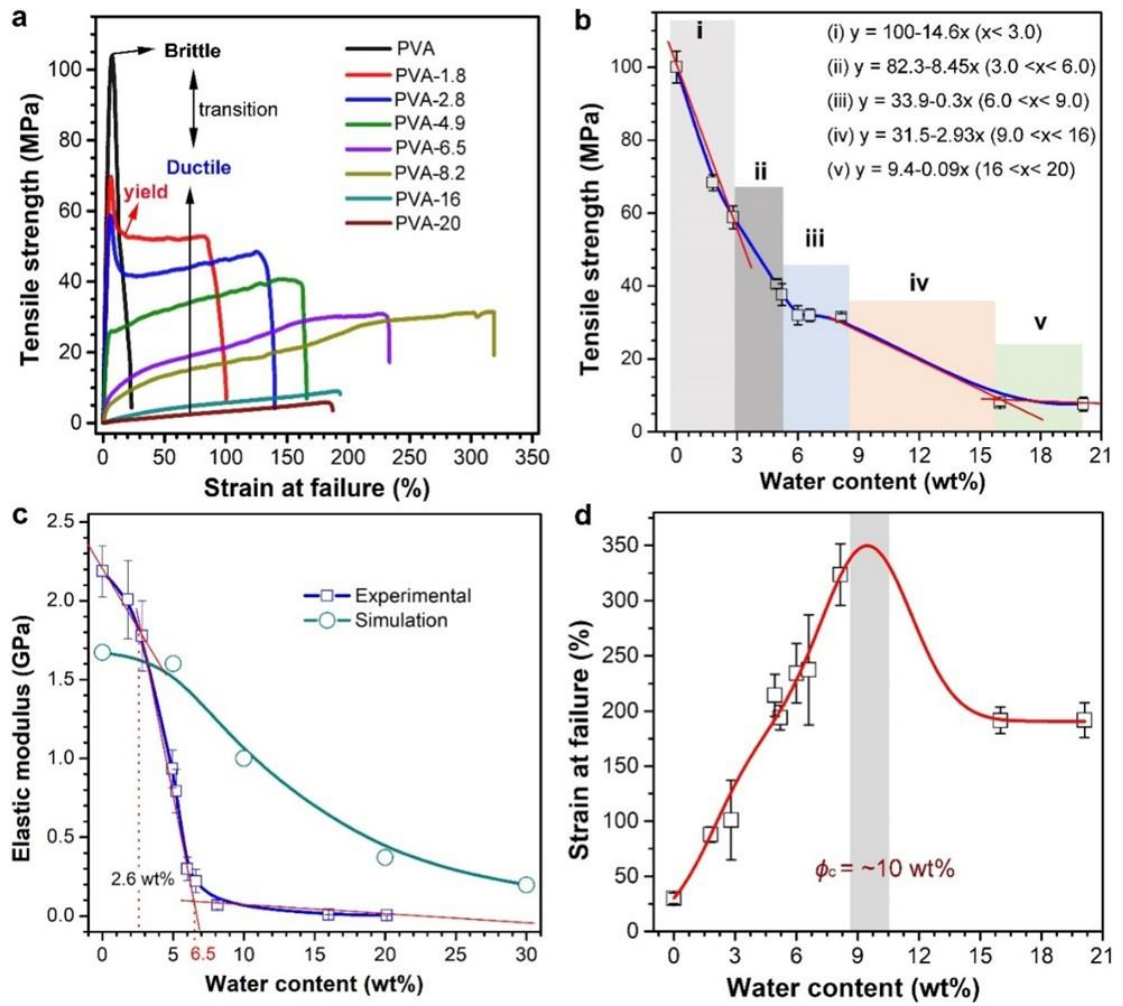


Figure 3.3 (a) Typical tensile stress-strain curves, (b) tensile strength, (c) elastic modulus, and (d) strain at failure of PVA films with varied water content (ϕ).

Table 2.1 Detailed mechanical properties including tensile strength, modulus, stain at failure, obtained from tensile tests as well as elastic modulus predicted by MD simulation.

Run	σ_y^a (MPa)	σ_m^a (MPa)	E^a (MPa)	ε_b^a (%)	τ^a (MJ/m ³)	E_s^a (MPa)
PVA	–	100± 4.3	2190±160	25 ± 5	18.7±5.6	1672
PVA-1.8	68.4±2.2	68.4±2.2	2010± 250	88 ± 7	44.3±3.7	–
PVA-2.8	58.8±3.1	58.8±3.1	1780± 220	101±36	48.7±3.6	–
PVA-4.9	25.3±2.0	40.5±1.3	934 ± 120	214±19	73.3±9.0	~1607
PVA-6.5	9.52±0.8	32.0±1.7	222 ± 70	237±50	54.5±4.7	–
PVA-8.2	6.11±0.9	31.4±0.95	68.6 ±30	324±28	68.1±6.7	~1005
PVA-16	3.18±0.6	7.93±0.94	9.39 ± 0.5	191±12	9.36±1.0	–
PVA-20	0.5±0.08	7.55±0.94	3.90 ± 0.5	192±16	7.91±1.5	~371
PVA-30	–	–	–	–	–	~197

^a σ_y , σ_m , E , ε_b , τ , and E_s respectively refer to yield strength, tensile strength, elastic modulus, strain at break, toughness, and the elastic modulus by MD.

3.3.2 Mechanical performances

The tensile stress-strain curved of PVA with different water content is shown in Figure 3.3, and the results are summarized in Table 3.1. the absolute dry PVA film exhibits a typical brittle failure without yield. It shows a high tensile strength (σ_m) of around 100 MPa, a high elastic modulus (E) of 2.19 GPa (comparable to the simulated value ($E_s = 2.31$ GPa)), and a break strain (ε_b) of only 25%. In a sharp contrast, the water-containing PVA films start to behave in a ductile manner, even at a very low water content (φ) of only 1.8 wt%. The ductile failure behavior becomes more and more significant with increasing water content, in addition to an obvious yield phenomenon. Such plasticization effects are similar to those observed in the PVA/glycerol binary systems (T. Liu et al., 2018). Only a small amount of water can significantly decrease both strength and modulus of PVA, as reflected in the PVA-1.8 sample with a σ_m of 68.4 MPa (~31.6% reduction). The

decrease of tensile strength with water content can be roughly classified into five water-content zones (see Figure 3.3b). The σ_m reduces sharply in a water content within 3 wt%, at a high slope of 14.6, which is followed by a relatively smaller slope of 8.45 in a water content range from 3 to 6 wt%. Then σ_m change levels off at a water content of 6 – 9 wt% followed by a further notable reduction with the water content increasing from 9 to 16 wt%.

In comparison with the strength, the elastic modulus basically has a rapid reduction as the water content increases up to 8.0 wt%, and then decreases slowly with further increase in water content. The MD simulation shows an overall higher modulus than the experimental one in the entire water content range except for the PVA matrix. This is because the simulation is based on perfect PVA/water systems without any defects. In reality, it is nearly impossible to avoid the generation of defects, such as the introduction of dusts, during the casting and drying of the PVA films. The defects can significantly reduce the modulus values of the final PVA films. Moreover, it is well-known that the experimental modulus values of PVA films are strongly dependent on the tension rate during tensile tests, e.g., a high the tension rate usually leading to a higher modulus of the PVA film.

In addition, the experiment results show a gradually reduced degree of crystallinity with increasing water content (see Figure AS3), which accounts for the decreased E_s . Generally, the polymer crystallinity is defined as the ratio of crystalline phase in the bulk polymer, and is closely related to ordered arrangements of polymer chains, which renders it nearly impossible to calculate the crystallinity degree by the MD simulation. Instead, the previous work of MD simulations has focused on the conformational features in crystallization process to understand the polymer crystallization (Lavine, Waheed, & Rutledge, 2003). In present MD simulations, the polymer crystallization is characterized by torsion changes of backbone (the extensional deformation of backbone segments). The relationship between the torsion angle of the backbone and the temperature for

varied water content is illustrated in Figure AS4. The enhancement of crystallization corresponds to reduced torsion of the backbone, as reflected by a smaller backbone torsion of PVA-2.5 than PVA-15, agreeing well with the DSC results (Figure AS3). Meanwhile, the calculated Poisson's ratio is around 0.3, agreeing well with the typical values (0.2 – 0.4) of polymer materials (Ma, Xiao, Yin, & Xiao, 2005).

On the contrary, the break strain (ϵ_b) or the ductility of PVA increases from 25% (0 wt% water) to 324% (8.2 wt% water), indicative of a 12-fold increase. With further increasing water content, the strain-at-failure decreases then becomes steady. In addition, the toughness (τ) achieves a peak value of 73.3 MJ/m³ at a water content of ~4.9 wt%, as compared to 18.7 MJ/m³ for the dried PVA. The reduced strength and modulus as well as increased ductility strongly demonstrate that the presence of water can affect the macroscopic mechanical deformation of PVA through interfering its chain movement and crystallinity as well as intermolecular HB interactions. Shi *et al.* has recently revealed that the water content significantly influences mechanical properties and deformation mechanisms of PVA hydrogel with water content under uniaxial tensile conditions by using MD simulation (Shi & Han, 2018).

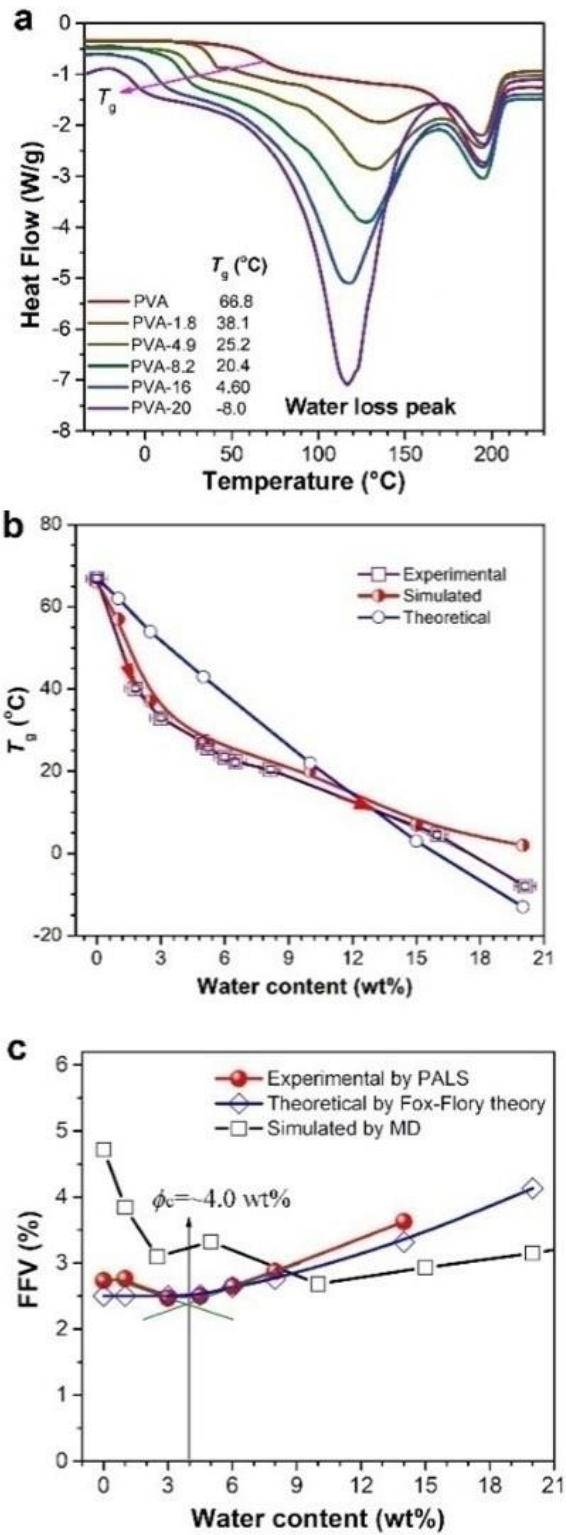


Figure 3.4 (a) The first heating cycle of PVA with various water content, and the experimental, simulated and theoretical (b) T_g values, and (c) of FFV of PVA as a function of water content.

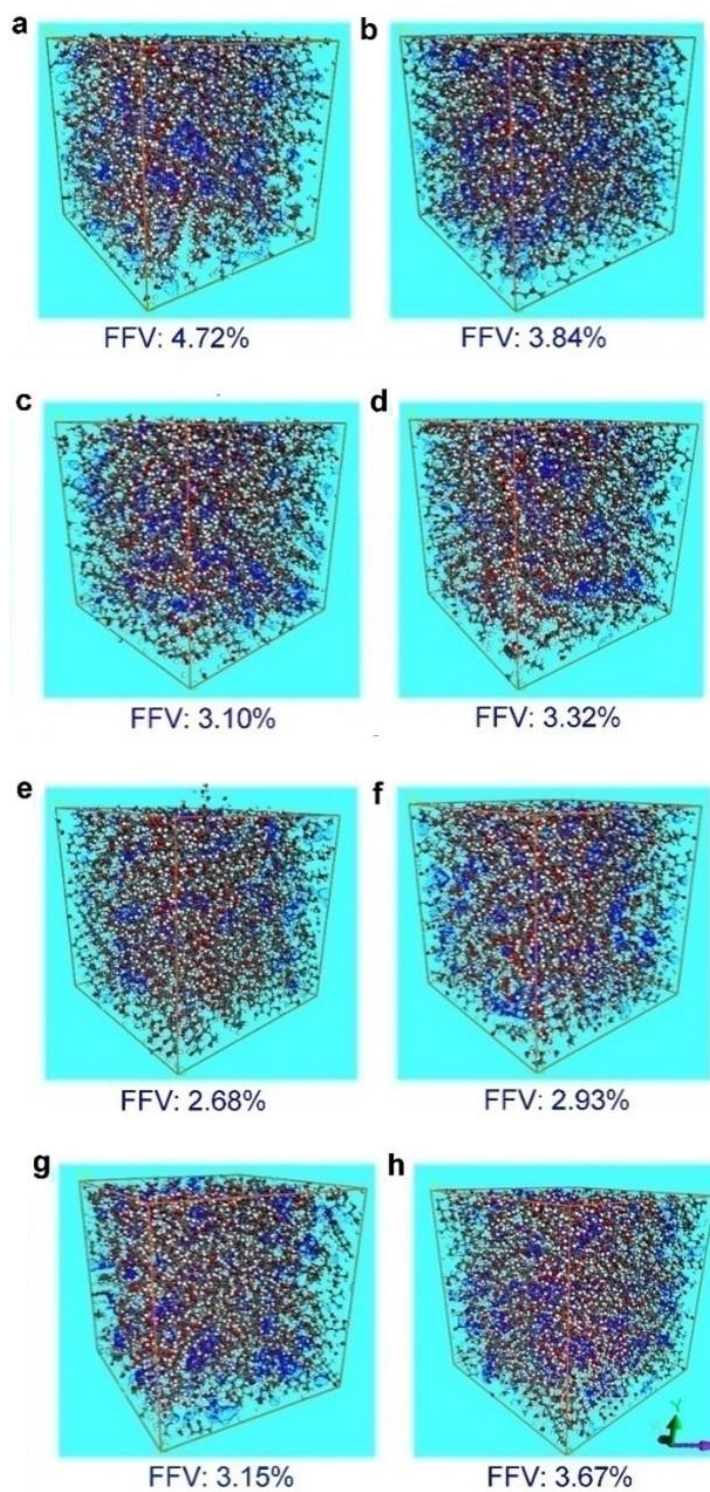


Figure 3.5 Snapshots of FFV for PVA with various water contentswater content calculated by MD simulation. (a) PVA, (b) PVA-1.0, (c) PVA-2.5, (d) PVA-5.0, (e) PVA-10, (f) PVA-15, (g) PVA-20, and (h) PVA-30. (The blue cloud and gray cloud represent the outside or free volume

3.3.3 Glass transition temperatures and free volume

In addition to the mechanical property, the T_g is another critical macroscopic feature of polymer material because it determines the temperature uplimit of their practical applications. Physically, the T_g of a semicrystalline polymer reflects the movement of the polymer segments and its intermolecular interactions, and thus affects the macroscopic mechanical property. We use DSC to determine the T_g change of PVA films as a function of water content (see Figure 3.4a and Figure AS5). The T_g of PVA shows a gradual decrease with increasing water concentration, which is also previously observed by Hodge *et al.* (R. M. Hodge et al., 1996). Interestingly, such change trend of T_g appears similar to the tensile strength (see Figure 3.4b), indicative of their similar dependences on water content. The dry PVA gives a high T_g of 66.8°C whereas only 1.8 wt% of water leads to a sharp drop in T_g to 38.1°C, and the T_g continues to decrease to 20.4°C for PVA-8.2 and even to -8.0 for PVA-20 (see Table AS1). This strongly demonstrates that the presence of water promotes the movement of PVA segments, thus reducing T_g .

To gain a better understanding of the effect of water concentration on T_g of PVA, the T_g is also calculated by MD simulations and the following Gordon-Taylor equation 3.10 (Briscoe et al., 2000).

$$\frac{1}{T_g} = \frac{w_1}{T_{g1}} + \frac{w_2}{T_{g2}} \quad (3.10)$$

Where T_{g1} and T_{g2} denote the glass temperature for pure PVA (67°C was used as determined by the DSC for better comparison, instead of the previously reported 85°C (Sakurada, 1985)) and bulk water (-139°C), respectively (Angell, Sare, & Sare, 1978), and w_1 and w_2 are their mass fractions. The theory values of the glass temperature for each system are presented in Table AS2.

In order to calculate the T_g of PVA at different water content, the plots of density – temperature curves should be established. In the simulation, we run high number of cycles of dynamics at different temperatures and the density of each

system is calculated after equilibration. To enhance the simulated accuracy, a step size of 5 °C was chosen for each run dynamics. The simulated T_g can be obtained by identifying the intersection point of two linear fitting curves of the density – temperature plots, since the density of the polymer shows a turning point appears in the vicinity of T_g (see Figure AS6). As shown in Figure 3.4b and Table AS2, the simulated T_g values of PVA agree well with the experimental ones in the whole water content range of 0 wt%-20 wt%, except for a relatively large deviation the PVA-20. However, as-simulated T_g of PVA-20 is 286 K, very close to ~ 293 K of PVA containing 21 wt% water (C. Wu, 2010). In comparison, the theoretical T_g s by the Gordon-Taylor equation exhibit certain deviations from the simulated and experimental values in the water content range from 1.0 wt% to 10 wt%, but are in good consistence to the experimental ones at the water content above 10 wt%. Moreover, it is easy to understand such differences in the experimental T_g values from those by the MD simulation and the Gordon-Taylor equation, if the impact of the simulated cooling rate and intermolecular HB between water and PVA on the T_g values are considered. Overall, the experimental T_g values of PVA exhibit a similar trend to both the simulated and theoretical values as the water concentration increases (see Figure 3.4b). It is understandable that the increased water molecules can promote the mobility of PVA segments and reduce the activation energy for the glass transition. The MD simulation results have revealed that the glass transition of PVA-water composite depends on the cooperative behavior of PVA and water. This behavior involves the HB interaction between PVA and water as well as the HB among the PVA chains and the water molecules themselves (Kleinen & Richtering, 2011b; C. Wu, 2010). Therefore, it is reasonable to conclude that the HB interactions between the PVA chains play a key role in determining the T_g in the presence of water.

In addition, the T_g is closely related to the free volume, especially fraction free volume (FFV) of a polymeric material. In fact, the simulated T_g is calculated

on the basis of the FFV parameter. The FFV can be used to predict the relative size of free space and the dynamic of the polymer matrix. The dry PVA shows a FFV of 2.74% very close to 2.5% given by the Fox-Flory theory. With increasing water content, the FFV values of PVA determined by the PALS measurements first decline and then rebound after hitting the rock bottom at a water content of ~4.0 wt%, as presented in Figure 3.4c and Table AS2. Moreover, the Fox-Flory theory can predict the FFV very well as the water content is higher than 3.0 wt%, as reflected by its very close FFV values to those measured by PALS. However, when the water content is in the range of 0~3.0 wt%, the theory fails to predict the real FFV value of PVA. This is mainly because the Fox-Flory theory assumes that the FFV is a constant when the measurement temperature (herein, 25°C) is lower than the T_g of the polymer (Sperling, 2005).

Interestingly, the simulated FFV values show a “W” shape trend with increasing water content. As compared with experimental and theoretical FFV values, it seems that the MD simulation fails to predict the FFV value well at water content less than 8.0 wt%, as reflected by relatively large deviations in the water content range (see Figure 3.4c and Table AS2). When the water content is above 8.0 wt%, the FFV values obtained by three methods nearly share a growingly upward tendency with increasing water content. Figure 3.5a-h gives the snapshots for the isosurfaces corresponding to the Connolly surface (Connolly, 1983) at different water content at 300 K and 0.1 GPa as well as their corresponding FFV values.

In fact, it is not difficult to understand such a change trend in FFV of PVA films as a function of water content. On one hand, the addition of water increases the interchain distance and FFV of PVA bulk because of the volume effect of water molecules; on the other hand, the strong HB interactions enable water molecules to occupy the free space among polymer chains, thus reducing the FFV. Hence, the FFV value of PVA is primarily determined by the trade-off or competition of these

two opposite effects. At a very low water concentration ($\phi < 4.0$ wt%), the strong HB interactions dominate, water molecules enter the interchain space whereas their volume effect is negligible, thus resulting in gradually decreased FFV with increasing the content of water. As the water content (ϕ) approaches a critical value, herein, ~ 4.0 wt%, the volume effect of water is comparable to the intermolecular HB effect, and thus the FFV reaches the bottom value. With further increased water content, the volume effect of water molecules suppresses the intermolecular HB one. Meanwhile, because of the strong HB interactions between water molecules themselves tend to form water clusters with much large volume. As a result, the FFV shows a steady increase as water content increase.

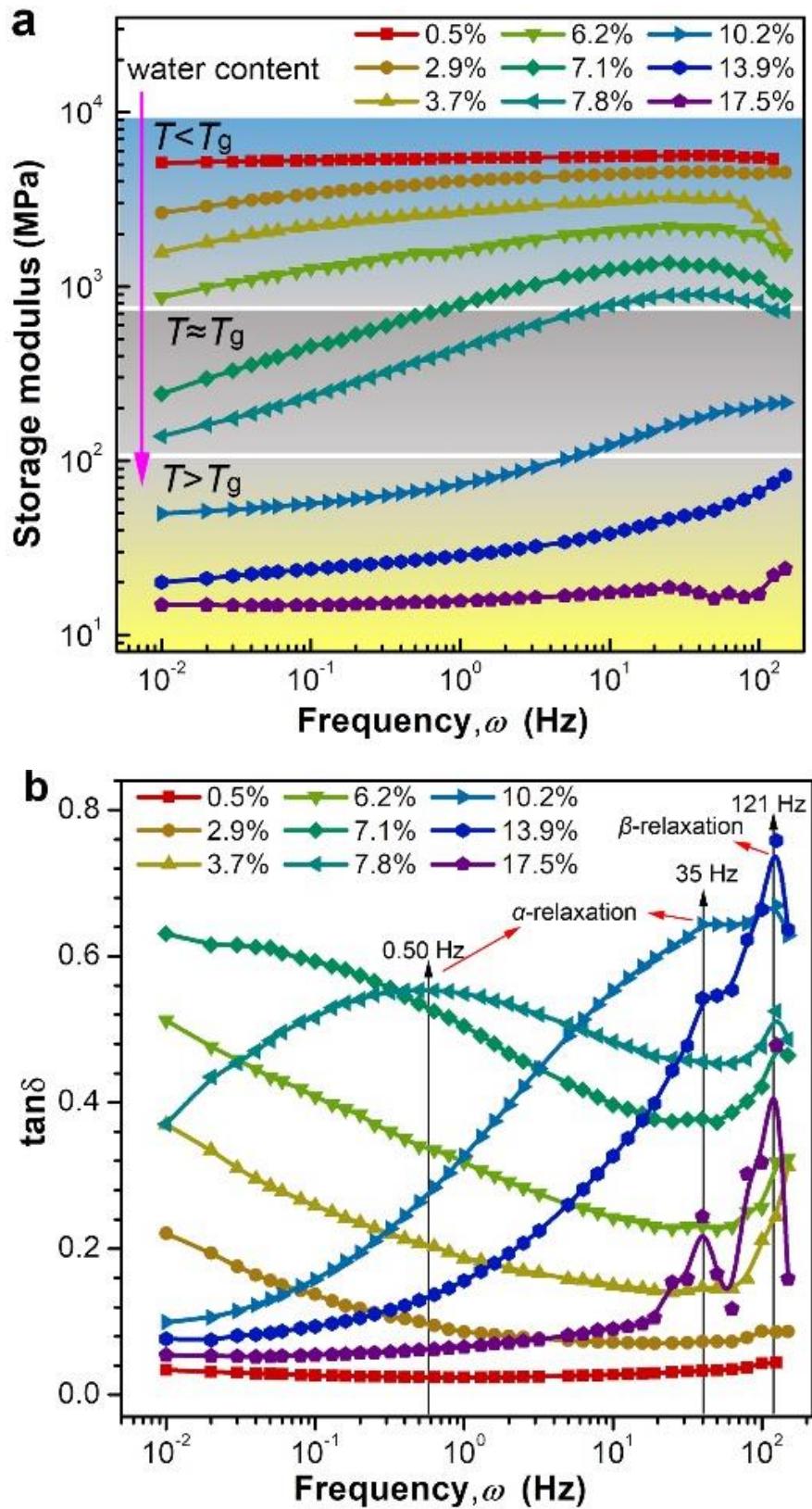


Figure 3.6 Frequency dependence of (a) storage modulus (G') and (b) loss factor ($\tan \delta$) at 25 °C for PVA films with varied water content.

Table 2.2 Dynamic mechanical properties of PVA films with varied water content by controlling the relative humidity (RH) of the sample chamber and as-obtained characteristic relaxation times (τ_r).

Run	Water content (wt%)	RH (%)	T_g (°C)	ω at $\tan\delta$ peak (Hz)	$\tau_r = 1/\omega$ (ms)	$T \sim T_g$
PVA-0.5	0.5	1.0	63.9	–	–	$T < T_g$
PVA-2.9	2.9	25	37.3	–	–	
PVA-3.7	3.7	47	32.8	–	–	
PVA-6.2	6.2	56	25.4	35	29	
PVA-7.1	7.1	62	23.3	35	29	$T \approx T_g$
PVA-7.8	7.8	66	21.8	0.5/121	2000/8.3	
PVA-10.2	10.2	76	17.0	35/121	29/8.3	$T > T_g$
PVA-13.9	13.9	83	9.51	35/121	29/8.3	
PVA-17.5	17.5	90	1.33	35/121	29/8.3	

3.3.4 Relaxation and Dynamics of PVA chains

The viscoelastic behavior can reflect the relaxation and movement of polymer chains in the presence of another component. In order to maintain the water content during DMA measurements, the water content of PVA films are controlled by the relative humidity (RH) of the test chamber. As presented in Figure 3.6, the storage modulus of PVA exhibits a gradual decrease with increasing water content in the whole frequency range. For example, at 1.0 Hz, a storage modulus of ~5000 MPa is achieved for the PVA-0.5 (0.5 wt% water), ~2500 MPa for PVA-3.7, ~500 MPa for PVA-7.8, and ~15 MPa for PVA-17.5. According to the relationship between the T_g and water content, one can calculate the T_g of PVA with varied water content, with detailed data listed in Table 3.2. When the water content is < ~6.2 wt%, the measurement temperature (T) is higher than the T_g value of PVA films, namely $T > T_g$. Therefore, one cannot observe the relaxation of PVA chains

and the loss peaks (see Figure 3.6b). As the water content in the range of 6.2~7.8 wt%, the T_g values of PVA films approach the T , namely $T \approx T_g$, where the PVA segments start to move and to relax more quickly as the water content increase. For both PVA-6.2 and PVA-7.1, there appears a very weak loss peak at 35 Hz probably corresponding to a characteristic relaxation time ($\tau_r = 1/\omega$) of 29 ms of side hydroxyl groups of PVA, namely the β -relaxation (T. Liu et al., 2018). Unexpectedly, a very broad loss peak is observed at 0.5 Hz, which is presumably due to a very long-time relaxation ($\tau_r = 2000$ ms) or the α -relaxation of the PVA. Such α -relaxation is attributed to the movement of PVA segments because at this water content the environmental T is moderately higher than the T_g of PVA, thus providing thermal energy. Moreover, there is another loss peak at a high frequency of 121 Hz ($\tau_r = 8.3$ ms) due to the β -relaxation of side hydroxyl groups ($\tau_r = 8.3$ ms). Interestingly, with further increase in the water content, the $T > T_g$, another loss peak is determined at a higher frequency at 121 Hz ($\tau_r = 8.3$ ms), in addition to the α -relaxation peak at 35 Hz ($\tau_r = 29$ ms). Moreover, both the intensity of loss peaks turns stronger with increasing water content, strongly indicating that they are closely related to water molecules. The loss peaks at 35 and 121 Hz are respectively to the relaxation of PVA segment and side hydroxyl groups because the HB between PVA and water can further reduce their vibration energy.

The diffusion behavior of PVA chains significantly depends upon the water content and their interactions. The diffusion coefficient (D) of polymer chains or small molecules can be calculated by using the following Einstein relation (Equation 3.11).

$$D = \frac{\left\langle \left| \vec{r}_i(t) - \vec{r}_i(0) \right|^2 \right\rangle}{6t} \quad (3.11)$$

where $\vec{r}_i(t)$ is the diffusion trajectory of molecule i and t represents the time.

$\left\langle \left| \vec{r}_i(t) - \vec{r}_i(0) \right|^2 \right\rangle$ denotes the MSD by averaging over all possible time origins as

well as all molecules in the simulation. If there are N equivalent permeant molecules, the MSD can be denoted as following:

$$MSD = \frac{\sum_{i=0}^N D_i}{N} \quad (3.12)$$

The MD simulations have previously demonstrated that the PVA chains affect the diffusion dynamics of water (Florian Müller-Plathe, 1998; C. Wu, 2010), and *vice versa* the amount of additional small molecules also influences the dynamics of polymer chains (Mora-Barrantes, Rodríguez, Ibarra, González, & Valentín, 2011; Qiao, Zhao, Yue, Zhang, & Wu, 2012). As shown in Figure 3.7, the increase of the water content results in faster diffusion of both PVA (Figure 3.7a) and water (Figure 3.7b), and meanwhile, the water molecules diffuse more rapidly than the PVA chains. Unlike the water molecules whose diffusion steadily continue to increase, the diffusion of PVA chains gradually increases as the water concentration increases to ~5.0 wt%, which is followed by a moderate decrease as water content increases to ~10 wt%. With further increasing water content, the PVA chains diffuse quickly again and continue to become faster as water content reach 30 wt%. Such interesting diffusion trend of PVA and water can be reflected by their D values as a function of water content (see Figure 3.7c).

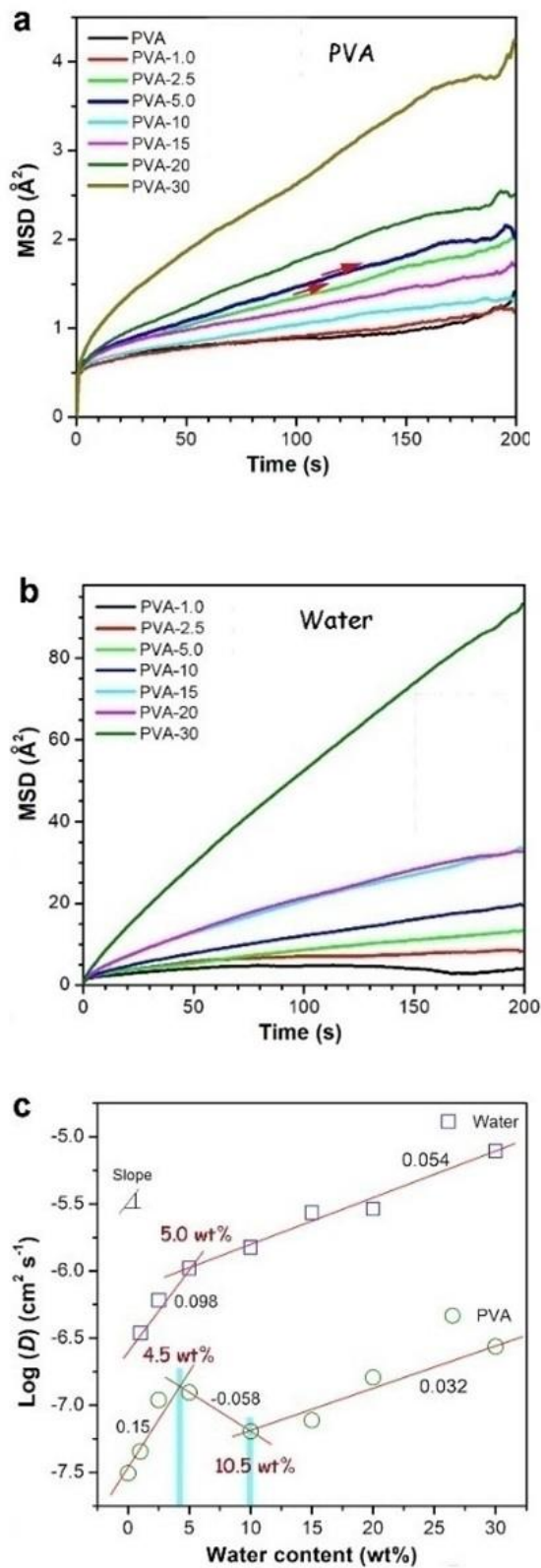


Figure 3.7 MSD as functions of simulation time for (a) PVA and (b) water and (c) their diffusion coefficient (D) at 300 K.

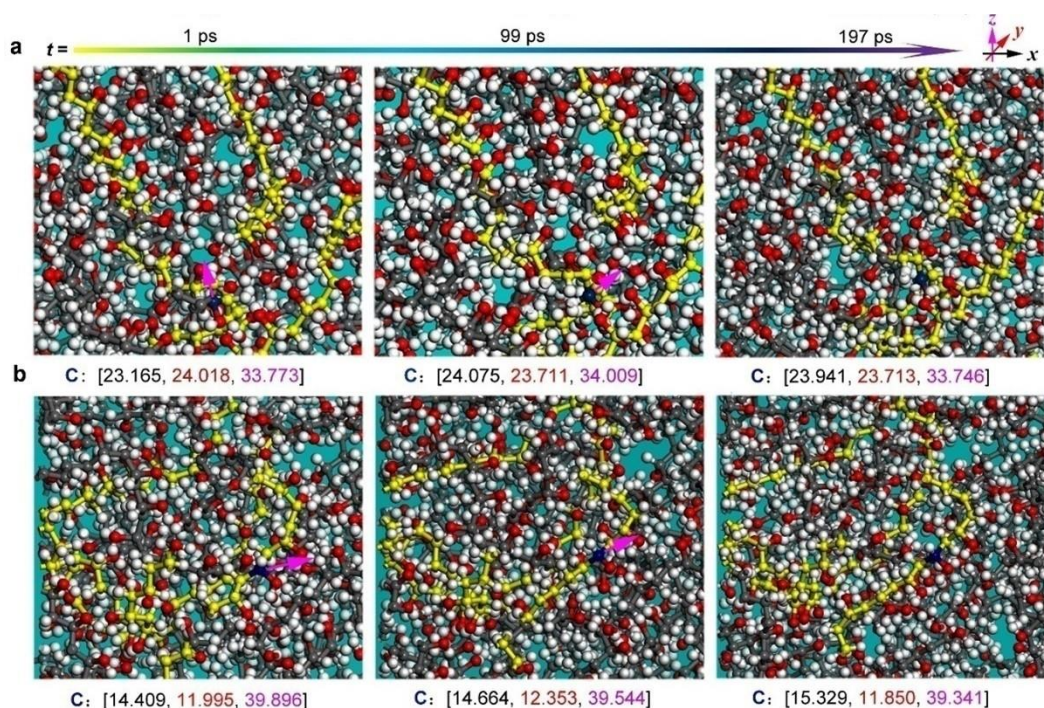


Figure 3.8 Snapshots of MD simulation showing the motion trajectory of extracted PVA chains from (a) PVA-1.0 and (b) PVA-10 after 1ps, 99 ps and 197 ps. One PVA chain is marked in yellow with one carbon atom and highlighted in dark blue for showing the movement of PVA chains. The three numbers in the brackets refer to x, y and z coordinates of the marked carbon atom, respectively.

It is easy to understand that water molecules diffuse faster with increasing water content mainly because of their smaller size and higher degree of freedom than long PVA chains. Another reason is that at a low water content the water molecules are confined within the PVA chains due to their strong HB interactions. As the water concentration increases, water molecules can also increase the interchain distance of PVA, thus leading to more free space for water molecules to diffuse. In comparison, at a relatively low water content less than 5.0 wt%, the intermolecular HB among PVA chains is partially replaced by the HB interactions between PVA and water. As a result, the small water can also promote the diffusion of PVA chains that form strong HB with water. On the other hand, the increase in water content also leads to reduced free volume of the PVA bulk, as reflected by the smallest FFV at a water content of ~4.0 wt% (see Figure 3.4c), thus allowing

less space for PVA chains to diffuse. With further increasing water content, the diffusion of PVA chains accelerates again because of the gradual increased FFV and the lubricative effect of water clusters. In addition, the snapshots of MD simulation provide a visual evidence that the PVA chains move faster in the PVA-10 than in the PVA-1.0 system with time (see Figure 3.5a and 3.5b). Meanwhile, both the PVA chains and water molecules move more quickly as the water content increases from 1.0%, to 5.0%, to 10% and then 20% (see Figure AS7-10).

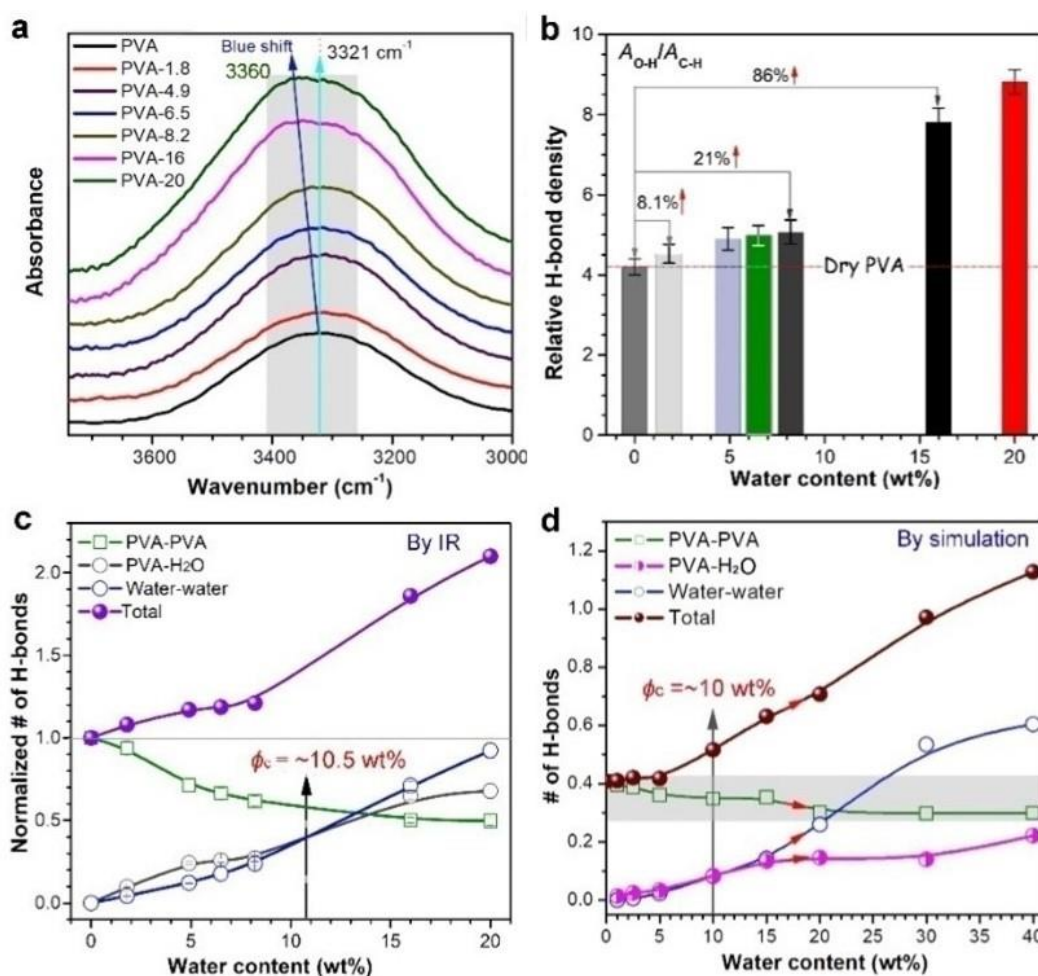


Figure 3.9 H-bond interactions between PVA and water. (a) ATR-IR spectra, (b) relative H-bond density for PVA films as a function of water content. (c) Experimental and (d) simulated (at 300 K) changes in the number (#) of different H-bonds of PVA films as a function of water content

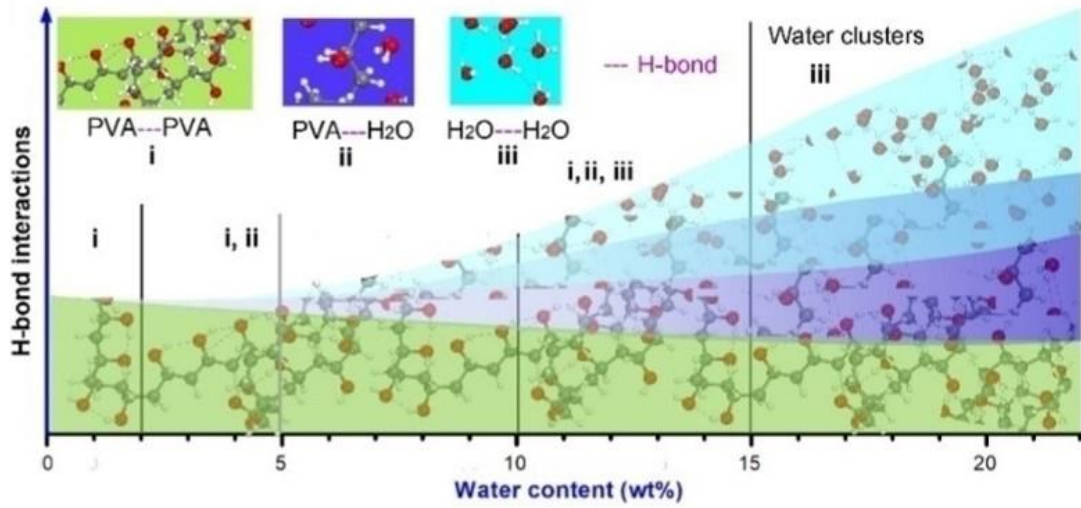


Figure 3.10 Illustration of dominant H-bond interactions in the PVA with increasing water content.

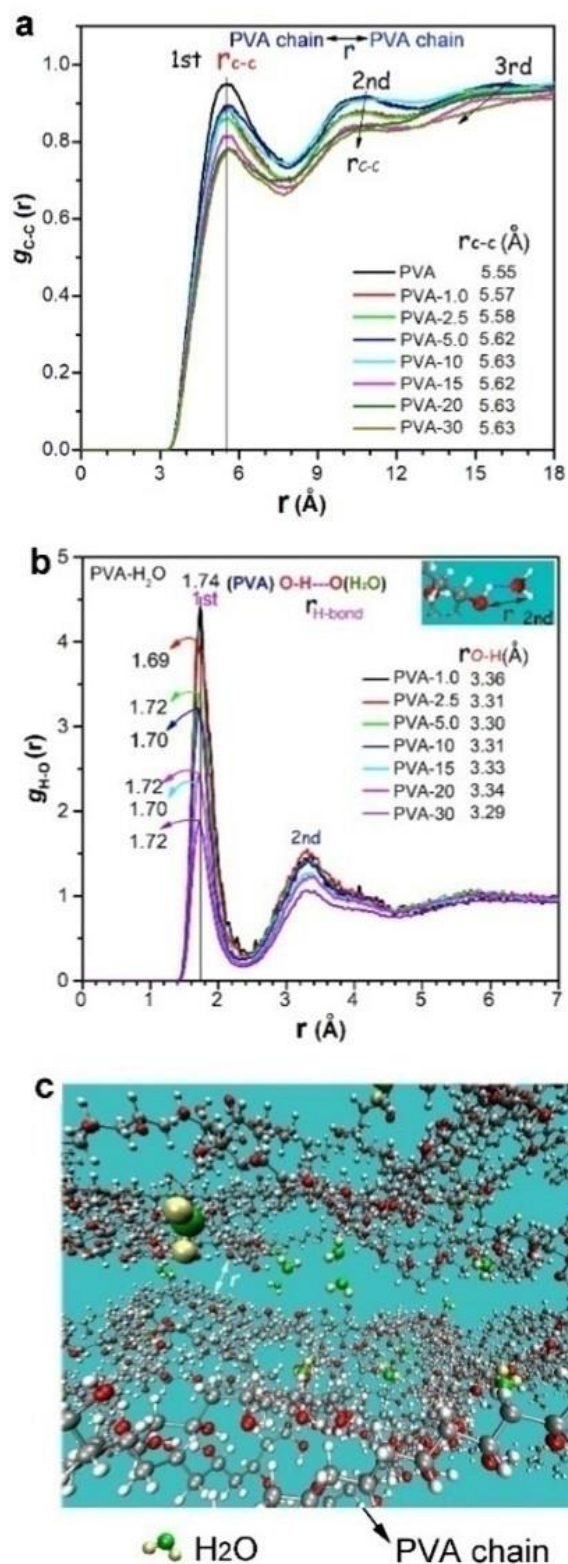


Figure 3.11 Radial distribution functions (RDFs) of samples with various water content showing intermolecular distance for (a) $g_{c-c}(r)$ between PVA chains, (b) $g_{H-O}(r)$ between PVA chains and water molecules and (c) the interaction between water and PVA.

3.3.5 Intermolecular interactions and interchain distances

HB interactions have been revealed to govern the mechanical properties of PVA (Shi & Han, 2018), and the inclusion of water inevitably affects the HB interactions of PVA because of the saturated feature of H-bonds, and the strong capable of forming HB with water. The H-bonds formed between water and PVA can replace those among PVA chains, which can weaken the interactions of PVA chains and thus influence the mechanical performances and molecular movements of PVA. As shown in Figure 3.9a, the stretching vibration peak ($\nu_{\text{O-H}}$) of hydroxyl groups of PVA gradually shift to higher wavenumbers with increasing water content. For instance, the $\nu_{\text{O-H}}$ of PVA-20 (3360 cm^{-1}) exhibits a blueshift as high as 39 cm^{-1} as compared to the dry PVA (3321 cm^{-1}) (Jiajun Li et al., 2020). Moreover, the relative HB density of PVA films also steadily augments as the water content increases because water molecules can form much more H-bonds than PVA. The peak analyzer fitting is employed to further confirm the HB interactions between PVA and water and identify the types of HB by using subtraction spectrum (see Figure AS11) (X. Guo et al., 2018). For the dry PVA, it shows a relatively broad absorption peak of hydroxyl groups ($\nu_{\text{O-H}}$) of centered at 3321 cm^{-1} (see Figure 3.9a), while the water shows a vibration peak at 3445 cm^{-1} corresponding to stretching vibration of O–H in water molecules (see Figure AS11b). By using the subtraction spectrum method, a new absorption peak at 3245 cm^{-1} appears and turns stronger with increasing water content, which is attributed to the H-bonded O–H groups between PVA and water. Meanwhile, the absorption peak of O–H in water molecules shifts to 3408 cm^{-1} . By fitting three vibration peaks of O–H at 3408 cm^{-1} (H₂O–H₂O), 3321 cm^{-1} (PVA–PVA) and 3245 cm^{-1} (PVA–H₂O), their relative contents can be calculated by fitting with using Origin 2017 software. Upon the introduction of water molecules, water molecules will either form

intermolecular HB with PVA and/or intramolecular HB among water molecules depending on the water content in the PVA. The absorption peaks of different types of water are strongly dependent on the HB, and the HB between water and PVA can give rise to a red shift (X. Guo et al., 2018; L F et al., 2001). With the aid of the peak analyzer fitting, two more absorption peaks are fitted respectively centred at 3498 cm^{-1} belong to H-bonded O-H of water-water and 3320 cm^{-1} arising from the H-bonded O-H of water-PVA. This can be evidenced by their steadily increasing relative contents with increasing water content (see Figure AS11).

In addition, the MD simulation shows that the interactions energy between PVA and water also increases with increased water content (Figure AS12). This clearly indicates the strong HB interactions between PVA and water molecules. After fitting the total H-bonds using the Origin software (see Figure AS11), one can normalize the respective number (#) of three types of H-bonds, namely the H-bonds of PVA-PVA, PVA-water, and water-water. It is evident that with increasing water content, the total # of H-bonds, # of PVA-water H-bonds, and # of water-water H-bonds gradually increase, whereas the # of the PVA-PVA H-bonds decreases (see Figure 3.9c). Interestingly, the # of water-water H-bonds reaches the same level of that of PVA-water at a water content of $\sim 10.5\text{ wt}\%$, and exceeds that of the latter with further increased water content. Such trends in the # of various H-bonds are also well evidenced by the MD simulation (see Figure 3.9d).

Based on the IR and MD simulation, we propose the HB interactions of the PVA as a function of water content (see Figure 3.10). Specifically, at a water content less than $2.0\text{ wt}\%$, the H-bonds between PVA chains (i) are dominant and individual water molecules are uniformly bounded with PVA. When the water content is in the range of $2.0\sim 5.0\text{ wt}\%$, the H-bonds of PVA-water (ii) gradually increases although the i-type H-bonds still dominate, and meanwhile, the water-water H-bonds (iii) begin to appear. As the water content increases up to $10\text{ wt}\%$, the water-water H-bonds nearly approach those of PVA-water, leading to the

extensive formation of water clusters. With further increased water content or degree of hydration to ~20 wt%, the PVA film gradually transits to a plasticine-like state (see Figure AS13).

Above IR results strongly reveal that upon the addition of water, the H-bonds of PVA-water gradually replaces those of PVA-PVA, which can disrupt the intermolecular HB between PVA chains. Meanwhile, the # of water-water H-bonds can outnumber that of PVA-water, giving rise to the formation of water clusters once the water content reaches a critical value, here ~10 wt% (Bermejo & Ugarte, 2008). Moreover, the MD simulation results show what small water clusters start to form at a water content of only 5 wt%. In addition, Hodge *et al.* has previously shown that ~30 wt% is the critical water content for reaching the H-bond saturation between PVA and water. At such a water content, the PVA begins to behave in a solution-like manner but all the water molecules are still strongly bounded to the O-H of PVA, namely the nonfreezing water (Briscoe et al., 2000; R. M. Hodge et al., 1996). Therefore, the addition of water can disrupt and even destroy the strong HB between PVA chains by replacing such interactions. As a result of the disrupted intermolecular HB, the mechanical strength and modulus of PVA display a gradual decline trend with increasing water content by the plasticization effect.

In addition, such plasticization effect of water is also responsible for the reduced T_g of PVA. In addition to the FFV, the T_g of PVA is also relevant to its interchain distance. Therefore, the radial distribution function (RDF) $g_{A-B}(r)$ between the carbon atoms of two adjacent PVA chains is calculated to further investigate the effect of water content on the interchain distance of PVA. This gives the probability density of backbone carbon atoms at a distance r , which can be calculated by the following equation 3.13. It presents the atom density of type B averaged over all structure around A. N_A , N_B and N_{AB} correspond to the atom number of type A and B and their common part (C. Wu, 2010).

$$g_{A-B}(r) = \frac{V \left\langle \sum_{i \neq j} \delta(r - |r_{Ai} - r_{Bj}|) \right\rangle}{N_A N_B - N_{AB}} 4\pi r^2 dr \quad (3.13)$$

The RDFs of the backbone carbon of PVA, $g_{C-C}(r)$, and the (PVA)O-H---O(H₂O), $g_{O-H}(r)$, at various water content are respectively shown in Figure 3.11a and 3.11b. The interchain distance, r_{C-C} , of PVA shows a steady increase from 5.55 Å for PVA to 5.63 Å for PVA-10 until the water content reaches 10 wt%, and then it levels off as the water content increases to 30 wt% (Tasaki, 1996). The slight increase of 0.08 Å in r_{C-C} is mainly because of the strong HB interactions between PVA and water, and the small size of water molecules. Assuming that the diameter (d) of free volume cavities calculated by the PALS measurements is approximately equal to the interchain distance of PVA, it is interestingly found that the d value of the cavities is about 4.80 Å, which is very close to the simulated value (~5.60 Å). Moreover, when the water content is relatively high, herein ~14.5 wt%, the experimental d value increases to the simulated 5.60 Å, which strongly indicates the reliability of MD simulations (see Figure AS14). In addition, the $g_{O-H}(r)$ curves exhibits that the distance between PVA and water nearly maintain a constant because the length of (PVA)O-H---O(water) H-bond is about 1.69-1.72 Å (Tasaki, 1996), which is slightly shorter than the length of two O-H bonds (~0.96 Å, see Figure AS15). Figure 3.11c illustrates the presence of water molecules in the PVA bulk. Despite strong HB between water and PVA, the inclusion of water molecules still slightly increases the interchain distance (d) of PVA, thus leading more free space for the movement of PVA, especially when the water content is above 5.0 wt%.

On the basis of above findings, it is reasonable to conclude that the presence of water not only disrupts the HB interactions of the PVA bulk by reducing the number of PVA-PVA H-bonds, but also increases the interchain distance by forming water clusters. In addition to affecting the crystallinity of PVA, these two factors also lead to a plasticization effect at relatively low water content, and a

lubricating effect at high water content. The combination of the plasticization effect and the lubricating effect gives rise to reduced mechanical strength and stiffness but increased plasticity and toughness of the PVA bulk on the macroscopic scale, and increased relaxation and mobility of PVA chains on the microscopic scale. Therefore, water molecules govern the mechanical properties of PVA by disrupting the intermolecular HB interactions and promoting the chain movement of PVA.

3.4 Conclusions

In summary, we have systematically investigated the impact of water content on the mechanical properties, glass transition, free volume and intermolecular HB interactions of PVA by the combination of experimental and MD simulations. Both the mechanical strength and elastic modulus of PVA gradually decrease with increasing water content, whereas the ductility and toughness first increase and then reduce. For instance, the presence of only 1.8 wt% of water declines the tensile strength by ~32% but increases the ductility of PVA by ~250%. Besides, the increase in water content notably reduces the glass transition temperature and promotes the relaxation and mobility of PVA chains. The presence of water can disrupt the HB interactions of the PVA bulk by replacing PVA-PVA H-bonds with PVA-water H-bonds, thus weakening the intermolecular HB interactions of PVA, decreasing the degree of crystallinity, and leading to the plasticization effect. Moreover, at relatively high water content (>5.0 wt%), water clusters begin to form and result in a lubricating effect on the PVA chains. These two factors work together to cause reduced intermolecular interactions and increased chain mobility, thus making PVA show reduced mechanical strength and stiffness but increased plasticity and toughness. This work sheds light on how water determines the mechanical performances of the PVA, and gains an insightful understanding on the correlation between macroscopic performances, chain relaxation and

intermolecular interactions of polymers containing small molecules.

CHAPTER 4: INSIGHTS INTO THE HYDROGEN-BOND CROSS-LINKING EFFECTS OF SMALL MULTIAMINE MOLECULES ON PHYSICAL AND MECHANICAL PROPERTIES OF POLY(VINYL ALCOHOL) BY MOLECULAR DYNAMICS SIMULATIONS

This is from the publication resulted from my PhD:

L. Li, X. Xu, P. Song, Q. Cao, X. Qiao, Z. Xu, Y. Yang, C. Zuo, H. Wang, Insights into the hydrogen-bond cross-linking effects of small multiamine molecules on physical and mechanical properties of poly(vinyl alcohol) by molecular dynamics simulations. *Modelling and Simulation in Materials Science and Engineering*, 2021, 29, 035012 .

4.1 Introduction

Poly (vinyl alcohol) (PVA) is one of the most common biodegradable polymeric materials, which is widely used in the electronic fields (Howard et al., 2010; Kleinen & Richtering, 2011a; Lyon, Meng, Singh, Sorrell, & John, 2009; Monti, Fu, Iliopoulos, & Cloitre, 2008; Raheem, Roy, & Prasad, 2016; Städler et al., 2009; Zelikin, Price, & Stadler, 2010), tissue engineering (Anseth et al., 2002) and drug delivery (Chiessi, Cavalieri, et al., 2007). Recently, mechanically and thermal enhanced PVA films by adding a small amount of nanofillers were prepared experimentally (Basta & Lotfy, 2019; Gunge, Koppad, Nagamadhu,

Kivade, & Murthy, 2019; Morimune et al., 2011; Potts et al., 2011; Voronova, Surov, Guseinov, & Zakharov, 2016; J. Wang, Cheng, Lin, Chen, & Jiang, 2013). However, this strategy leads to a trade-off between strength and toughness due to mutually exclusive governing mechanisms. Therefore, it has been a long-standing challenge to design strong and tough PVA materials (Alexy, Kachova, Krasiak, Bakos, & Simkova, 2002; Ding, Chen, Wang, & Wang, 2009).

The natural silks possess exceptional mechanical properties with combination of high strength and great extensibility compared to most of man-made materials. The previous works reveal that the β -sheet nanocrystals, assembled by well-organized hydrogen bonds (H-bonds), play a key role in determining such mechanical properties. It demonstrates that β -sheet nanocrystals reinforce amorphous domains, leading to high strength and great toughness through cooperative HB (Brockwell et al., 2003; Buehler & Yung, 2009; Eom, Li, Makarov, & Rodin, 2003; E. H. Lee, Gao, Pinotsis, Wilmanns, & Schulten, 2006; Lefèvre, Rousseau, & Pérolet, 2007; Rief & M., 1997; SulKowska & Cieplak, 2007). The ultimate strength and toughness of spider silks are even comparable to steel (Du et al., 2006; S. M. Lee et al., 2009). This encouraging finding has stimulated the creation of strong and tough PVA materials by the addition of specific small molecules to construct the HB.

Some molecules capable of forming H-bonds, such as glycerol (Tudorachi, Cascaval, Rusu, & Pruteanu, 2000), multiamines (Song et al., 2015a), urea/caprolactam, benzene/cyclohexane and tannic acid (Guan et al., 2016), have been introduced to create high-performance PVA composites. The combination of glycerol and urea can enhance the thermal stability of PVA, but decrease tensile strength with increasing the mixture concentration (Xiang, Yao, Jia, & Dong, 2009). The interaction mechanism of PVA with urea and caprolactam indicates that the elastic modulus of PVA decreases with increasing the mixture concentration in despite of the existence of abundant H-bonds in the composite system (X. Zhao,

Zhang, Chen, & Lu, 2011). Recently, Wu et al. (W. Wu, Tian, & Xiang, 2012) reported that the HB interaction occurs between PVA and polyol plasticizer, but the glass transition temperature decreases with increasing the plasticizer concentration. In contrast, our previous work has demonstrated significantly increased glass transition temperatures, enhanced thermal stability and mechanical properties of PVA for low concentration of multiamines, such as 4N-2456 (P. Song & H. Wang, 2020; Song et al., 2013; Song et al., 2015a, 2015b). In addition, both the thermal degradation temperature and mechanical properties are found to obey a linear relationship with the H-bond number or cross-linking density (Song et al., 2015a, 2015b). Despite the promising experimental achievements, it remains unclear how the H-bond cross-linking effect controls the glass transition, chain dynamics and mechanical properties of the PVA/4N-2456 composites on molecular scale.

Molecular dynamics (MD) simulations provide a powerful tool to understand the experiment results and resolve controversy for different experimental conclusions. The present work aims to gain an insight into the HB interactions and chain dynamics of PVA/4N-2456 supramolecular complexes on molecular level using MD simulations. Our simulation results show that the interactions of multiple H-bonds between the PVA and 4N-2456 molecules affect the structural and dynamics properties of composites, such as the free volume, chain mobility, glass transition temperature and elastic modulus. It also predicts enhanced mechanical properties (such as the Young's modulus) in a range of low 4N-2456 concentration, which is consistent with the experiments (Song et al., 2015a) except for larger value due to extremely higher strain ratio used in the MD simulations. Further, it offers an insightful understanding for the formation mechanism of the PVA/4N-2456 composites and the relevance between the molecular interactions and various properties.

4.2 Simulation Methods

4.2.1 Preparation of initial model system

The structures of the 4N-2456 molecules and the PVA chains with the repeat unit of $n=99$ was generated. We first performed the energy minimization of the system through the conjugate gradient algorithm to obtain appropriate input configurations for the following simulations. Then, model systems with different 4N-2456 concentrations ($\phi= 0$ wt%, 0.5 wt%, 1.0 wt%, 2.0 wt%, 5.0 wt%, 10 wt%, 15 wt%, and 20 wt%) were constructed. Each system contains ten PVA chains. The initial value of density for different configurations was taken as 1.0 g/cm^3 . The periodic boundary conditions were applied along three coordinate directions. A set of ten configurations for each case were generated. Figure. 4.1 shows the molecular structures of PVA and 4N-2456. And the molecular system for all simulations of PVA/4N-2456 concentrations are list in Table 4.1.

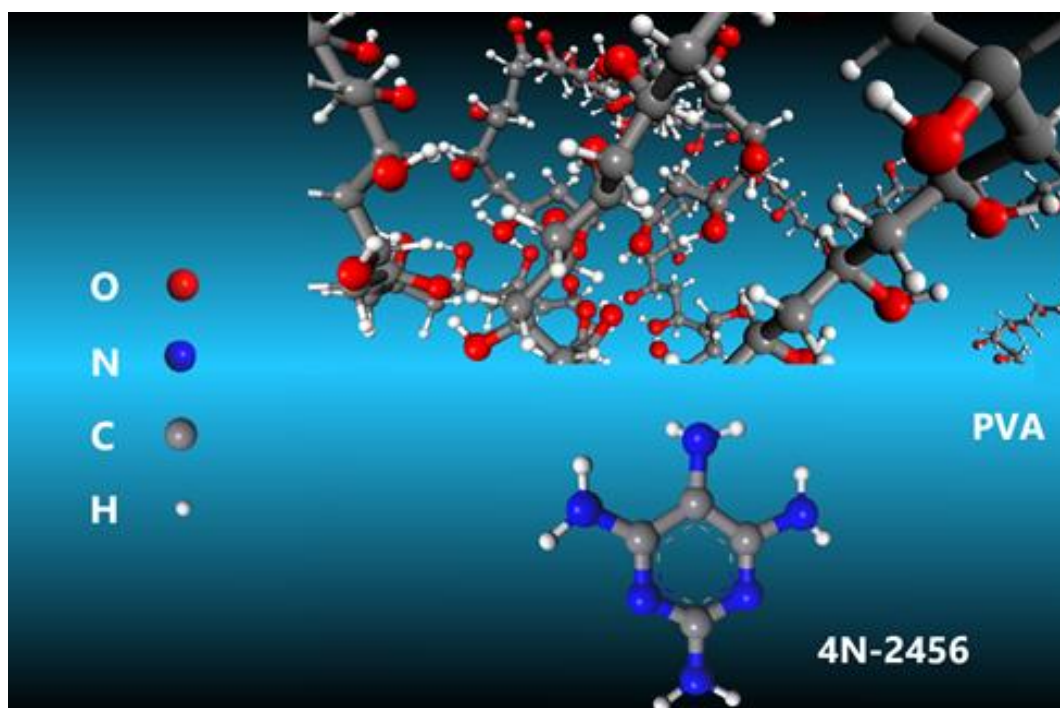


Figure 4.1 Molecular models for the simulations of PVA/4N-2456 composites.

Table 4.1 The model systems with different 4N-2456 concentrations.

Φ (wt%)	No. of 4N-2456	cell size(Å)	equilibrium density (g/cm ³)
0	0	39.72106	1.191
0.5	2	39.477835	1.192
1.0	3	39.544049	1.183
2.0	6	39.714443	1.183
5.0	17	40.063634	1.193
10	35	40.697843	1.194
15	55	41.315509	1.207
20	78	42.096935	1.217

4.2.2 Molecular dynamics simulations

In classical MD simulations, the positions and velocities of particles in the model system evolve as a function of time. The equations of motion are integrated using the Verlet velocity algorithm with a time step of 1 fs. The formalism of interaction potential between particles is an important ingredient in the MD simulations. Here, the high-quality COMPASS (Condensed-phase Optimized Molecular Potential for Atomistic Simulation Studies) force field is employed for modeling the molecular interactions, which can successfully predicate the structural and dynamics properties for many polymer materials (Shen et al., 2018; C. Wu & Xu, 2007).

The initial velocities of the particles were generated by temperature-dependent Gaussian distribution. The particle mesh Ewald (PME) method with a nonbonded cutoff of 1.25 nm was used to calculate long-range electrostatic interactions. To avoid being trapped in the local energy minimum conformations, one cycle anneal dynamics procedure was conducted. During the process, we used NPT (constant particle number, pressure and temperature) ensemble. To regulate the system temperature, the system is coupled to the Andersen thermostat

(Andersen & Hans, 1980). The pressure is controlled using the Berendsen algorithm with relaxation time of 1ps (Berendsen, Postma, van Gunsteren, DiNola, & Haak, 1984). In annealing cycles, the initial temperature was set to 300K and the highest temperature 500K. Ten ramps per cycle were carried out. The simulation for each ramp was 5×10^4 time steps. Then, the NPT simulations run for 10ns to obtain the equilibrium density at 300K. The density of the pure PVA measured experimentally is about 1.26 g/cm^3 (Davidson; Xiang et al., 2009). The equilibrium density of the pure PVA is 1.191 g/cm^3 at 300 K, within the error range of about 3-5 wt% (Bermejo & Ugarte, 2008; H. Sun, 1998). Finally, we performed simulations for 20 ns and sampled the production data to analyze the trajectories of simulations and calculate the related system properties.

4.2.3 Calculation of properties

The glass transition temperature T_g is one of critical thermal properties of polymer materials because it demonstrates polymer transition from a rigid state to a more flexible state. It can be calculated through measuring free volume, mean square displacement (MSD), network topology density or molecular energy components (Bermejo & Ugarte, 2010).

The H-bonds are formed between the hydrogen atom and two negatively charged atoms through electrostatic interactions. They are denoted as H—D•••A, where D and A are donor and acceptor, respectively. Generally, the strength of the H-bonds is stronger than the van der Waals interaction but weaker than the covalent bond. Therefore, the H-bonds play a critical role in determining the properties of materials. In our simulations, the H-bonds are geometrically defined according to the criterion in Ref (Morimune et al., 2011; Yoshinori Tamai, Hideki Tanaka, & Koichiro Nakanishi, 1996a). The D—A distance is lower than 0.35 nm and the H—D•••A angle is less than 30° . The distance value corresponds to the first minimum of radial distribution functions between D and A. The structure of

H-bonds in the PVA/4N-2456 composites is shown in Figure 4.1.

The elastic moduli of the composite materials can be calculated by static (Theodorou & Suter, 1986) or dynamic methods (D. Brown & J. H. Clarke, 1991). Here, we use the dynamic method to measure the mechanical properties of the PVA/4N-2456 composites through analyzing stress-strain curves. In the range of elastic deformation, the strain tensor ε . They are symmetric tensors: $\varepsilon_{LM} = \varepsilon_{ML}$, $\sigma_{LM} = \sigma_{ML}$. The relationship between strain and stress is expressed according to Hook's law in the range of elastic deformation, $\sigma_{LM} = C_{LMNL}\varepsilon_{NK}$. By introducing the equation 3.7, the Young's modulus (E), Poisson ratio (γ), shear modulus (G) can be calculated as following:

$$E_Y = \mu \frac{3\lambda + 2\mu}{\lambda + \mu} \quad (4.1a)$$

$$\gamma = \frac{\lambda}{2(\lambda + \mu)} \quad (4.1b)$$

$$G = \mu \quad (4.1c)$$

$$K = \lambda + \frac{2}{3}\mu \quad (4.1d)$$

Based on the analysis of strain-stress curves, we can calculate the Lamé constants and obtain the elastic constant further.

4.3 Results and Discussion

4.3.1 H-bond interactions

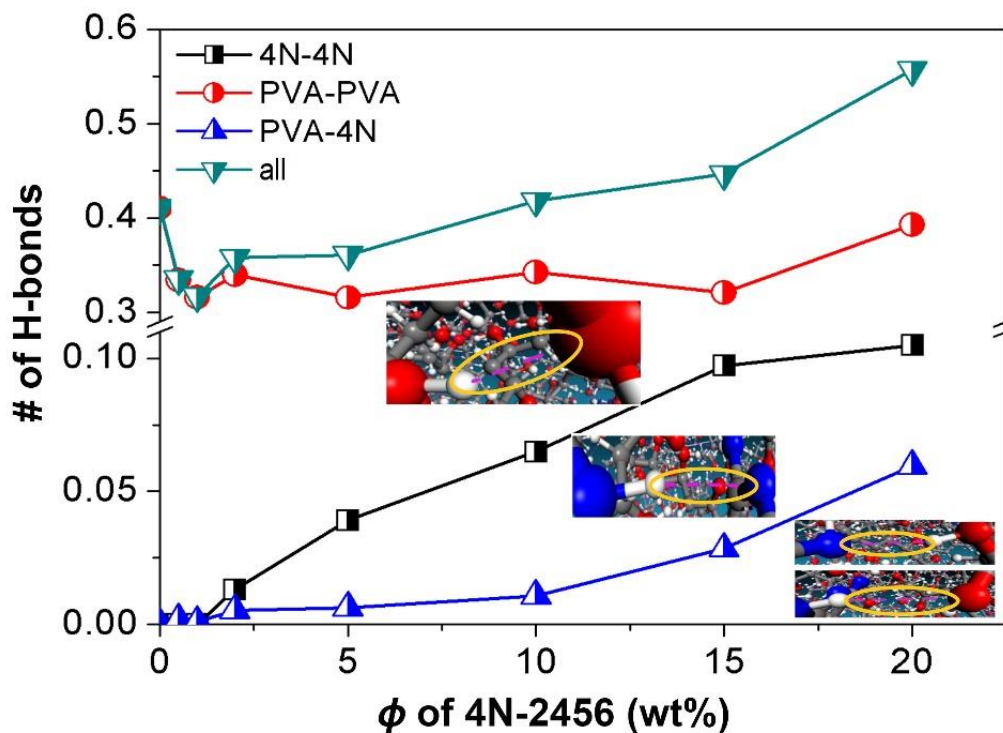


Figure 4.2 Number of H-bonds as a function of the 4N-2456 concentration at 300 K.

First, we present the number of H-bonds between different components in the composite system at 300 K as a function of the 4N-2456 concentration ϕ in Figure 4.2. The number of H-bonds is normalized by the number of PVA monomers except for the number of H-bonds between 4N-2456 molecules which is normalized by the number of 4N-2456 molecules. At low 4N-2456 concentration, the addition of the 4N-2456 molecules leads to reduced number of H-bonds between the PVA chains. This is because the 4N-2456 molecules damage the HB network of the PVA chains near the 4N-2456 molecules, thus leading to reduction of the number of H-bonds. The number of H-bonds increases remarkably with further increasing the 4N-2456 concentration except for that between the PVA chains, because the added 4N-2456 molecules inhibit the formation of intermolecular H-bonds in the bulk PVA itself. The number of H-bonds between

PVA and 4N-2456 increases gradually. It means that the interactions between PVA and 4N-2456 is enhanced. There is a larger number of H-bonds between the 4N-2456 molecules compared to that between PVA and 4N-2456 when the 4N-2456 concentration exceeds 1wt%. This is related to the formation of cluster structures of the 4N-2456 molecules in the composite.

4.3.2 *Free volume*

The free volume plays an important role in explaining the transport behavior of the composite of the PVA chains and the 4N-2456 molecules. Detailed MD simulations can detect accurate free volume voids and provide a qualitative tool to study the structure of the composite (S. Lee & Mattice, 1999). The atoms in the composite system are represented as hard spheres. The molecular surface (or Connolly surface) is measured through rolling over the van der Waals (vdW) surface using the probe molecule with the radius R_p as shown in Figure 4.3. Then, we define the free volume as the volume outside of molecular surface area. The fraction of free volume (FFV) obtained by the method depends strongly on R_p , but the calculated results show the same tendency for different R_p (Pan et al., 2007). The vdW scale factor is taken as 1.0 in all simulations. It should be noted that the free volume does not include the blind area that the probe molecule cannot touch.

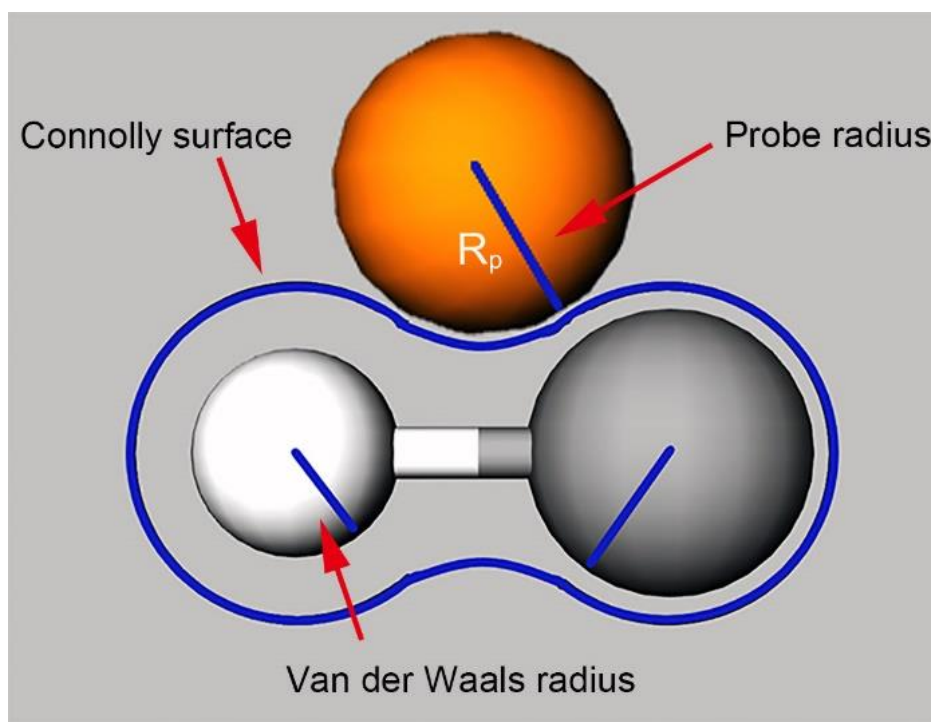


Figure 4.3 Schematic of the method of drawing a Connolly surface with radius R_p . The atoms are represented as hard spheres with vdW radius.

The FFV (Wei et al., 2017; Xie et al., 2018) can be used to predict the interactions between molecules. It is defined as $FFV = v_f / (v_o + v_f) \times 100\%$, where v_f and v_o are the free volume and the occupied volume, respectively.

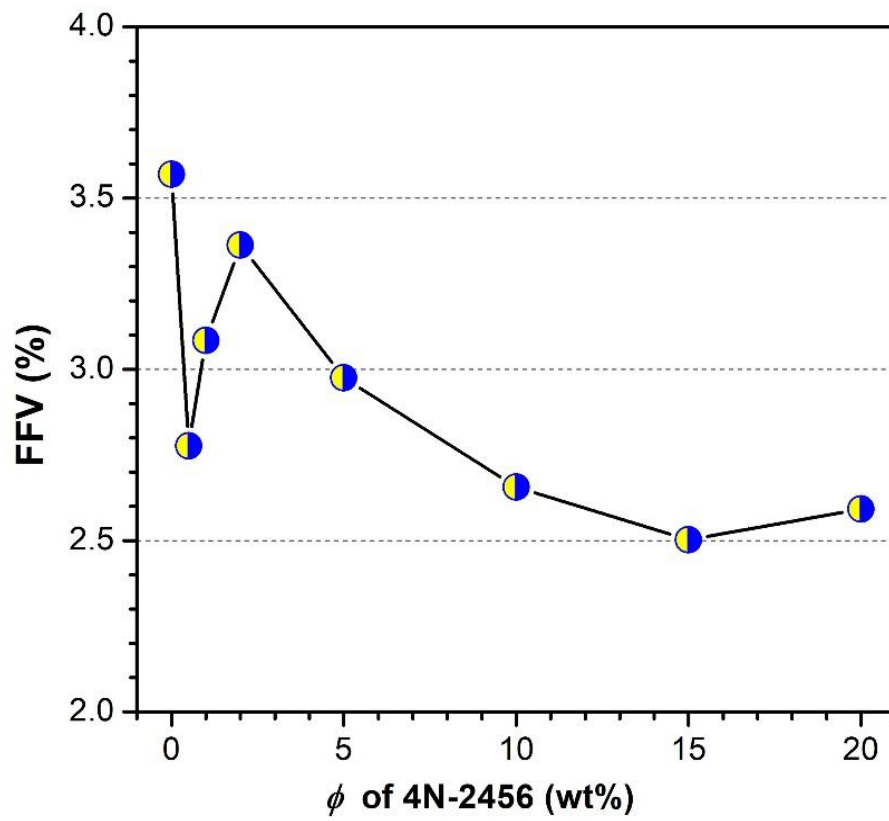


Figure 4.4 Fraction of free volume of the composite system as a function of the 4N-2456 concentration (ϕ).

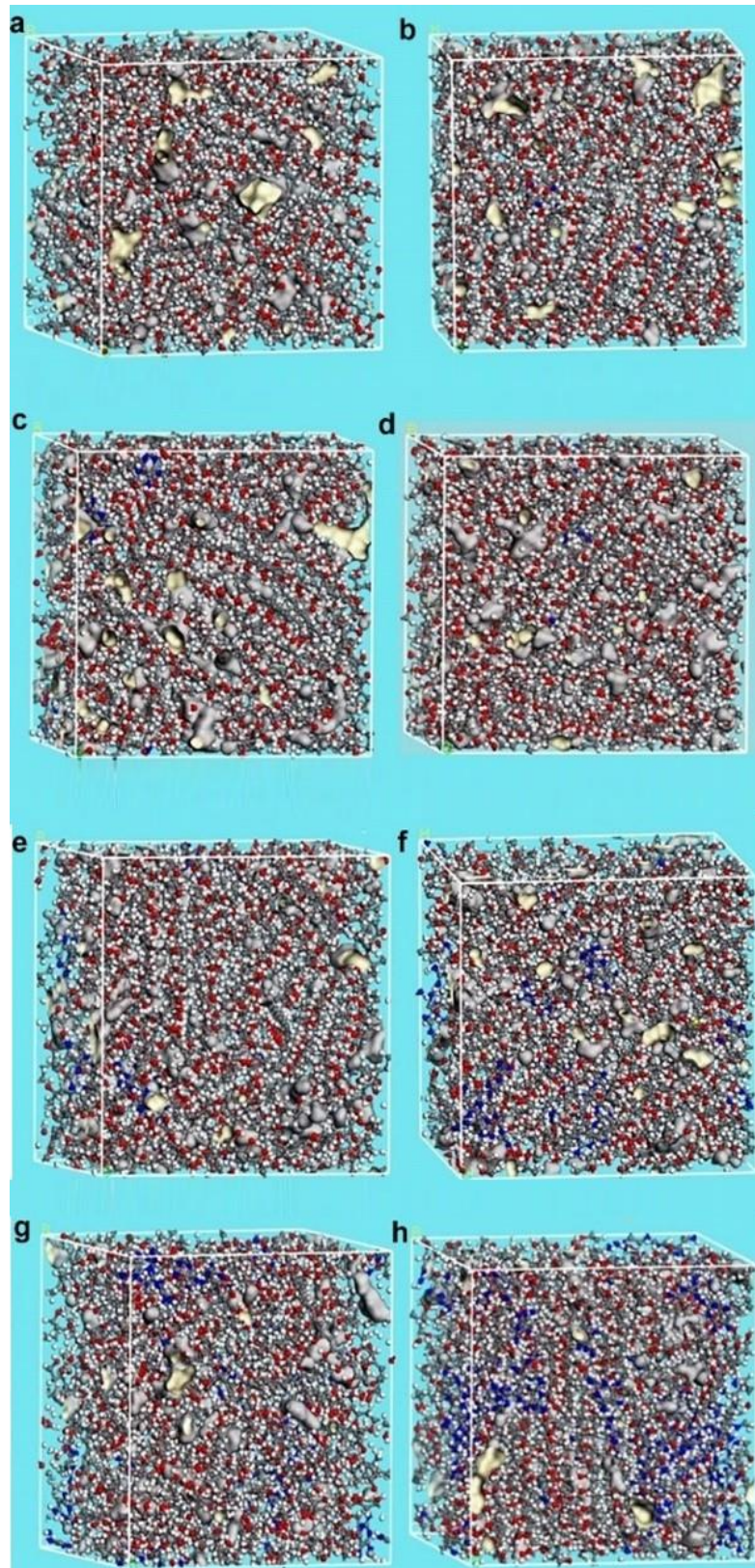


Figure 4.5 Simulation snapshots of the composite system for various 4N-2456 concentration
a) pure PVA, b) 0.5 wt%, c) 1 wt%, d) 2 wt%, e) 5 wt%, f) 10 wt%, g) 15 wt%, h) 20 wt%.

The bubbles represent the free volume.

Figure 4.4 shows the FFV of the composite system as a function of the 4N-2456 concentration. To present the FFV in a visual form, we also give the corresponding simulation snapshots in Figure 4.5. The relationship between the FFV and the 4N-2456 concentration is complicated due to the formation of cluster structures and the interactions between the PVA chains and the 4N-2456 molecules. For pure PVA materials, the FFV is about 3.6 wt%, which is significantly higher compared to the cases in the presence of 4N-2456 molecules. When a low amount of 4N-2456 molecules are added into the PVA system, the FFV decreases owing to the entrance of small molecules. However, the FFV increases until 3.4% at $\phi_N=2$ wt% with the 4N-2456 concentration. The FFV is related to molecular interactions. Stronger molecular interactions mean more compact structure. Initially, the increase of the 4N-2456 concentration leads to a decrease of the number of H-bonds. It indicates that the molecular interactions are weakened. Therefore, the composites become slightly loose, corresponding to higher FFV. With further increasing the 4N-2456 concentration, the H-bond interaction between the 4N-2456 molecules themselves becomes more prominent than that between 4N-2456 and PVA. This causes the 4N-2456 molecules to form larger clusters which occupy the free volume. In addition, the 4N-2456 clusters also bridge the PVA chains through the H-bonds interactions, which partly contributes to the decrease of the free volume to some extent at high 4N-2456 concentrations.

4.3.3 *Mobility of PVA chains*

Previous works reveal that the mobility of the polymer chains can be restricted due to the interactions between added molecules and polymer chains (Fragiadakis, Pissis, & Bokobza, 2005), and the motion of atoms in voids of free volumes is also controlled by the movement of chains in polymer network (Nagel et al., 2000). The present simulations show that the change of the 4N-2456 concentration can influence the free volume of the composite and the chain-chain

interactions, which is important in determining the chain mobility.

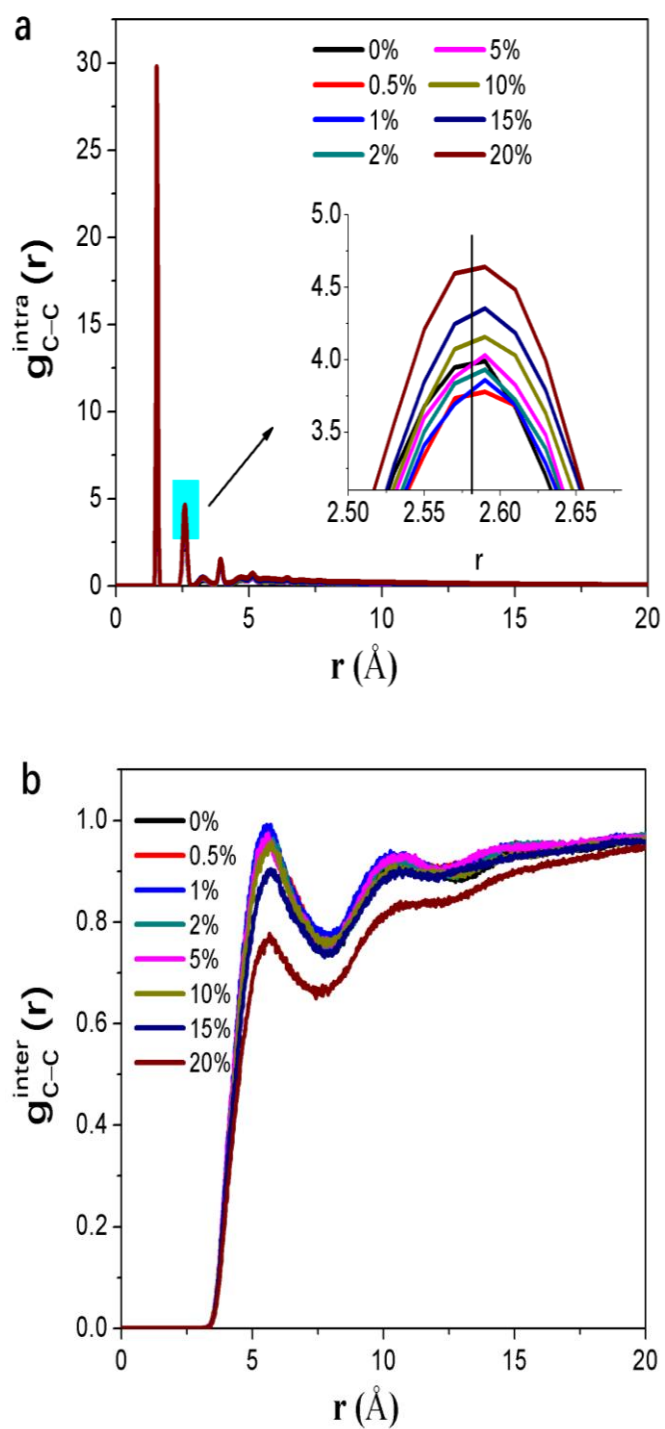


Figure 4.6 Radial distribution functions of the PVA backbone carbons at various 4N-2456 concentrations for (a) intramolecular $g_{C-C}^{intra}(r)$ and (b) intermolecular $g_{C-C}^{inter}(r)$.

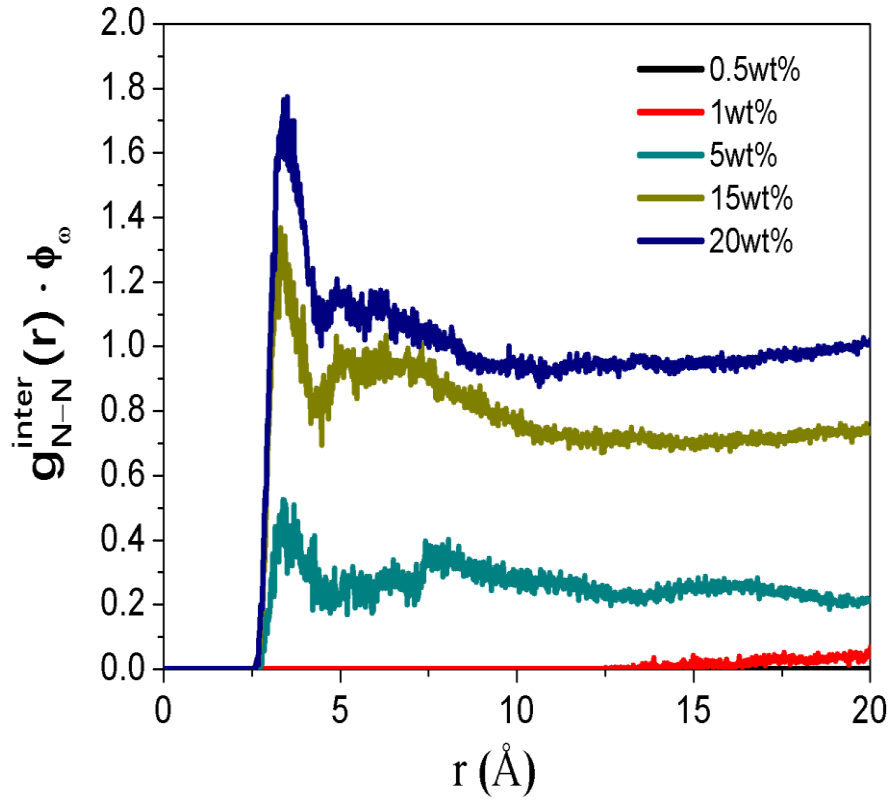


Figure 4.7 $g_{N-N}^{inter}(r)\phi_{\omega}$ as a function of the radial distance. $g_{N-N}^{inter}(r)$ is radial distribution function for the N atoms from 4N-2456 molecules. $\phi_{\omega} = \phi / \phi_m$ is the ratio of the 4N-2456 concentrations, and $\phi_m = 20wt\%$ is the maximum 4N-2456 concentration in the present simulations.

We describe the radial distribution function (RDF) before analysis of the chain mobility. The RDF of the carbon atoms between the PVA chains is related to the effect of the 4N-2456 concentration on the local structure of the composites. It gives the probability density of the backbone carbon atoms at a distance of r . The RDF is calculated by equation 3.13. The RDF of the backbone carbons at different 4N-2456 concentrations are shown in Figure 4.6. The value of the RDF is zero at a small distance because of the excluded volume effect, but it approaches to a steady value at a larger distance where the spatial correlation impact disappears. The results of the intramolecular RDF, $g_{C-C}^{intra}(r)$, indicate that the first peak

increases with the 4N-2456 concentration, corresponding to steadily enhanced intramolecular interactions with increasing the 4N-2456 concentration (> 2.0 wt%). In Figure 6a, the first peak locates at about $r = 1.53\text{\AA}$, corresponding to the distance of the C-C bond. The second peak indicates strength of non-bonded interactions. The results show that the interactions of intra-molecules are enhanced with the 4N-2456 concentration. In Figure 4.6b, the first peak is observed at about 5.0\AA belonging to the carbon atoms of the intermolecular case. It should be noted that the distance of the first peak increases from 5.5\AA to 5.8\AA when the 4N-2456 concentration is higher than 5.0 wt%. The high 4N-2456 concentration influences the distance between the PVA chains due to the H-bond interactions between the PVA and 4N-2456 molecules. The RDF of the N atoms between 4N-2456 molecules is also calculated (see Figure 4.7). At low concentrations, the correlation between 4N-2456 molecules disappears. As the 4N-2456 concentration increases, the molecular correlation is enhanced. The apparent peak indicates the formation of 4N-2456 clusters.

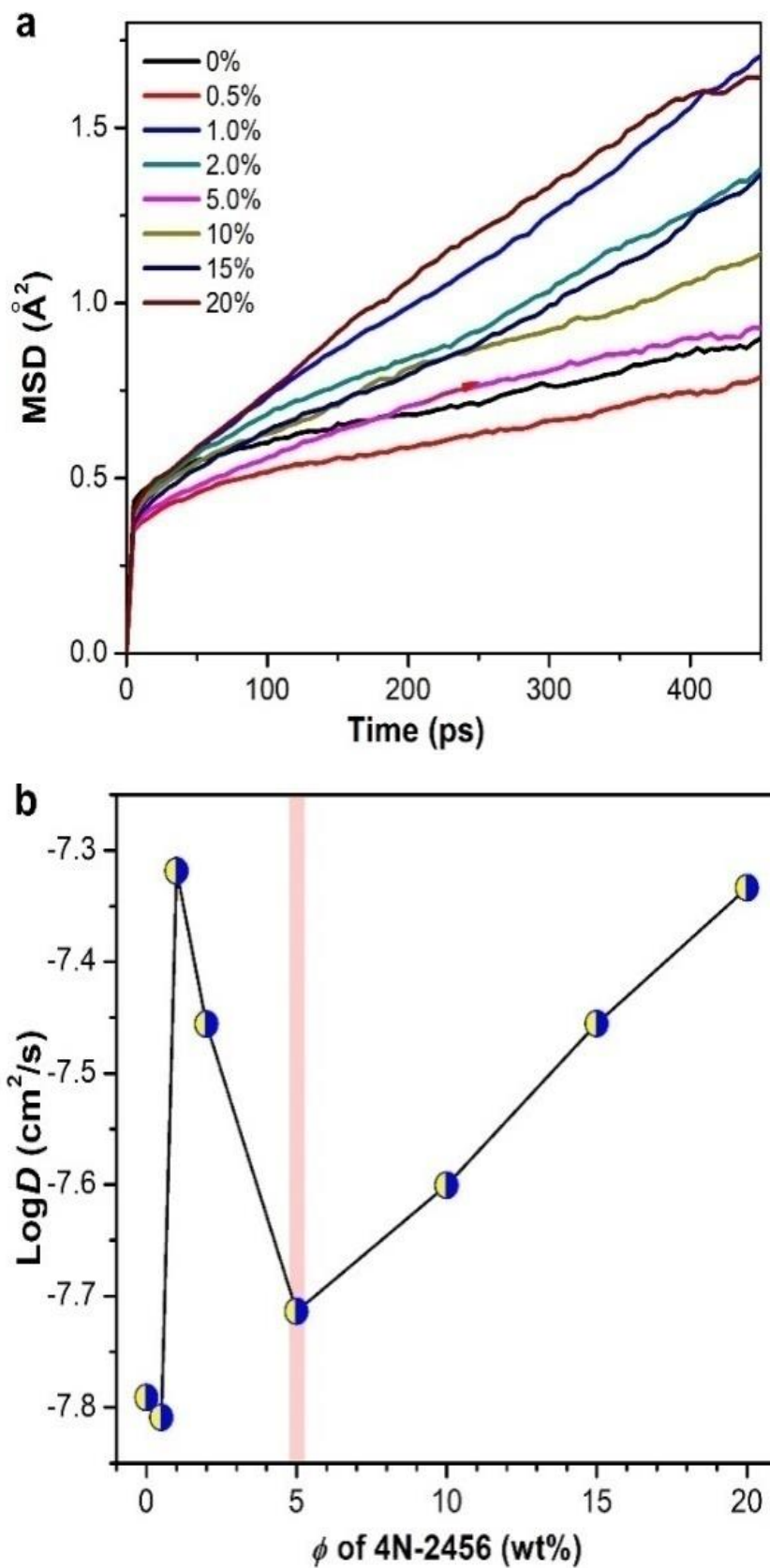


Figure 4.8 Mobility of the PVA chains at different 4N-2456 concentrations: (a) mean square displacement (MSD) and (b) diffusion coefficient (D).

The diffusion coefficient D of the PVA chains is calculated through the following formula

$$D = \frac{1}{6} \lim_{t \rightarrow \infty} \frac{d}{dt} \sum_{i=1}^N \langle |\mathbf{r}_i(t) - \mathbf{r}_i(0)|^2 \rangle \quad (4.2)$$

where $\mathbf{r}_i(t)$ is the position vector of atom i at time t . $\sum_{i=1}^N \langle |\mathbf{r}_i(t) - \mathbf{r}_i(0)|^2 \rangle$ denotes the mean square displacement (MSD) with ensemble average. The MSD profiles of the PVA chains at different 4N-2456 concentrations in a short time range are shown in Figure 4.8a. The diffusion of the PVA chains exhibits a significant dependence on the 4N-2456 concentration. To illustrate the relationship between the PVA diffusion and the 4N-2456 concentration, the diffusion coefficient (D) of the PVA chains as a function of the concentration is plotted in Figure 4.8b. D is smaller for the pure PVA system and at low concentrations. This is because strong interaction between the PVA monomers, in particular H-bonds, constrains the PVA mobility. The diffusion is boosted when the 4N-2456 concentration increases to 1.0%. The increase of diffusion coefficient of the PVA chains is due to that the addition of the 4N-2456 molecules weakens the interactions between the PVA chains. However, the diffusion ability of the PVA chains decreases as the 4N-2456 concentration increases from 1.0 wt% to 5.0 wt%. This means that in the concentration range ($1\text{wt}\% < \phi < 5\text{wt}\%$), further increase of the 4N-2456 concentration restricts the motion of the PVA chains because of enhanced PVA/4N-2456 interactions. At higher concentrations ($\phi_N > 5.0 \text{ wt}\%$), the interactions between the 4N-2456 molecules themselves become strong, leading to the formation of 4N-2456 molecule clusters which can lubricate the PVA chains.

4.3.4 Glass transition temperature

The mobility of polymer chains is strongly relevant to the glass temperature T_g , which reflects the phase transition from the glassy state to the rubbery state or

vice versa. The glass temperature is a critical feature of polymer materials because it determines the temperature window of the practical applications of polymers. To obtain the glass temperature, the PVA composite system is cooled from 600 K to 200 K with an interval of 15 K. The T_g can be determined from the turning point of the density versus temperature as shown in Figure 4.9. The previous works indicate that T_g determined by the change in different properties as a function of temperature gives similar results. To study the glass transition in affordable computational cost, the simulations are required to run under much higher cooling ratio than that of real experiment. As a result, it produces a shift in T_g towards higher values, 1-3 K per decade (Bermejo & Ugarte, 2010). This effect has already been observed by other MD simulation works and it is simply due to the logarithmic cooling rate dependence.

The glass temperature is significantly affected by the 4N-2456 concentration as shown in Figure 4.9. The detailed T_g values are listed in Table 4.2. On the whole, the T_g exhibits a steady increase, then followed by a gradual decrease as the 4N-2456 concentration increases. The glass temperature for the pure PVA is 67°C determined by the DSC (L. Li et al., 2021), which approaches to the simulated value 70.8°C.

In particular, at low 4N-2456 concentrations the T_g increases with the concentration until about 5.0 wt%. The large T_g value reveals that higher thermal energy is required to activate the PVA segments. Therefore, the increase of the 4N-2456 concentration (<5.0 wt%) implies enhanced interaction energy and strong H-bond interactions between the PVA chains and the 4N-2456 molecules. This restricts the movement of the PVA segments. As the 4N-2456 concentration increases further, a decreasing tendency of the T_g is observed. It indicates that the 4N-2456 molecules can promote the movement of the PVA chain segments owing to the lubricating effect of 4N-2456 molecule clusters as discussed above.

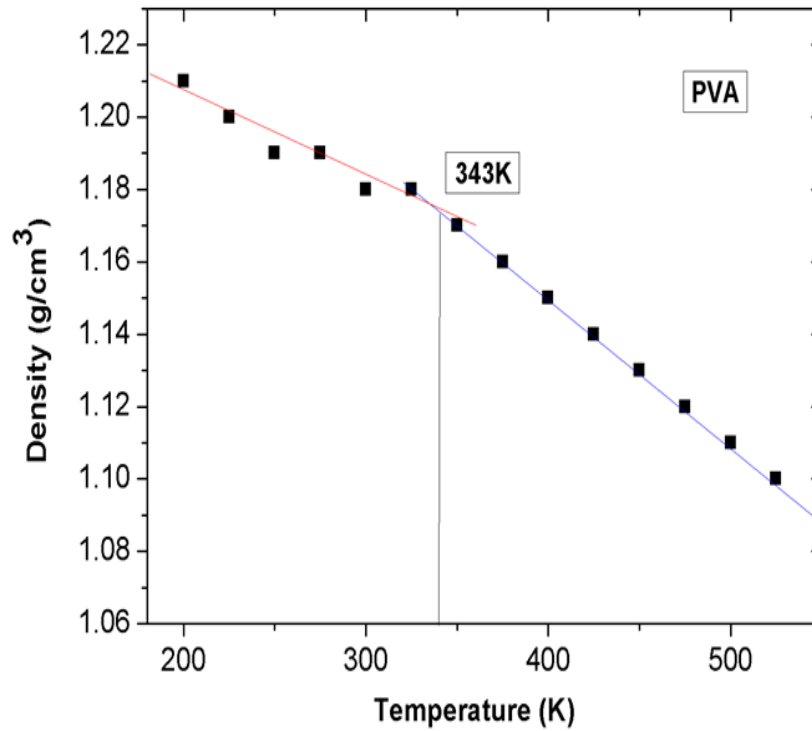


Figure 4.9 The density as a function of temperature for calculation of glass transition temperature T_g of the pure PVA

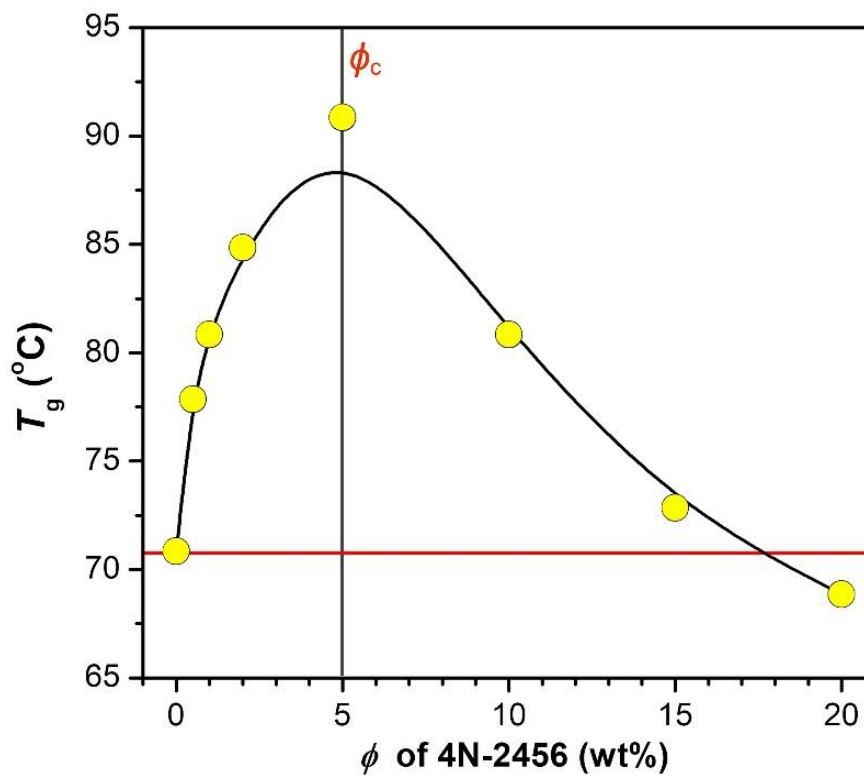


Figure 4.10 The glass transition temperature T_g of the composites as a function of the 4N-2456 concentration.

Table 4.2 Glass transition temperatures of the composite systems for various 4N-2456 concentrations.

4N-245(wt%)	0	0.5	1.0	2.0	5.0	10	15	20
T_g (°C)	70.8	77.9	80.8	84.9	90.8	80.9	72.8	68.9

4.3.5 Mechanical performances

Finally, we calculate the mechanical properties of the PVA/4N-2456 composites using the constant-strain approach. The results are summarized in Table 4.3. For each configuration, the maximum strain amplitude ± 0.003 which is in range of elastic strain, is applied. The mechanical properties of the composite systems are obtained at 300 K. The calculation shows that the Poisson's ratios are around 0.3 in good agreement with the values (0.2-0.4) of plastic materials (Ma et al., 2005). The simulated strain rate is $1 \times 10^9 \text{ s}^{-1}$. Generally, the Poisson's ratio is less affected by the strain rate (Odegard et al., 2014). It was found that the elastic moduli of the composites increase with the 4N-2456 concentration and reach the peak values at $\phi=5.0$ wt%. For example, the Young's modulus is 10.4 GPa for the pure PVA material. The value is higher compared to the measured elastic modulus 2.8-3.5GPa in experiment (Bermejo & Ugarte, 2010). To obtain the mechanical properties in affordable computational cost, the simulations are required to run under extremely higher strain ratio compared to the experiments. This generally leads to higher modulus. Then, the addition of the 4N-2456 molecules with $\phi=5.0$ wt% increases the modulus up to 13.1 GPa (Table 4.3). Experimentally, we also observed enhanced mechanical properties (such as the Young's modulus) in a range of low 4N-2456 concentration (Song et al., 2015a), except for larger value in the MD simulations. Interestingly, the peak of the modulus corresponds to the

lowest diffusion coefficient (Figure 4.8) and the highest glass temperature (Figure 4.10). This is because the H-bonds between the PVA chains and the 4N-2456 molecules cross-link molecular components in the composites significantly, which restricts the diffusion and mobility of the PVA chains. The present finding reveals that the H-bond cross-linking effect induced by the 4N-2456 molecules enhances the intermolecular interactions and improves the stiffness of the composites.

Table 4.3 Mechanical properties of the composite systems at various 4N-2456 concentrations.

4N-2456 concentration (wt%)	Bulk modulus (GPa)	Shear modulus (GPa)	Young's modulus (GPa)	Poisson Ratios
0	9.39	4.32	10.4	0.3185
0.5	9.76	4.76	11.4	0.3178
1	10.1	4.86	12.6	0.3278
2	11.1	5.02	12.6	0.3212
5	11.2	5.26	13.1	0.3143
10	10.6	5.03	12.0	0.3181
15	10.8	5.10	12.9	0.3036
20	10.3	5.02	12.6	0.3089

4.4 Conclusions

In this work, we investigate the effects of the 4N-2456 concentration on the free volume, chain mobility, glass transition, H-bond interactions and mechanical properties of the PVA composites by using MD simulations. Because of the strong intermolecular H-bonds, the free volume of the composites shows a nonlinear decrease in the range 0-20 wt% of the 4N-2456 concentration. It was found that the optimal concentration is about 5.0 wt% for many properties of the PVA/4N-2456 composites. At this concentration, the PVA chains show a relatively low mobility, the highest glass transition temperature and the highest elastic modulus.

In a range of the 4N-2456 concentration below 5.0 wt%, the addition of the 4N-2456 molecules can restrict the chain mobility and increase both the glass transition temperature and the elastic modulus due to enhanced H-bond cross-linking effect. In the concentration range above 5.0 wt%, some 4N-2456 molecules could form clusters, which promotes the chain mobility. As a result, glass transition temperature and elastic modulus decreased owing to lubrication effect of the 4N-2456 clusters as well as weakened H-bond interactions between the PVA chains. The work provides a molecular-level insight into how small 4N-2456 molecules affect the intermolecular interactions, chain dynamics and mechanical properties of the PVA matrix through the H-bonds.

CHAPTER 5: STRUCTURE, CHAIN DYNAMICS AND MECHANICAL PROPERTIES OF TRANSPARENT AND ANTIBACTERIAL POLY(VINYL ALCOHOL)/PHYTIC ACID COMPOSITE FILMS

This part has been submitted to :

L. Li, X. Xu, B. Wang, P. Song, Q. Cao, Y. Yang, Z. Xu, H. Wang, Structure, chain dynamics and mechanical properties of transparent and antibacterial poly(vinyl alcohol)/phytic acid composite films. *Composites Communications*, 2021, under review.

5.1 Introduction

The intractable micro- and nano-plastic issue has challenged and been damaging our living environment more than ever (Kane et al., 2020). This environmental crisis has significantly catalyzed the development of more sustainable and biodegradable polymers (plastics). Because of excellent biocompatibility, biodegradability, excellent mechanical properties, and good film-forming ability, polyvinyl alcohol (PVA) has gained growing interests for its extensive applications in pharmacy, automotive industry, packaging, fibers, and electronic industries (Bonderer et al., 2008; Cazon, Vazquez, & Velazquez, 2020; B. Huang et al., 2019; Wan et al., 2015). Recent interests particularly focus on improving mechanical and/or thermal stability properties of PVA to expand its practical applications in packaging and engineering fields. With the addition of external cross-linking reagents (W. Zhao et al., 2016), the resultant PVA films usually exhibit improved thermal stability and mechanical properties because the physical or chemical cross-linking can suppress the dehydration reaction and the

chain movement to some extent (Jihui Li, Li, Song, Niu, & Li, 2017; Y. Li & Yao, 2017; L. Yao et al., 2003). The cross-linkers for PVA can be either organic or inorganic compounds, such as dimethyl carbonate (Cui et al., 2020; Jihui Li, Li, Niu, Liu, & Wang, 2017; Park & Lee, 2018), cellulose nanocrystals (Yang et al., 2020), poly (acrylic acid) (W. Zhao et al., 2016), lignin (Kubo & Kadla, 2003), phosphoric acid (Prajapati, Roshan, & Gupta, 2010) and boric acid (Yin, Li, Liu, & Li, 2010).

Phytic acid (PA), a non-toxic biomacromolecule (Samotus & Schwimmer, 1962), has been widely employed as cross-linking reagent (Jihui Li, Li, Song, et al., 2017), antimicrobial agents (Gao et al., 2016; Q. Zhou, Zhao, Dang, Tang, & Zhang, 2019), and flame-retardant additive (Y. Zhou, Ding, Qian, & Ankey, 2015) as well as other property enhancer for polymers (Krishnamoorthy, Kim, & Kim, 2013; Masoomi & Morsali, 2012). In addition to potential applications in the areas of proton-conducting membranes (Jiang, Qiao, & Hong, 2012), and Li-ion batteries (H. Wu et al., 2013), the PA was also reported as a dopant to prepare conductive and flame-retardant polyaniline-deposited papers (Y. Zhou et al., 2015). Moreover, a recent study has revealed that PA has a good antibacterial ability to damage the cell morphology, thus affording new opportunities in the food industry (Q. Zhou et al., 2019). Given the multi-hydroxyl groups in molecules and antibacterial activities, PA molecules are expected to be used for the fabrication of antibacterial, mechanically robust and biodegradable PVA materials (Jihui Li, Li, Song, et al., 2017). In addition, it is essential to unveil how PA molecules affect the intermolecular HB, structure, chain dynamics and mechanical properties of the final PVA/PA composites both theoretically and experimentally.

Molecular dynamics (MD) simulations allow us to extract important information about intermolecular interactions, dynamics and mechanical properties as well as their correlations of PVA blends or composites at a molecular level (Jing Li et al., 2019; Ni et al., 2018; Shi & Han, 2018; Xie et al., 2018). For

instance, MD simulations have been used to investigate intra- and inter-molecular HB interactions and chain dynamics (Rosa, Heux, Cavallé, & Mazeau, 2002), diffusion behavior (Pan et al., 2007), and the glass transition and structural changes (Bermejo & Ugarte, 2010) of PVA composites. In addition, this tool enables the understanding of the governing effect of HB networks on the structure and mechanical properties of graphene oxide (GO) composite paper (Medhekar et al., 2010; X. Yao et al., 2019), and PVA-GO composites (Compton et al., 2012). This means that the MD simulation can help understand the impact of PA molecules on HB, microscopic structure, chain dynamics, and mechanical properties of PVA/PA composites.

This work aims to understand impacts of the PA contents on intermolecular HB, chain dynamics, mechanical properties of antibacterial PVA/PA composite films, and of PVA by combining MD simulations and experimental. In addition to improved antibacterial activities, we show that the addition of PA gradually increases the total H-bond number, but a critical PA content of *ca.* 1.25 wt% is observed for the peak glass transition temperature (T_g), the lowest molecular diffusion, and the highest mechanical strength of the PVA/PA composites. This study sheds light on the mechanisms of chain dynamics and mechanical properties of the PVA/PA composites by combining numerical simulations and experimental, which will ultimately contribute to the design of high-performance biodegradable polymeric materials and expanding the practical applications of PVA/PA composites in packaging, pharmacy, and automotive industries.

5.2 Experimental

Raw Materials. PVA (M_w : 145000 g/mol, degree of hydrolysis: 99%) was purchased from the Aladdin Chemistry Co., Ltd., China, and PA (45 wt% aqueous solution) was bought from the J&K scientific China.

Fabrication of PVA/PA Composite Films. As illustrated in Figure 5.1a, 8.0

wt% aqueous solutions of PVA were prepared by dissolving PVA powder to 95 °C water. Then a predesigned amount of PA in H₂O solutions was added into the PVA solution with moderate stirring for 30 min. After that, the mixture was cast into a glass mold followed by drying for 72 h at room temperature and then 48 h at 60 °C in a vacuum dryer to remove residual water. The dry PVA and PVA/PA films with a mean thickness of 100 μm were peeled off for further characterizations.

Characterizations. The optical transmittance of the PVA and its PA composite films with a thickness of *ca.* 70 μm was recorded on a Varian CARY 100 Bio UV–vis spectrophotometer. The antibacterial activities of PVA and its PA composite films were evaluated using a disc diffusion method. Film samples were cut into 18-mm discs and placed on the surface of agar plates inoculated with 10⁸ CFU/mL of *S. aureus* or *E. coli*. Plates were incubated at 37 °C for 24 h. The diameter of the inhibition zone was measured in mm.

Fourier transform infrared spectrum (FTIR) of composites film was recorded on Nicolet iS50 FTIR instrument (Thermo Fisher, USA) with a resolution of 2 cm⁻¹. The wavelength range is from 4000 to 400 cm⁻¹ and at least 32 scans was used to gain the spectrum. Differential scanning calorimetry (DSC) measurements were carried out on TA Q200 instrument (DSC, USA). A small amount of specimen (5–10 mg) was added into a zero aluminum pan and followed with heat/cool/heat method under nitrogen atmosphere. The temperature range is 0 - 245 °C and the heating/cooling rate is 10 °C/min. The glass transition temperature (T_g) was obtained from the last heating process.

The tensile tests were measured on a SANS universal testing machine (CMT 6000) with a capacity of 200 N, using a test rate of 5 mm/min at 23 ± 2 °C, under a relative humidity of 30 %. Dry PVA films with a typical thickness of 70 (±10) μm were then cut into rectangular specimens with dimensions of 30 × 5 mm². Dynamic mechanical analysis (DMA) was performed using TA Q800 dynamic mechanical analyzer (DMA, USA). The temperature range was from 20 to 150 °C

with a heating rate of 3 °C/min and tests frequency of 1 Hz, 5Hz, 10Hz, respectively.

Molecular dynamic simulation. The molecular interactions dynamics evolution in the PVA/PA composite systems are modeled by Accelrys Material Studio 2018. The PA and PVA molecular structures involved in the simulation are shown in Figure 5.1b. In order to better compare with the experimental data (where the PVA with a degree of hydrolysis of 98.0-98.8 % were used), one single initial atactic PVA chain with repeat units of n=99 is generated and two repeat units CH₂-CHOH) are replaced with -CH₂-CH(O)CH₃. The PVA chain is constructed by amorphous cell module. Each model system includes ten PVA chains and different concentrations of PA molecules (ϕ = 0, 1.5, 2.9, 4.3, 9.6 wt%). The density for the initial configurations is set to 0.8 g/cm³. The periodic boundary conditions (PBC) are applied to avoid surface effects. A set of five configurations for each case are constructed. The positions and velocities of particles contained in the model system are evolved as a function of time. The Verlet velocity algorithm with a time step of 1fs is used to integrate the equations of motion. In the present work, the high-quality COMPASS (Condensed-phase Optimized Molecular Potential for Atomistic Simulation Studies) force field is adopted to model the molecular interactions. The force field has been widely applied to predict the structural and dynamics features of many polymer materials (Choi, Yu, Yang, & Cho, 2011; Jing Li et al., 2019; Qiao et al., 2012). The energy of the system can be approximately estimated as the sum of different contributions which can be classified as the bonded and non-bonded interactions. The non-bonded energy consists of van der Waals and electrostatic interactions in the COMPASS force field.

$$E_{non-bond} = E_{vdW} + E_{Electrostatic} \quad (5.1)$$

In order to avoid that the energy is trapped in temporary minimum energy states, the system is annealed from 300 to 600 K and then down to 300 K again with an interval of 50 K. Next, an NPT (constant number, pressure and temperature)

simulation for 10ns is performed at 298 K. The constant temperature simulations can be implemented through scaling the velocities to a desired temperature or coupling the system to an external thermal bath. Both the Andersen thermostat and Berendsen thermostat methods are commonly used in many MD simulations. Here, the Andersen thermostat is applied to keep the temperature constant. The system pressure is controlled using the Berendsen barostat. Finally, we sample the production data to analyze the trajectories of simulations and calculate the related system properties. To understand the effect of HB interactions on the structures and dynamics of the PVA/PA composites, we study the diffusion behavior of PVA chains, the number of H-bond between the PVA chains and PA molecules, the glass transition temperature, and the elastic modules of PVA/PA composites.

The stress-strain behavior of PVA/PA composites was studied through calculating the Young's modulus from the simulation data (D. Brown & J. H. Clarke, 1991; Haghghatpanah & Bolton, 2013). Each stress component was solely applied. For example, when the normal force along the x direction was applied, all the other components were set to zero. To determine Young's modulus, the normal stress was calculated to average over the three normal components, similarly for the shear stress to measure the shear modulus. For the Young's modulus, the deformation dynamics was carried out through applying the stress from 0 to 1.46 GPa with increasement of 0.02 GPa and then down to 1.4GPa. The procedure ended when the normal strain exceeded 0.2. For the shear modulus, a similar process from 0 to 1.3 GPa with increasement of 0.02 GPa and then down to 1.2 GPa is applied. The procedure ended when the shear strain was higher than 0.12. The Young's and shear moduli can be obtained by linearly fitting the stress (σ) - strain (ϵ) profiles (D. Brown & J. H. Clarke, 1991).

The experimental details are provided in the appendix B.

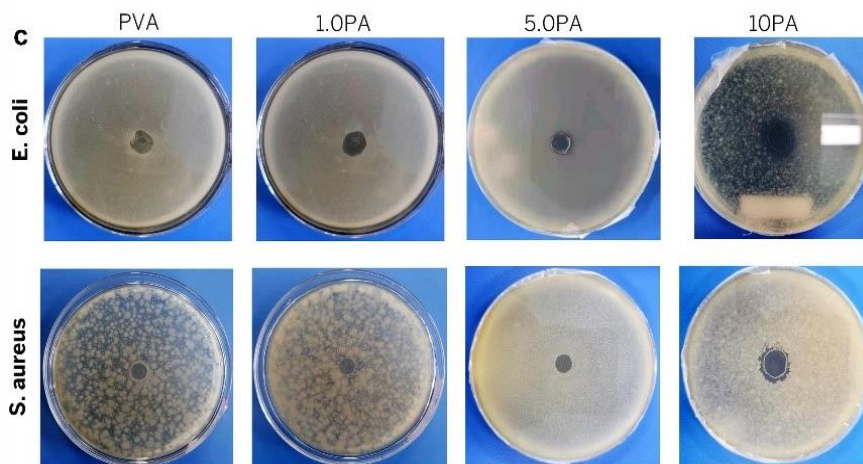
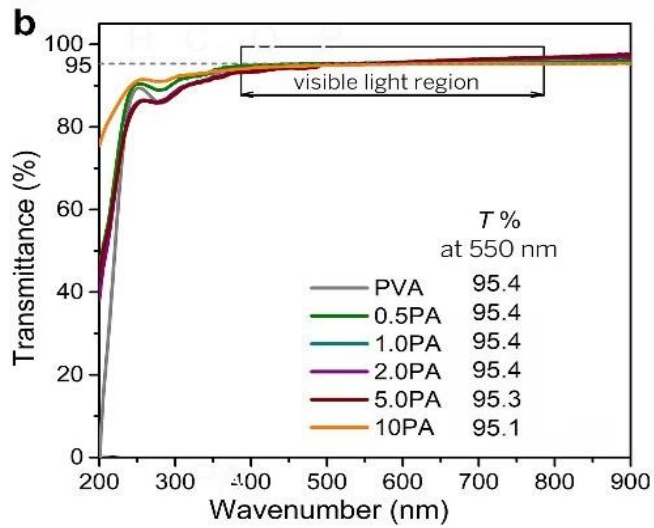
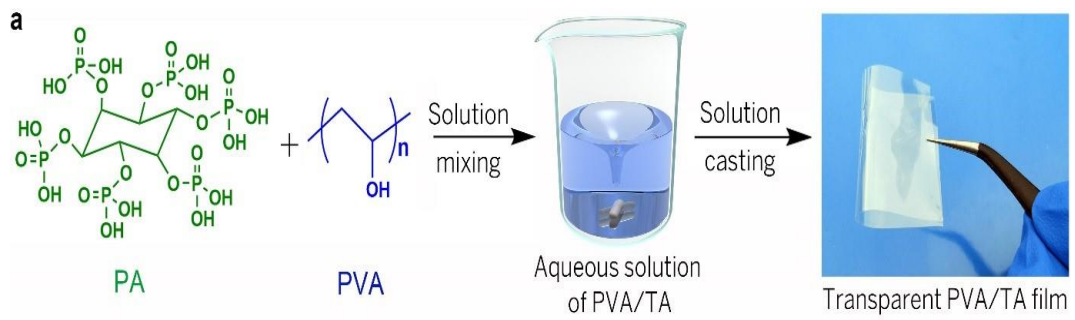


Figure 5.1 a) Illustration for the preparation process of PVA/PA composite films. b) UV-vis spectra of PVA and its PA composite films. c) Antibacterial properties of PVA and its PA composite films against *E. coli* and *S. aureus*.

5.3 Results and Discussion

5.3.1 *Optical and Antibacterial Properties*

As shown in Figure 5.1a, the PVA/PA composite films were prepared by a solution mixing followed by solution casting using water as a co-solvent. The resultant PVA/PA composite films are highly transparent with a high optical transparency above 95% from UV to visible light regions (see Figure 5.1b). As mentioned above, PA molecules have been proven to possess certain antibacterial activities (Gao et al., 2016; Q. Zhou et al., 2019). Therefore, the antibacterial activities of PVA/PA composite films against Gram-positive (*S. aureus*) and Gram-negative (*E. coli*) food-borne pathogenic bacteria were determined by the disc diffusion test (see Figure 5.1c). The pure PVA film does not show an inhibition zone, indicative of no antibacterial ability against both *S. aureus* and *E. coli*. Likewise, the addition of 1.0 wt% PA does not show a significant antibacterial effect on the PVA film regardless of both Grams. Upon the addition of 5 wt% PA, the composite film starts to show an inhibition zone and exhibit a certain antibacterial activity against *E. coli*. An obvious inhibition zone against *S. aureus* and *E. coli* is clearly observed when the PA content rises to 10 wt%, demonstrating that the composite film achieves an improved antibacterial performance against both Grams. The improved antibacterial property of PVA/PA composite opens up a potential opportunity for their applications in future antibacterial food and drug packaging.

5.3.2 *HB Interactions between PVA and PA*

Figure 5.2a shows a snapshot of PVA/PA composites to describe formation of the HB. The density of the pure PVA measured experimentally is about 1.26 g/cm³ (Davidson; Rosa et al., 2002). Previous simulations have indicated that the equilibrium density of the pure PVA with 99 monomers is 1.191 g/cm³ at 300 K,

within the error range of about 3-5% (Bermejo & Ugarte, 2008; H. Sun, 1998). The abundant hydroxyl groups in both PVA and PA (macro)molecules give rise to the formation of extensive inter/intramolecular HB interactions and a H-bond network (Compton et al., 2012; Rosa et al., 2002).

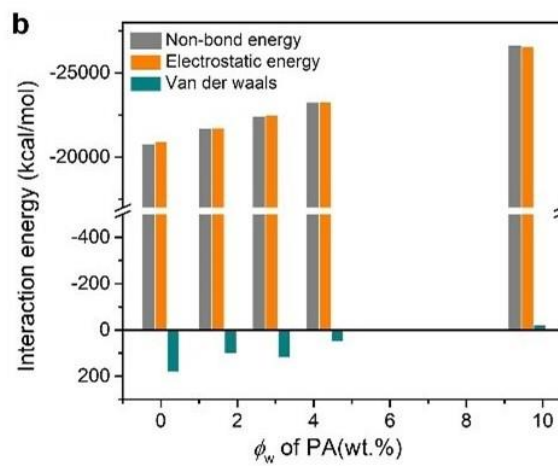
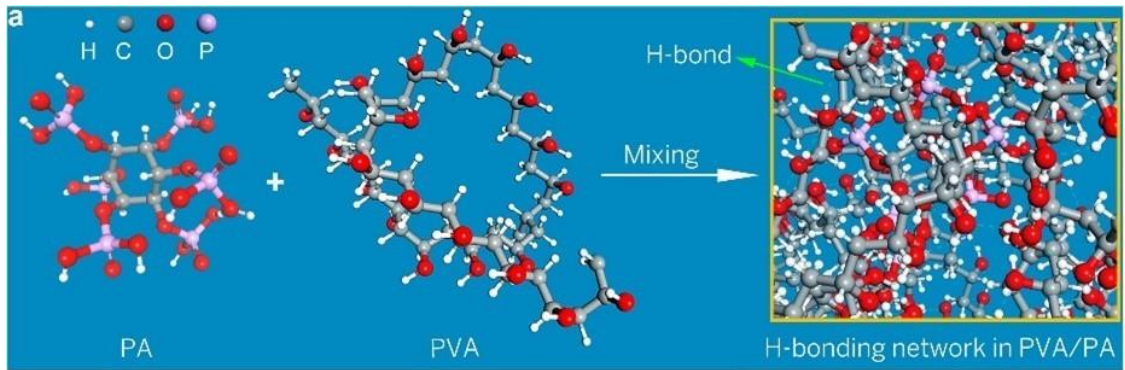


Figure 5.2 (a) snapshot of PVA/PA composites and (b) Non-bonded interaction energy between PVA and PA

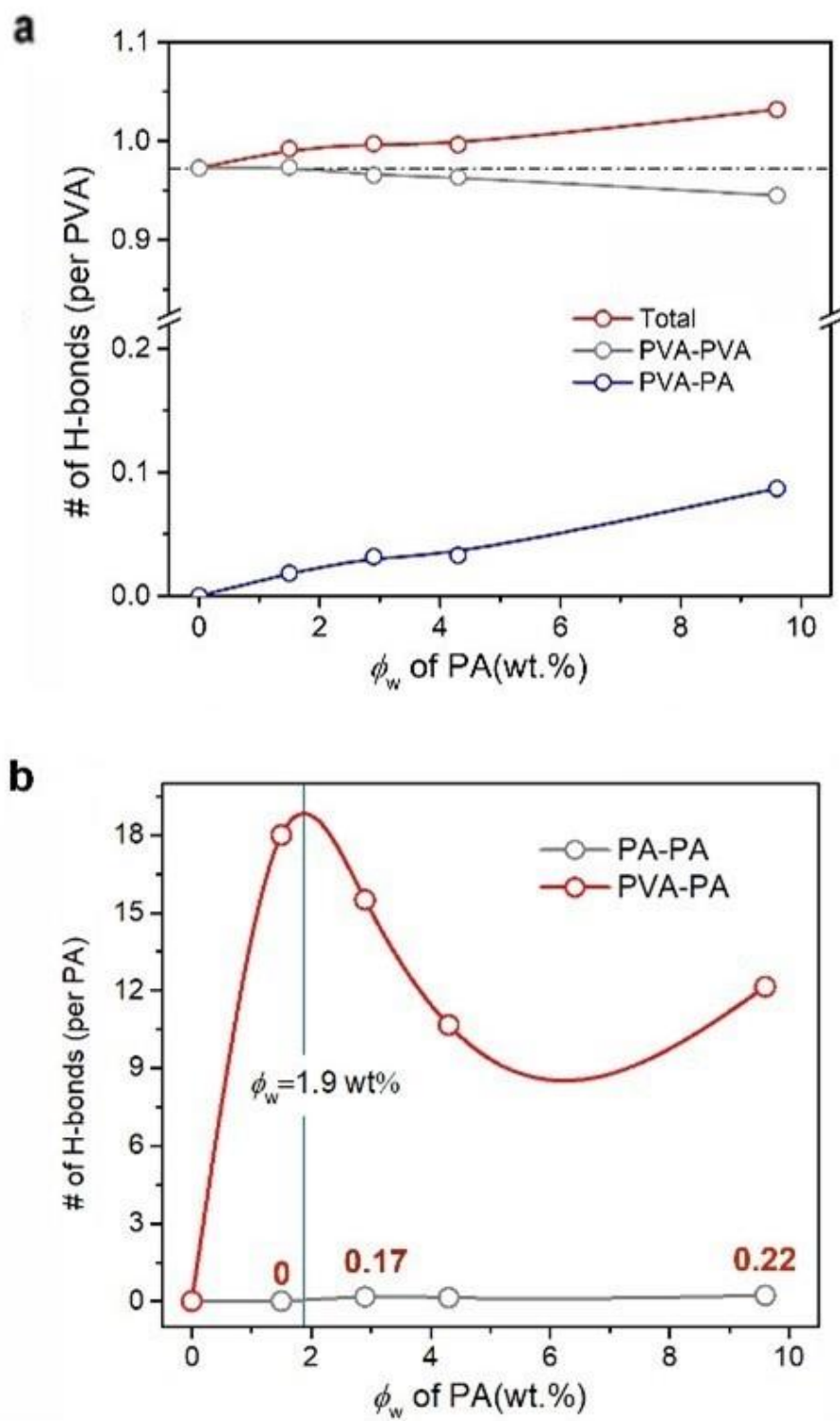


Figure 5.3 H-bond number of each hydroxyl group on (a) PVA and (b) PA as a function of the PA concentration

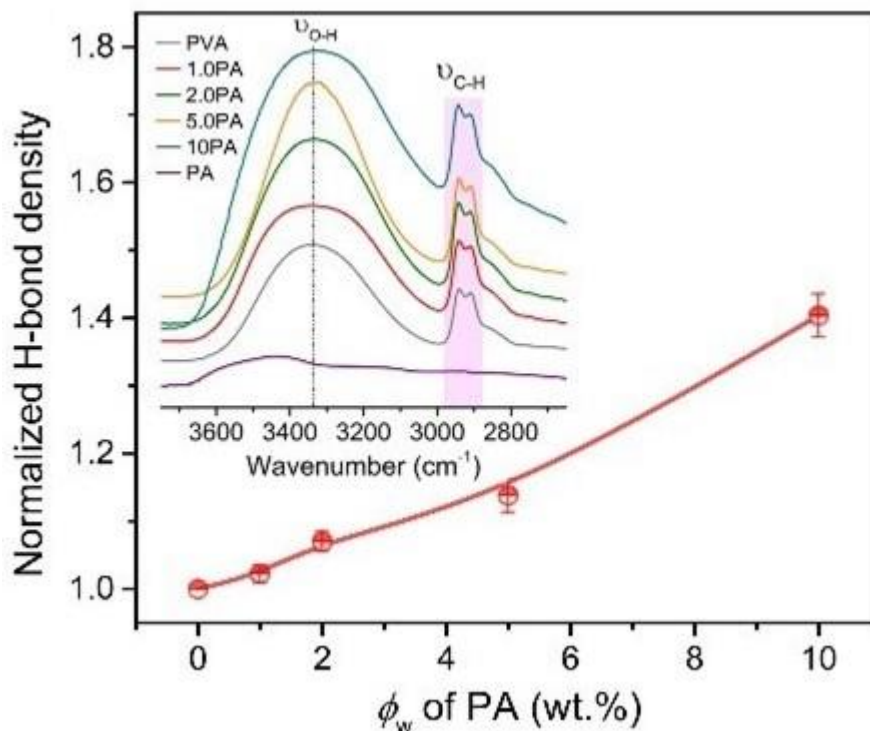


Figure 5.4 normalized H-bond density of PVA/PA composites by comparing the peak area of O-H stretching ($3100\text{--}3650\text{ cm}^{-1}$) and that of C-H absorption.

In general, the non-bonded interactions consist of the electrostatic and van der Waals interactions in the COMPASS force field. The sign of the interaction energy is related to the directionality of force. The non-bonded interaction energies (electrostatic and van der Waals forces) increase with the PA concentration, and the electrostatic part dominates the total interaction energy (see Figure 5.2b). The increased interaction energy (electrostatic energy) strongly indicates that the hydroxyl groups of PA molecules contribute to the non-bonded energy due to the topology formed by highly polar oxygen atoms in PA (e.g., the HB with PVA).

To gain further insights into the molecular interaction in the PVA/PA composites, we further study the impact of the PA concentration on the formation and number of the H-bonds. It is widely recognized that a H-bond is formed between atoms of the donor D and the acceptor A. The geometric definition of the H-bond requires that the D-A distance is less than 3.5 \AA and the angle H-D...A is less than 30° (Joseph & Aluru, 2008). The value of 3.5 Angstroms corresponds to

the first minimum of radial distribution function $g_{D-A}(r)$. There are also some other geometrical definitions to identify the H-bond (Yoshinori Tamai et al., 1996a; Yoshinori Tamai, Hideki Tanaka, & Koichiro Nakanishi, 1996b). These definitions do not affect the distribution of the H-bond. Because H-bonds exist in a dynamic manner, only the statistical results of H-bonds can be calculated. The H-bonds can be influenced by the properties of materials, such as the rigidity of polymers, the size of the additive, and the accessibility of functional groups. The complex interplay among these factors may affect the formation of H-bonds and the HB network structure.

Figure 5.3a gives the normalized number of HB by the number of oxygen groups of PVA, and the insert graph is the average number of H-bonds for each PA molecule as a function of PA concentrations. The results show that the number of PVA-PVA H-bonds steadily decreases whereas the number of PVA-PA H-bonds increases with increasing PA loading levels, indicating strong HB interactions between PVA and PA. This is because the introduction of PA molecules replaces the HB between the PVA chains, thus giving rise to decreased number of PVA-PVA H-bonds (Bermejo & Ugarte, 2010). Moreover, because of more hydroxyl groups in PA than PVA, the magnitude of increase in the number of PVA-PA H-bonds is larger than that of decrease in the number of PVA-PVA H-bonds. As a result, the total number of H-bonds continues to augment as the PA content increases. It should be noted that in Figure 5.3b, the number of PVA-PA H-bonds for each PA molecule reaches the peak value at a critical content of $\phi_w \approx 1.9$ wt % and then goes down to the minimum at a PA content of ca. 6.0 wt %. Meanwhile, the number of PVA-PA H-bonds per PA molecule is much higher than that of PA-PA H-bonds in the whole PA content range, indicating that the H-bonds of PA molecules mainly form with PVA macromolecules regardless of the content of PA. In addition, IR allows us to calculate the normalized H-bond density of PVA/PA composites simply by comparing the specific area ratio of the vibration peak of

hydroxyl groups ($3000\text{-}3650\text{ cm}^{-1}$) and methylene ($2820\text{-}2920\text{ cm}^{-1}$), namely AO-H/AC-H (see Figure CS1) (Song et al., 2018; Song et al., 2017; Song et al., 2013; Song et al., 2015b). The normalized H-bond density (see Figure 5.4) shares a monotonous increase trend with the total H-bonds (Figure 5.3a), indicative of a good agreement between MD and experimental results.

5.3.3 *Structure and chain dynamics*

The radial distribution function (RDF) has been intensively used as an effective means to predict the structure of polymer materials. Figures 5.3a and b show the RDF of intra-chain atoms and inter-chain atoms for the PVA backbones. The first peak is at around 1.5 \AA corresponding to the C-C bond length, whereas the second and third peaks are related to the non-bonded interaction of the PVA chains (see Figure 5.5a). Because the second peaks are much higher than the third ones, we focus on analysis of the second peak. The second peak turns larger at higher PA contents, indicating that intrachain interactions becomes stronger with increasing PA contents.

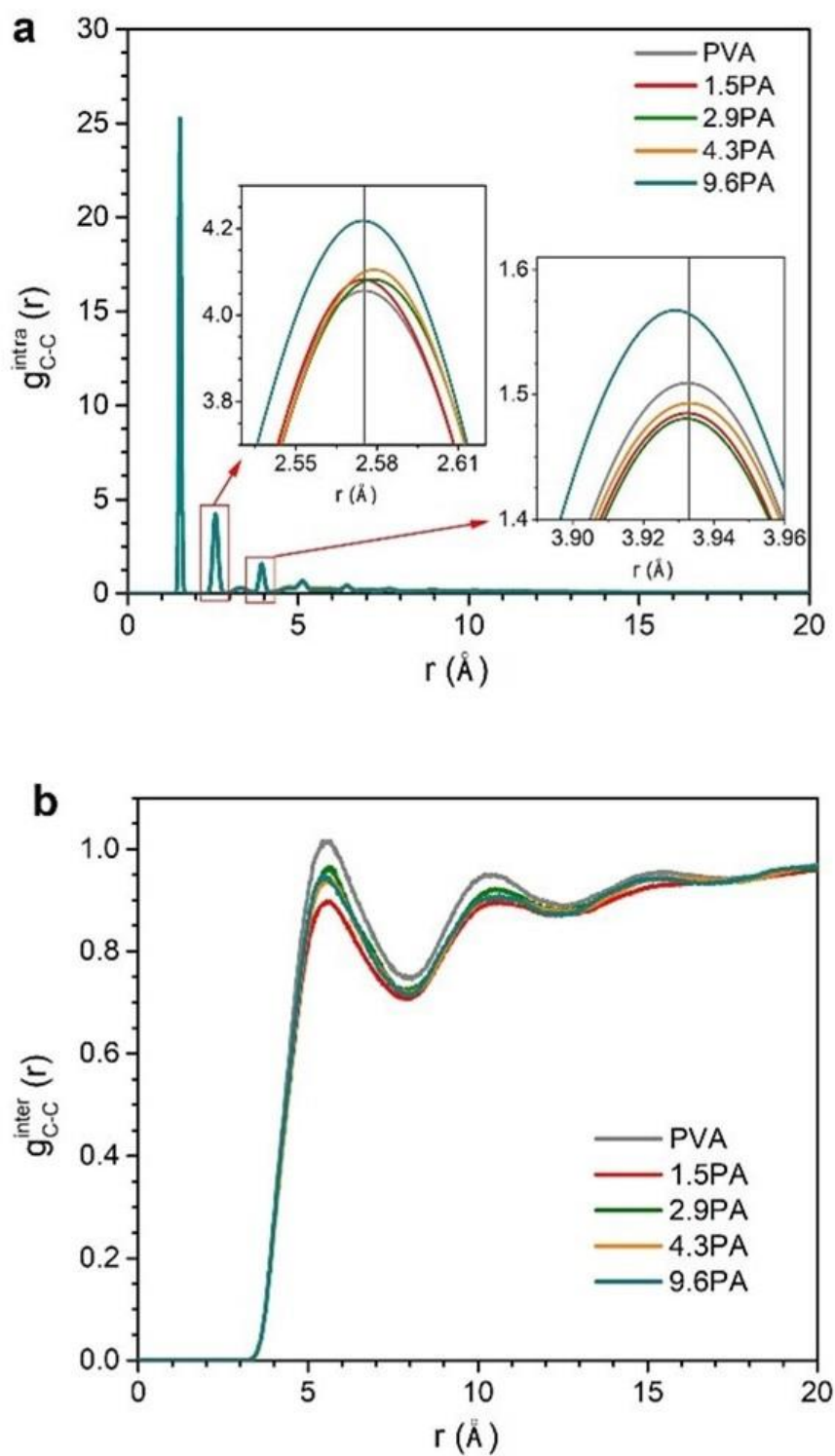


Figure 5.5 (a) Intra- and (b) inter-molecular RDF for the PVA backbones at different PA concentrations

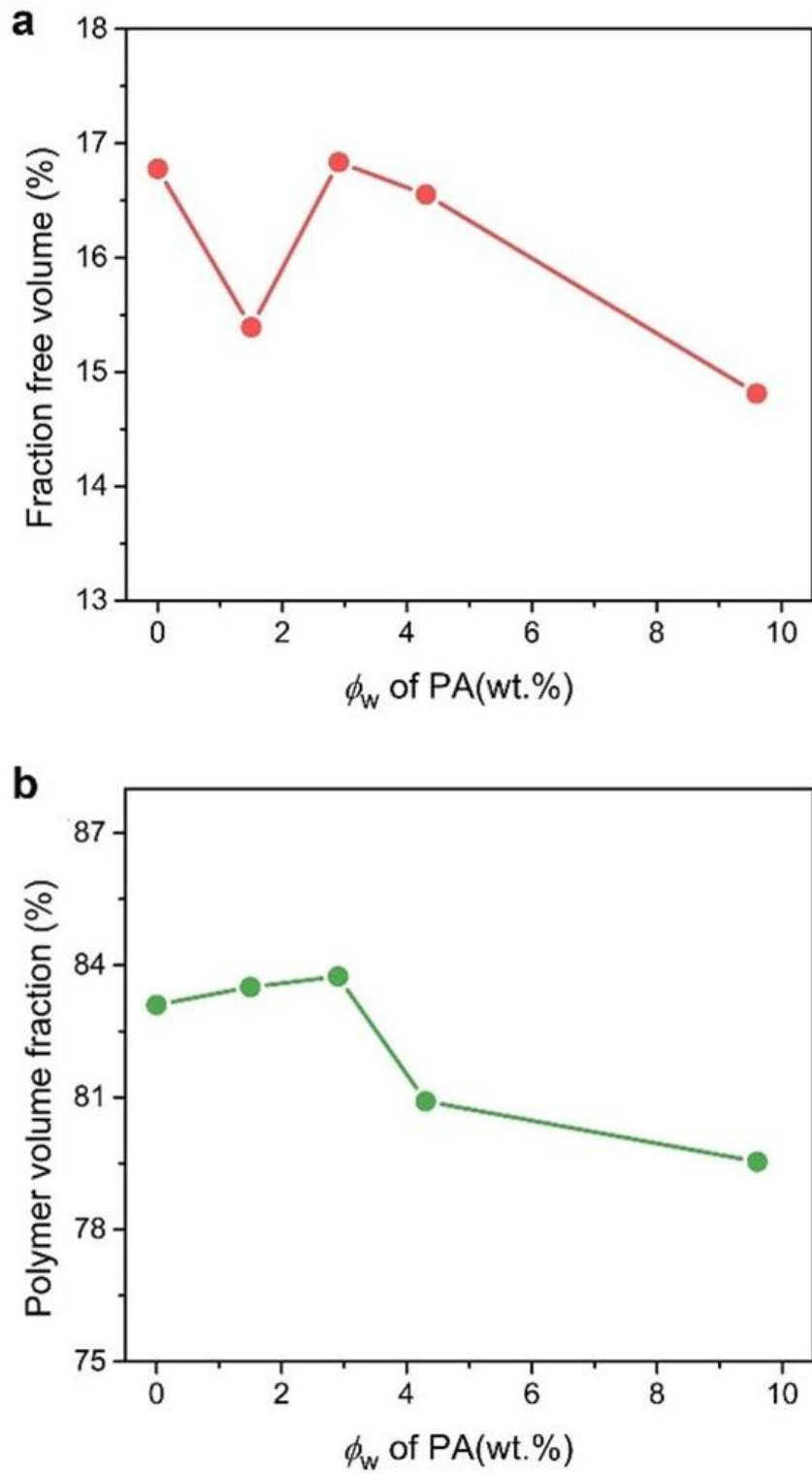


Figure 5.6 (a) fraction volume fraction and (b) polymer volume fraction of PVA/PA composites as a function of the PA concentration (ϕ_w).

The results of interchain interactions (Figure 5.5b) are in good accordance with the previous study, and the values are close to 1.0 at a large distance. The first peak appears at $r=5.4 \text{ \AA}$ and corresponds to the non-bonded interactions between PVA backbones. At a PA content (ϕ_w) of 2.9 wt %, a slightly larger peak appears, implying stronger interactions relative to other PA concentrations. This also means that the PVA matrix becomes more compact, corresponding to a larger polymer volume fraction at $\phi_w = 2.9 \text{ wt\%}$ (Figure 5.6b). In addition, the FFV first reduces sharply until $\phi_w = 1.5 \text{ wt\%}$ and then rebounds to a value close to that of the pure PVA at $\phi_w = 2.9 \text{ wt\%}$, but significantly declines again with a further increase in PA contents (Figure 5.6a). At a low PA concentration less than 1.5 wt%, the addition of small PA molecules fills in the free volume of the pure PVA, resulting in a reduced FFV. With the PA concentration further increasing to $\phi_w = 2.9 \text{ wt\%}$, the excessive PA molecules result in increased FFV values. A further addition of PA molecules decreases the FFV because PA molecules probably tend to form small clusters (as reflected by increased PA-PA H-bonds in Figure 5.2c) to fill the free volume again. In comparison, the increased PA concentration below 2.9 wt% causes a slight increase in the PVA volume fraction instead (Figure 5.6b), mainly arising from a more compact structure of PVA. Likewise, at a $\phi_w > 2.9 \text{ wt\%}$, the polymer volume fraction reduces as well, which means that the HB interactions between PVA chains weaken. With the PA contents continue to increase, the magnitude of decrease of the polymer volume fraction slows down probably due to the formation of PA clusters.

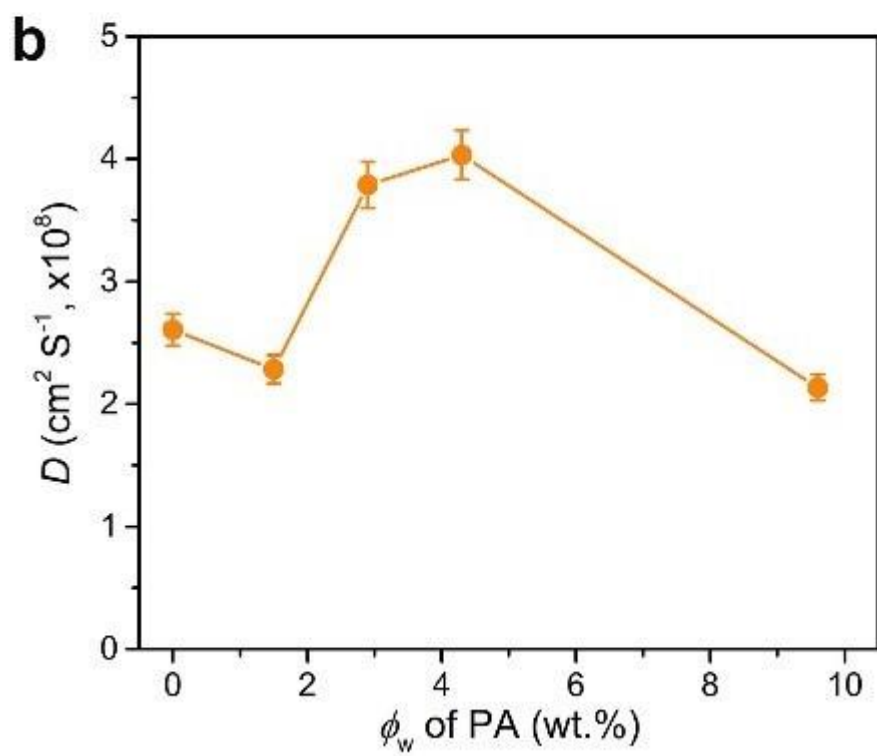
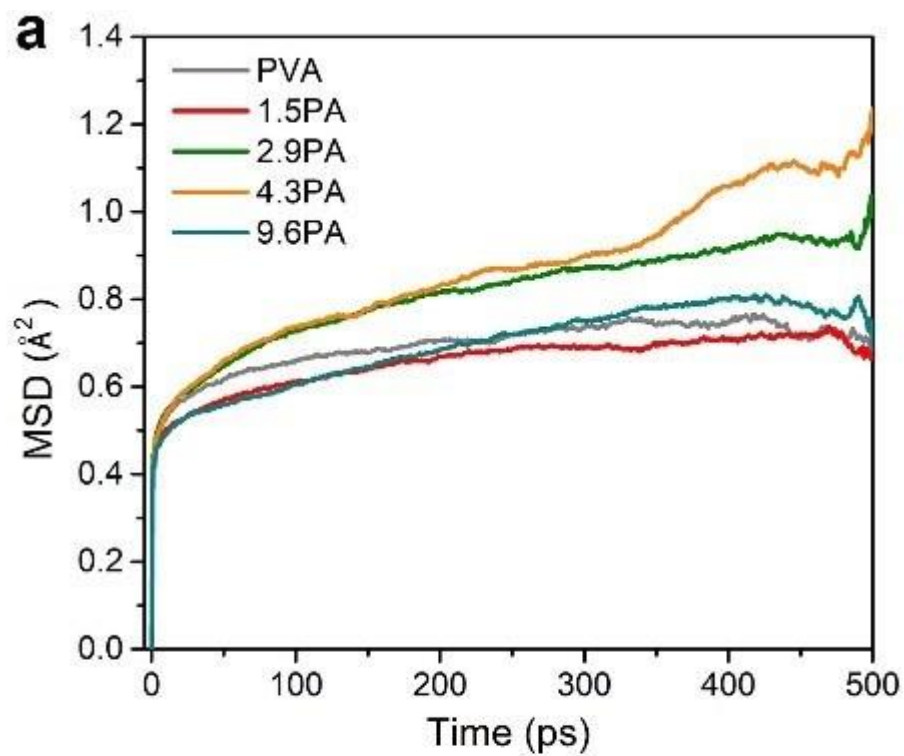


Figure 5.7 (a) MSD curves of PVA chains in the composites as a function of time and (b) dependence of D on the PA concentration

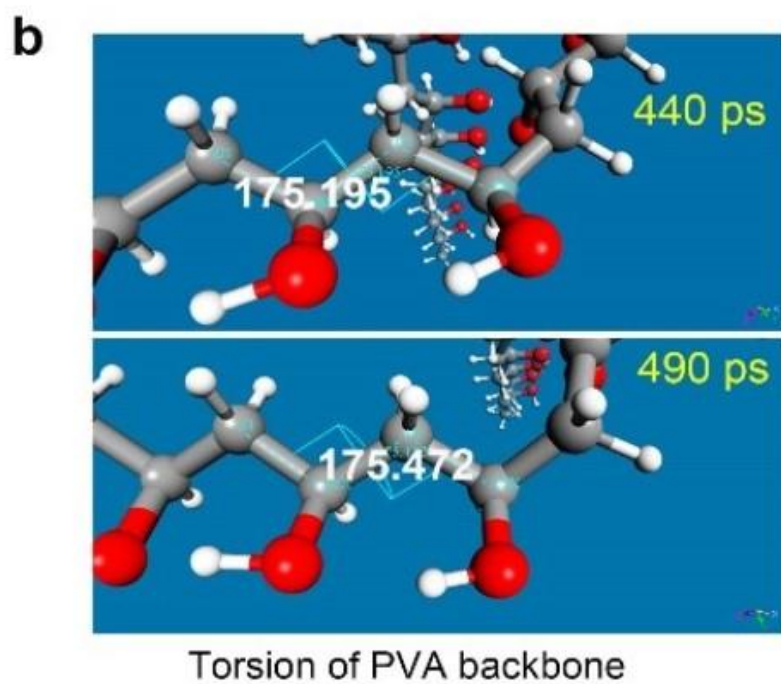
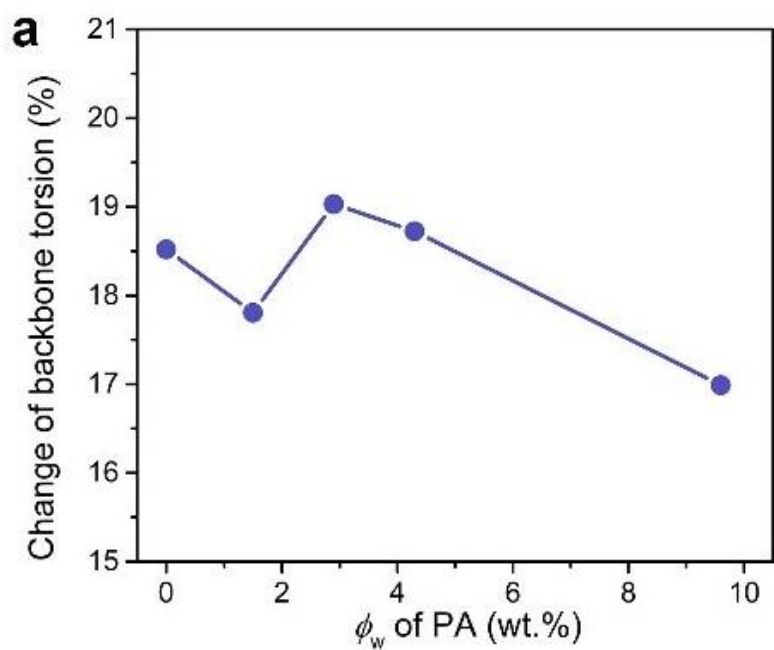


Figure 5. 8 (a) change of backbone torsion of PVA chains, and (b) snapshots for the torsion change of PVA backbones from $t=440$ to 490 ps

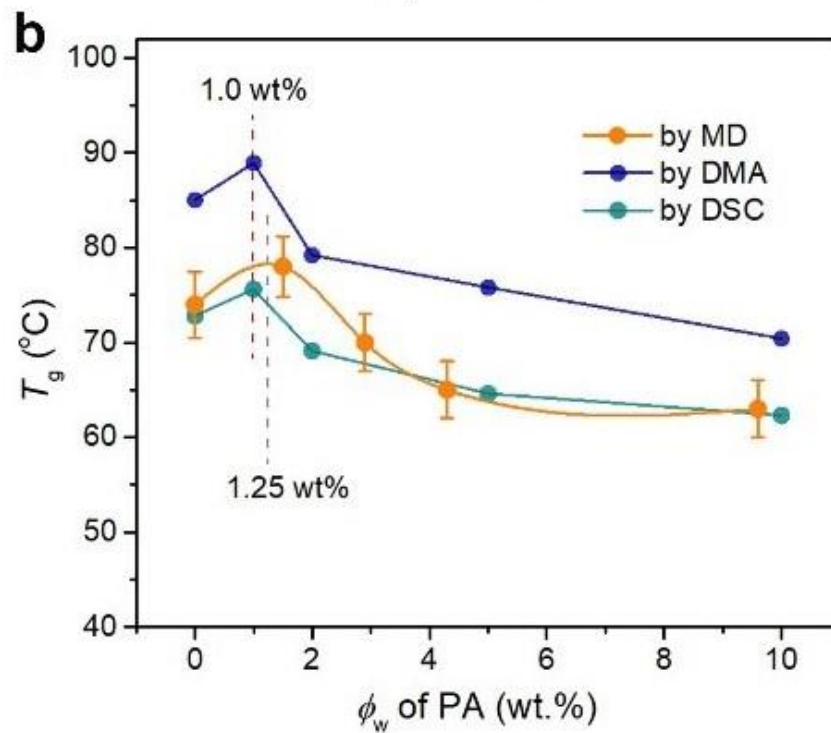
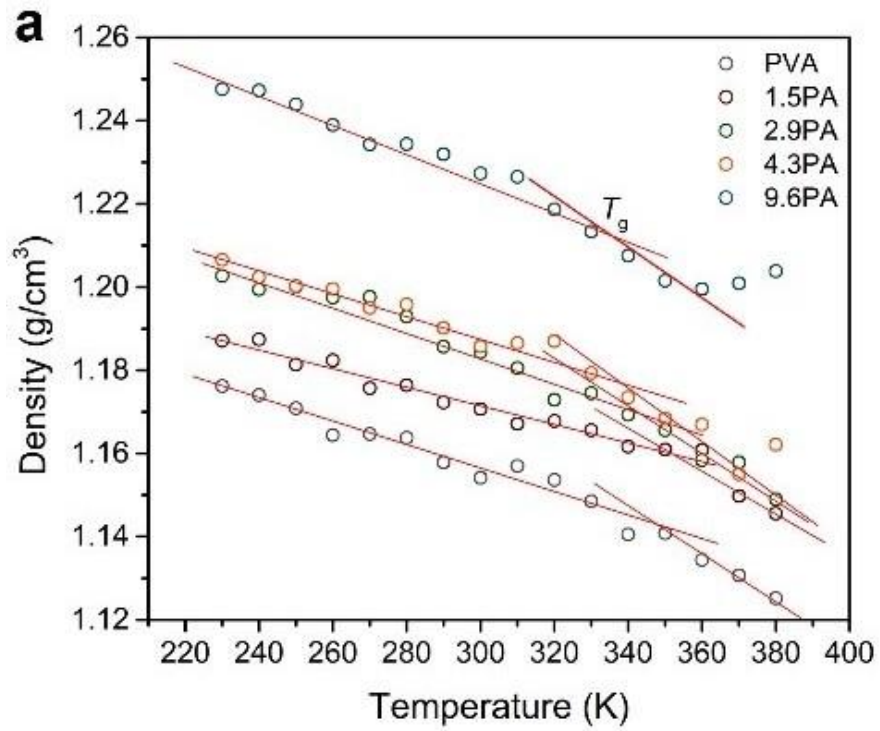


Figure 5.9 (a) Plots of temperature dependence of density, and (b) glass transition temperature (T_g) values of PVA/PA composites as a function of PA concentrations, obtained by MD, DSC and MDA techniques

The mobility and dynamics of PVA chains strongly depends on the surrounding environment, e.g., the HB interactions between PVA and PA (Pan et al., 2007). To understand chain dynamics of PVA, mean square displacement (MSD) curves of PVA chains with various PA concentrations are calculated. The MSD values of PVA chains first increase until a PA content of 4.3 wt%, and then decline with increasing PA contents in the simulated time scale (see Figure 5.7a). The diffusion coefficient (D) is calculated by extracting the slope of the MSD curve to further assess the mobility of chains at 298 K (Florian Müller-Plathe, 1998). As shown in Figure 5.7b, the D values share a similar trend to polymer volume fraction (Figure 5.3d), with increasing PA concentrations. The PVA chains show weaker mobility at $\phi_w=1.5$ and 9.6 wt% than $\phi_w=2.9$ and 4.3 wt %. This is because both 1.5PA and 9.6PA possess smaller FFV relative to other samples (Figure 5.3c), thus allowing less space for the chain movement of PVA and thus reduced diffusion ability. Moreover, this phenomenon can be further explained by measuring the change of torsion of backbone carbons. Generally, a greater change of backbone torsion reflects a higher diffusion coefficient (Bulacu & van der Giessen, 2007). Apparently, the dependence of polymer mobility on the PA concentration is well consistent to the change of backbone torsion (Figure 5.8a), as visually evidenced by the snapshots for the torsion change of PVA backbones at $t=440$ and 490 ps (Figure 5.8b).

The glass transition temperature (T_g) is another important thermodynamic parameter for evaluating the movement of polymer chains. The T_g of polymers is largely determined by many factors, such as free volume, intermolecular interaction, and polymer network topology. In the MD simulations, the simulated T_g value can be calculated by determining the turning point of the density versus temperature (Figure 5.9a). The simulated T_g of PVA is about 352 K agreeing with previous work well (Bermejo & Ugarte, 2010). Upon the addition of PA, the T_g is found to first increase and reach the peak value at 1.25 wt%) followed by a steading

decline as a function of PA concentration (Figure 5.9f). The experimental T_g values clearly verify simulated ones, regardless of experimental methods (DSC and DMA) (see Figures CS2 and CS3), and the maximum T_g value occurs at a PA concentration of 1.0 wt%, very close to the simulated 1.25 wt%. Moreover, the T_g values of all samples obtained by DSC are very consistent to those obtained by MD, despite some deviations for the values by DMA. The 1.0PA sample (or 1.5PA for MD simulation) exhibits the highest T_g because strong HB interactions between PA and PVA and a smaller FFV, thus restricting the movement of PVA segments and torsion of PVA backbones (Bermejo & Ugarte, 2010). At PA contents above 1.25 wt%, the reduction in T_g is most likely due to the plasticization effect of excessive PA molecules on the PVA. Overall, the chain dynamics (D , T_g) of PVA/PA complexes are strongly dependent on the intermolecular interactions (HB) and structure (FFV).

5.3.4 Mechanical properties

Generally, the intermolecular interactions and movements strongly determine the mechanical properties of polymeric materials. The strength and stiffness (or resistance to the deformation) of PVA/PA composites can be obtained through stress-strain curves and elastic modulus (E) by MD simulations. Figure 5.10a presents typical stress-strain curves of PVA, 1.5PA and 9.6 PA. The stress of both PVA and the PVA/PA composites shows a linear growth within 10% strain, and then yields until 20% strain. The detailed values of tensile stress (σ_m) and elastic modulus (E) are calculated from curves and listed in Table 5.1. The MD results show that the σ_m values first increase and then decline with increasing loading level of PA. Moreover, their experimental values share the same trend, further validating the MD results despite their value differences (Figure 5.10b). The simulated and experimental tensile strength pure PVA are 315 and 115 MPa, respectively. The 1.5PA system presents the highest strength of 347 MPa (by MD),

which is well consistent to the corresponding experimental value that a relatively higher σ_m of 118 MPa is achieved for both 1.0PA and 2.0PA (Figure CS4). This implies that the maximum σ_m is achieved at a PA content of ~ 2.0 wt%, agreeing well with the greatest number of PVA-PA H-bonds per PA molecule at 1.9 wt% (Figure 5.2c). It should be noted that the simulated σ_m values are about 2-3 times higher than their corresponding experimental data, which is due to far higher strain rate in MD simulations than the experiment (Odegard et al., 2014) as well as the unavoidable defects of the samples

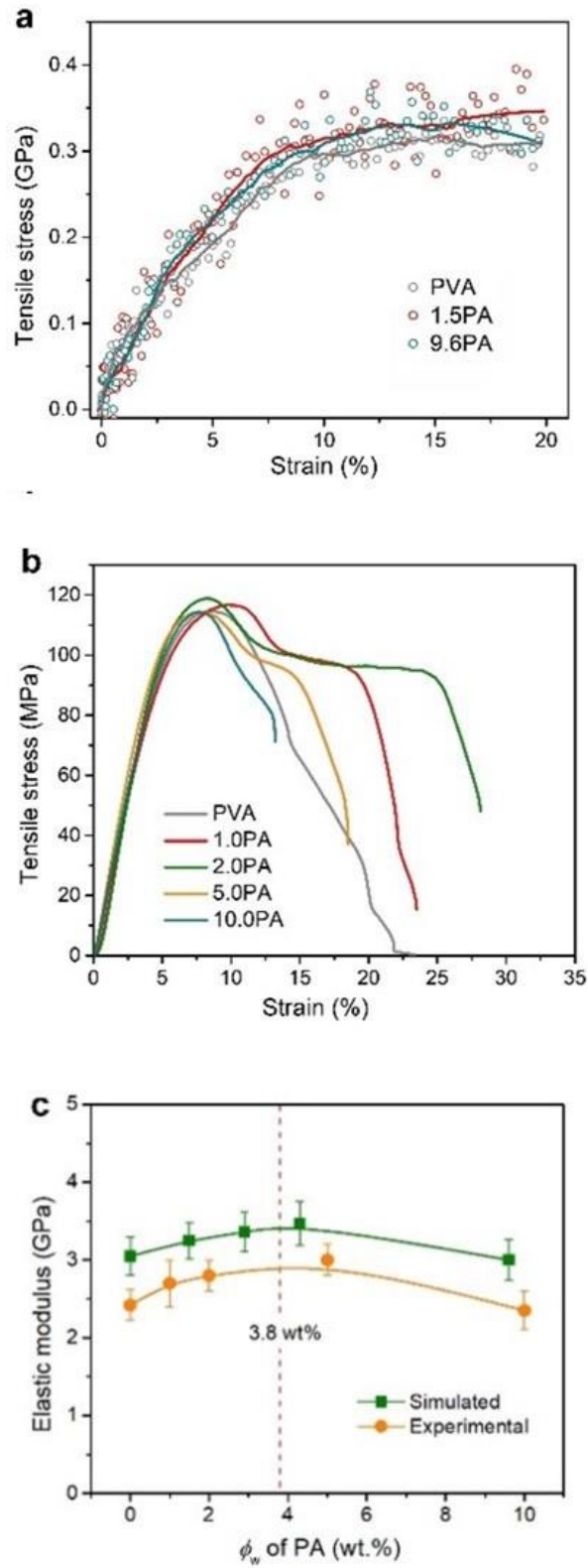


Figure 5.10 Stress-strain curves of PVA and PVA/PA composites obtained from (a) MD simulations and (b) experiments. (c) Elastic modulus PVA/PA composites as a function of PA concentrations.

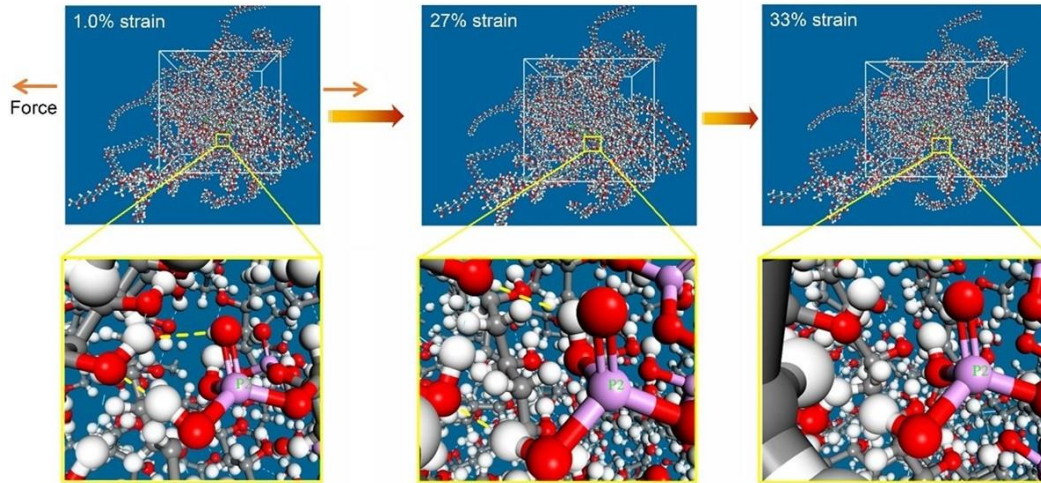


Figure 5.11 Snapshots under the tensile deformation of the 9.6PA sample at tensile strain of 1.0%, 27% and 33% during uniaxial tension.

Table 5.1 Detailed mechanical properties including tensile strength, elastic modulus, stain at failure, obtained from tensile tests and MD simulations.

Run	σ_m^a (MPa)	E^a (GPa)	ε_b^a (%)	E' (GPa) at 25°C	E' (GPa) at 70°C
PVA	115 ± 3.9	2.41 ± 0.22	30 ± 14	5.25	0.956
PVA †	315 ± 12 †	3.05 ± 0.25 †	–		
1.0PA	118 ± 4.9	2.74 ± 0.30	38 ± 14	5.49	1.39
1.5PA †	347 ± 20 †	3.25 ± 0.28 †	–		
2.0PA	118 ± 4.1	2.82 ± 0.20	41 ± 13	5.67	0.739
2.9PA †	342 ± 23 †	3.36 ± 0.26 †	–		
4.3PA †	340 ± 25 †	3.47 ± 0.27 †	–		
5.0PA	115 ± 3.8	3.05 ± 0.20	24 ± 6.0	5.70	0.727
9.6PA †	326 ± 18 †	3.02 ± 0.25 †	–		
10.0PA	114 ± 4.6	2.32 ± 0.30	18 ± 6.0	5.22	0.732

^a σ_m , E , ε_b , respectively refers to tensile strength, elastic modulus, and elongation at break.

^b E' refers to the storage modulus, obtained from DMA measurements. † The data were obtained by MD simulation.

Likewise, the elastic modulus (E) of the PVA/PA composites also first increases followed by a steady reduction with increasing PA contents. The

simulated moduli show the same trend as the experimental values, and their values are also comparable in the whole PA concentration range (Figure 5.10c). For instance, the pure PVA shows an E of 2.41 GPa (experimental, tensile) and 3.05 GPa (simulated). At a PA content of ~ 3.8 wt%, the E value reaches the maximum value for both simulated (~ 3.40 GPa) and experimental (~ 2.90 GPa) values. In addition, the storage modulus (E') of PVA/PA composites obtained from DMA behaves in a similar manner to both tensile and MD results (Table 5.1). This is mainly because the number of H-bonds between PVA and PA reaches the maximum at $\phi_w=2.9$ wt% (Figure 5.3a). In addition, Figure 5.11 presents a visual observation on the dynamic change of H-bonds with increasing strain during uniaxial tension, where dynamic H-bonds (yellow dash lines) break and reform again (Jiajun Li et al., 2020; P. A. Song & H. Wang, 2020; Song et al., 2015a).

5.4 Conclusions

In this work, we have comprehensively investigated the impact of PA contents on the optical, antibacterial, H-bond interactions, structure (FFV), glass transition temperature and mechanical properties of PVA. The addition of PA has no negative effect on the transparency of PVA films, but a good antibacterial ability is achieved when 10 wt% PA is added. The number of PVA-PA H-bonds per PA molecule reaches the peak at a PA content $\phi_w \approx 1.9$ wt%, and a further increase of PA concentration gives rise to reduced PVA-PA H-bond number and increased PA-PA H-bond number. Both the FFV and D experience a first decrease and then increase followed by steady decrease. In comparison, the T_g of the PVA reaches the peak value at a critical ϕ_w of 1.0-1.25 wt%. The tensile strength and elastic modulus of PVA/PA composites reach their peak value at $\phi_w \approx 2.0$ wt% and 3.8 wt%, respectively. As mentioned above, the different optimized properties are found at different PA contents according to simulations and experiments. The high glass transition temperature and tensile strength occur in close range of the PVA content.

However, good antibacterial ability is identified at 10wt% PA. Therefore, to obtain excellent mechanical properties, we have to sacrifice antibacterial ability to some extent. In addition to demonstrating the antibacterial activity of PA in PVA, this work provides an insight into the relationship between the intermolecular interactions and chain dynamics and macroscopic properties of polymer composites.

CHAPTER 6: CONCLUSIONS AND FUTURE RESEARCH

6.1 Conclusion

In the present thesis, we employed MD simulations and experimental methods to investigate the structural properties and dynamics behaviors of the PVA materials by the addition of small molecules: water, 4N-2456 and PA. The results indicate that the MD simulations can be used as a complementary approach to experiments to study the PVA/small molecule composites. The findings based on the combination method provide insights into the effects of small molecules on various properties of the PVA composites.

In the first project (Chapter 3), the effects of the water content on the mechanical properties, glass transition, free volume and intermolecular HB interactions of PVA are analyzed systematically through experiments and MD simulations. The mechanical properties of PVA, such as strength and elastic modulus, exhibit obvious dependence on the water content. The increase of the water content results in decrease of the glass transition temperature and enhancement of the relaxation and mobility of PVA chains. The HB interactions in the PVA/water system play a critical role in determining the structural characteristics and mechanical behaviors. It was found that the HB interactions of the PVA bulk are influenced due to formation of PVA-water H-bonds, which can weaken the intermolecular HB interactions between the PVA chains, and reduce the degree of crystallinity. At high water content, water clusters begin to form and thus causes a lubricating effect on the PVA chains.

The second project (Chapter 4) focuses on investigation on the effects of the 4N-2456 concentration on the free volume, chain mobility, glass transition, H-bond interactions and mechanical properties of the PVA composites by MD

simulations. The range of the 4N-2456 concentration studied is set at 0-20 wt%. We found that 5.0 wt% is an optimal concentration for many properties of the PVA/4N-2456 composites, because at this concentration, the low chain mobility, the highest glass transition temperature and the highest elastic modulus of PVA are identified. When the 4N-2456 concentration is below 5.0 wt%, the 4N-2456 molecules can suppress the chain mobility and lead to increase of the glass transition temperature and the elastic modulus due to enhanced H-bond cross-linking effect. If the concentration exceeds 5.0 wt%, some 4N-2456 molecules form clusters. The lubrication effect of the 4N-2456 clusters and weakened H-bond interactions between the PVA chains induce decrease in glass transition temperature and elastic modulus.

In the final project (Chapter 5), we study the optical, antibacterial, H-bond interactions, structure (FFV), glass transition temperature and mechanical properties of PVA in the addition of PA. At 1.9 wt%, there is the largest number of PVA-PA H-bonds per PA molecule, and higher PA concentration leads to decrease of the number of PVA-PA H-bonds and increase of the number of PA-PA H-bonds. The simulation and experimental results indicate that the composites reach different optimized properties at different PA contents. The glass transition temperature of PVA/PA composites reaches the peak value at 1.0-1.25wt%. The tensile strength and elastic modulus become largest at 2.0 wt% and 3.8 wt%, while a good antibacterial ability appears at 10 wt%.

6.2 Future research

In the present thesis, different properties for three kinds of composites of PVA with water, 4N-2456 and PA molecules were studied based on experiments and molecular dynamics simulations. Though we obtain some insight into the formation of the composites and their mechanical properties on molecular levels, the molecular models still need improvement for quantitative predication and

larger systems. Additionally, it is required to explore new PVA composites for emerging applications such as wearable electronic devices. The future works will focus on some composites of PVA with carbon-based materials and electro-conductive polymers as well as model improvements.

Stretchable polymer materials have been widely applied in wearable electronic devices and have received much attention. Electro-conductive polymer hydrogels are considered as promising candidates for the fabrication of wearable electronic devices. However, for most polymer hydrogels weak mechanical strength and biological incompatibility limit their applications in wearable electronic devices. PVA hydrogels exhibit good mechanical properties (high flexibility and stretchability), large water content and good biocompatibility, and have been widely used in wearable electronic devices. However, in many practical applications PVA electro-conductive polymer hydrogels suffer from weak mechanical strength and low electro-conductivity. In the further work, we will investigate composites of PVA with carbon-based materials and electro-conductive polymers (such as Poly(3,4-ethylenedioxythiophene): poly(styrenesulfonate)) through molecular modeling methods and experiments. By analyzing their microscopic structures and dynamics, we can understand physical mechanisms on the mechanical response and electro-conductivity of flexible electro-conductive composite films. According to this, suitable composition for the composites can be explored to improve mechanical strength and electro-conductivity.

All-atom MD simulations can provide abundant microscopic details for calculating various structural and dynamics properties of molecular systems, but is prohibitively expensive in computing cost. As a result, it is limited to simulate small systems typically within tens of nanometers and occurring on nanosecond scale. To predict the behaviors for larger systems, it is required to develop new modeling methods. In future works, we will explore modeling methods based on coarse-grained models and multiscale computational methods. By using these

methods we can analyze large-scale structural characteristics of the PVA composites and their mechanical responses in longer time scales. Additionally, to improve molecular modeling precision and simulate bond breaking behavior under extreme extension, we also will use reactive force-fields, such as ReaxFF, for modeling the composite systems.

REFERENCES

- Abd Alla, S. G., Nizam El-Din, H. M., & El-Naggar, A. W. M. (2006). Electron beam synthesis and characterization of poly(vinyl alcohol)/montmorillonite nanocomposites. *J. Appl. Polym. Sci.*, *102*(2), 1129-1138.
- Ackbarow, T., & Buehler, M. J. (2008). Hierarchical Coexistence of Universality and Diversity Controls Robustness and Multi-Functionality in Protein Materials. *J. Comput. Theor. Nanosci.*, *vol. 5, issue 7*, pp. 1193-1204, *5*(7), 1193-1204.
- Alexy, P., Kachova, D., Krsiak, M., Bakos, D., & Simkova, B. (2002). Poly(vinyl alcohol) stabilisation in thermoplastic processing. *Polym. Degrad. Stabil.*, *78*(3), 413-421.
- Andersen, & Hans, C. (1980). Molecular dynamics simulations at constant pressure and/or temperature. *J Chem. Phys.*, *72*(4), 2384-2393.
- Angell, C., Sare, J., & Sare, E. (1978). Glass transition temperatures for simple molecular liquids and their binary solutions. *J. Phys. Chem.*, *82*(24), 2622-2629.
- Anseth, K. S., Metters, A. T., Bryant, S. J., Martens, P. J., Elisseeff, J. H., & Bowman, C. N. (2002). In situ forming degradable networks and their application in tissue engineering and drug delivery. *J. Control Release*, *78*(1), 199-209.
- Bader, R. F. W. (1994). Atoms in Molecules: A Quantum Theory. *360*(1-3), 1.
- Barthelat, F., Yin, Z., & Buehler, M. J. (2016). Structure and mechanics of interfaces in biological materials. *Nat. Rev. Mater.*, *1*(4).
- Basta, A. H., & Lotfy, V. F. (2019). Assessment of carbohydrate derivatives as synergistic with carbon materials in production environmentally friendly agro-based composites. *Compos. Commun.*, *16*, 94-105.

- Berendsen, H. J. C., Postma, J. P. M., van Gunsteren, W. F., DiNola, A., & Haak, J. R. (1984). Molecular dynamics with coupling to an external bath. *J. Chem. Phys.*, *81*(8), 3684-3690.
- Bermejo, J. S., & Ugarte, C. M. (2008). Influence of water content on structure and mobility of polyvinyl alcohol: A molecular dynamics simulation. *J. Chem. Phys.*, *129*(15), 154907.
- Bermejo, J. S., & Ugarte, C. M. (2010). Influence of Cross-Linking Density on the Glass Transition and Structure of Chemically Cross-Linked PVA: A Molecular Dynamics Study. *Macromol. Theor. Simul.*, *18*(6), 317-327.
- Bonderer, L. J., Studart, A. R., & Gauckler, L. J. (2008). Bioinspired design and assembly of platelet reinforced polymer films. *Science*, *319*(5866), 1069-1073.
- Briscoe, B., Luckham, P., & Zhu, S. (2000). The effects of hydrogen bonding upon the viscosity of aqueous poly(vinyl alcohol) solutions. *Polymer*, *41*(10), 3851-3860.
- Brockwell, D. J., Paci, E., Zinober, R. C., Beddard, G. S., Olmsted, P. D., Smith, D. A., . . . Radford, S. E. (2003). Pulling geometry defines the mechanical resistance of a β -sheet protein. *Nat. Struct. Mol. Biol.*, *10*(9), 731-737.
- Brown, D., & Clarke, J. H. (1991). Molecular dynamics simulation of an amorphous polymer under tension. 1. Phenomenology. *Macromolecules*, *24*(8), 2075-2082.
- Brown, D., & Clarke, J. H. R. (1991). Molecular dynamics simulation of an amorphous polymer under tension. 1. Phenomenology. *Macromolecules*, *24*(8), 2075-2082.
- Buehler, M. J., & Yung, Y. C. (2009). Deformation and failure of protein materials in physiologically extreme conditions and disease. *Nat. Mater.*, *8*(3), 175-188.
- Bulacu, M., & van der Giessen, E. (2007). Molecular-dynamics simulation study of the glass transition in amorphous polymers with controlled chain

- stiffness. *Phys. Rev. E*, 76(1), 011807.
- Butcher, J. C. (2010). Numerical Methods for Ordinary Differential Equations. *Comput. Math. Math. Phys.*, 53(2-3), 153-170.
- Cazon, P., Vazquez, M., & Velazquez, G. (2020). Environmentally Friendly Films Combining Bacterial Cellulose, Chitosan, and Polyvinyl Alcohol: Effect of Water Activity on Barrier, Mechanical, and Optical Properties. *Biomacromolecules*, 21(2), 753-760.
- Cheng, H. K. F., Sahoo, N. G., Tan, Y. P., Pan, Y., Bao, H., Li, L., . . . Zhao, J. (2012). Poly (vinyl alcohol) nanocomposites filled with poly (vinyl alcohol)-grafted graphene oxide. *ACS Appl. Mater. Interfaces*, 4(5), 2387-2394.
- Cheng, Q., Jiang, L., & Tang, Z. (2014). Bioinspired Layered Materials with Superior Mechanical Performance. *Accounts. Chem. Res.*, 47(4), 1256-1266.
- Cheng, Q., Wu, M., Li, M., Jiang, L., & Tang, Z. (2013). Ultratough Artificial Nacre Based on Conjugated Cross-linked Graphene Oxide. *Angew. Chem. Int. Edit.*, 52(13), 3750-3755.
- Chiessi, E., Cavalieri, F., & Paradossi, G. (2005). Supercooled Water in PVA Matrixes. II. A Molecular Dynamics Simulation Study and Comparison with QENS Results. *J. Phys. Chem. B*, 109(16), 8091-8096.
- Chiessi, E., Cavalieri, F., & Paradossi, G. (2007). Water and polymer dynamics in chemically cross-linked hydrogels of poly (vinyl alcohol): A molecular dynamics simulation study. *J. Phys. Chem. B*, 111(11), 2820-2827.
- Chiessi, E., Francesca Cavalieri, A., & Paradossi, G. (2007). Water and Polymer Dynamics in Chemically Cross-Linked Hydrogels of Poly(vinyl alcohol): A Molecular Dynamics Simulation Study. *J. Phys. Chem. B*, 111(11).
- Choi, J., Yu, S., Yang, S., & Cho, M. (2011). The glass transition and thermoelastic behavior of epoxy-based nanocomposites: A molecular dynamics study. *Polymer*, 52(22), 5197-5203.

- Compton, O. C., Cranford, S. W., Putz, K. W., An, Z., Brinson, L. C., Buehler, M. J., & Nguyen, S. B. T. (2012). Tuning the Mechanical Properties of Graphene Oxide Paper and Its Associated Polymer Nanocomposites by Controlling Cooperative Intersheet Hydrogen Bonding. *Acs Nano*, 6(3), 2008.
- Connolly, M. L. (1983). Solvent-accessible surfaces of proteins and nucleic acids. *Science*, 221(4612), 709-713.
- Consolati, G., Genco, I., Pegoraro, M., & Zanderighi, L. (1996). Positron annihilation lifetime (PAL) in poly [1-(trimethyl-silyl) propine](PTMSP): Free volume determination and time dependence of permeability. *J. Polym. Sci., Part B: Polym. Phys.*, 34(2), 357-367.
- Cui, S., Li, L., & Wang, Q. (2020). Improved molecular chain constraint of poly (propylene carbonate) composites by the synergistic effect of poly (vinyl alcohol) and carbon nanotubes. *Compos Part B-Eng*, 194, 108074.
- Davidson, R. *Handbook of water-soluble gums and resins*: McGraw-Hill.
- Desiraju, G. R. (2002). Hydrogen Bridges in Crystal Engineering: Interactions without Borders. *Acc. Chem. Res.*, 35(7), 565-573.
- Desiraju, G. R., & Steiner, T. (1999). *The Weak Hydrogen Bond in Structural Chemistry and Biology*: Oxford University Press.
- Ding, J., Chen, S. C., Wang, X. L., & Wang, Y. Z. (2009). Synthesis and Properties of Thermoplastic Poly(vinyl Alcohol)-Graft-Lactic Acid Copolymers. *Ind. Eng. Chem. Res.*, 48(2), 788-793.
- Du, N., Liu, X. Y., Narayanan, J., Li, L., Lim, M. L. M., & Li, D. (2006). Design of Superior Spider Silk: From Nanostructure to Mechanical Properties. *Biophys. J.*, 91(12), 4528-4535.
- Eom, K., Li, P.-C., Makarov, D. E., & Rodin, G. J. (2003). Relationship between the Mechanical Properties and Topology of Cross-Linked Polymer Molecules: Parallel Strands Maximize the Strength of Model Polymers and Protein Domains. *J. Phys. Chem. B*, 107(34), 8730-8733.

- Fragiadakis, D., Pissis, P., & Bokobza, L. (2005). Glass transition and molecular dynamics in poly(dimethylsiloxane)/silica nanocomposites. *Polymer*, *46*(16), 6001-6008.
- Gao, X., Lu, K., Xu, L., Xu, H., Lu, H., Gao, F., . . . Ma, H. (2016). Excellent anti-corrosive pretreatment layer on iron substrate based on three-dimensional porous phytic acid/silane hybrid. *Nanoscale*, *8*(3), 1555-1564.
- Grabowski, S. J. (2006). *Hydrogen bonding - New insights*: Springer Netherlands.
- Guan, Y., Shao, L., Dong, D., Wang, F., Zhang, Y., & Wang, Y. (2016). Bio-inspired natural polyphenol cross-linking poly(vinyl alcohol) films with strong integrated strength and toughness. *RSC Adv.*, *6*(74), 69966-69972.
- Gunge, A., Koppad, P. G., Nagamadhu, M., Kivade, S., & Murthy, K. V. S. (2019). Study on mechanical properties of alkali treated plain woven banana fabric reinforced biodegradable composites. *Compos. Commun.*, *13*, 47-51.
- Guo, T., Heng, L., Wang, M., Wang, J., & Jiang, L. (2016). Robust Underwater Oil-Repellent Material Inspired by Columnar Nacre. *Adv. Mater.*, *28*(38), 8505-8510.
- Guo, X., Wu, Y., & Yan, N. (2018). In situ micro-FTIR observation of molecular association of adsorbed water with heat-treated wood. *Wood Sci. Technol.*
- Gusev, A. A., Zehnder, M. M., & Suter, U. W. (1996). Fluctuation formula for elastic constants. *Phys. Rev. B: Condens. Matter*, *54*(1), 1-4.
- Haghighatpanah, S., & Bolton, K. (2013). Molecular-level computational studies of single wall carbon nanotube-polyethylene composites. *Compos. Mater. Sci.*, *69*, 443-454.
- Harrington, M. J., Masic, A., Holten-Andersen, N., Waite, J. H., & Fratzl, P. (2010). Iron-Clad Fibers: A Metal-Based Biological Strategy for Hard Flexible Coatings. *Science*, *328*(5975), 216-220.
- Hassan, C. M., & Peppas, N. A. (2000). *Structure and Applications of Poly(vinyl alcohol) Hydrogels Produced by Conventional Crosslinking or by Freezing/Thawing Methods*: Springer Berlin Heidelberg.

- Hodge, R., Bastow, T., Edward, G., Simon, G., & Hill, A. (1996). Free volume and the mechanism of plasticization in water-swollen poly (vinyl alcohol). *Macromolecules*, 29(25), 8137-8143.
- Hodge, R., Edward, G. H., & Simon, G. P. (1996). Water absorption and states of water in semicrystalline poly (vinyl alcohol) films. *Polymer*, 37(8), 1371-1376.
- Hodge, R. M., Bastow, T. J., Edward, G. H., Simon, G. P., & Hill, A. J. (1996). Free Volume and the Mechanism of Plasticization in Water-Swollen Poly(vinyl alcohol). *Macromolecules*, 29(25), 8137-8143.
- Holten-Andersen, N., Fantner, G. E., Hohlbauch, S., Waite, J. H., & Zok, F. W. (2007). Protective coatings on extensible biofibres. *Nat. Mater.*, 6(9), 669-672.
- Holten-Andersen, N., Mates, T. E., Toprak, M. S., Stucky, G. D., Zok, F. W., & Waite, J. H. (2009). Metals and the Integrity of a Biological Coating: The Cuticle of Mussel Byssus. *Langmuir*, 25(6), 3323-3326.
- Honegger, E., & Leutwyler, S. (1988). Intramolecular vibrations of small water clusters. *J. Chem. Phys.*, 88(4), 2582-2595.
- Hongbin Li, †, Zhang, W., Weiqing Xu, A., & Zhang, X. (2000). Hydrogen Bonding Governs the Elastic Properties of Poly(vinyl alcohol) in Water: Single-Molecule Force Spectroscopic Studies of PVA by AFM. *Macromolecules*, 33(2), 465-469.
- Howard, S. C., Craig, V. S. J., FitzGerald, P. A., & Wanless, E. J. (2010). Swelling and collapse of an adsorbed pH-responsive film-forming microgel measured by optical reflectometry and QCM. *Langmuir*, 26(18), 14615-14623.
- Huang, B., He, H., Liu, H., Wu, W., Ma, Y., & Zhao, Z. (2019). Mechanically Strong, Heat-Resistant, Water-Induced Shape Memory Poly(vinyl alcohol)/Regenerated Cellulose Biocomposites via a Facile Coprecipitation Method. *Biomacromolecules*, 20(10), 3969-3979.

- Huang, X., Guo, Q., Zhou, P., Lu, C., Yuan, G., Chen, Z., & Zhang, X. (2020). Poly(vinyl alcohol)/artificial marble wastes composites with improved melt processability and mechanical properties. *Composites Part B*, *182*, 107628.
- Ismayil, Ravindrachary, V., Sanjeev, G., & Praveena, S. D. (2018). Electron beam induced modifications in the microstructure of PVA/Li₂B₄O₇ polymer films: Positron annihilation study. *Radiat. Phys. Chem.*
- Jahanshahi, M., Rahimpour, A., & Mortazavian, N. (2012). Preparation, morphology and performance evaluation of polyvinylalcohol (PVA)/polyethersulfone (PES) composite nanofiltration membranes for pulp and paper wastewater treatment. *Iran. Polym. J.*, *21*(6), 375-383.
- Jean, Y. (1990). Positron annihilation spectroscopy for chemical analysis: a novel probe for microstructural analysis of polymers. *Microchem. J.*, *42*(1), 72-102.
- Jeffrey, G. A. (1997). *An introduction to hydrogen bonding*: Oxford University Press.
- Jiang, G., Qiao, J., & Hong, F. (2012). Application of phosphoric acid and phytic acid-doped bacterial cellulose as novel proton-conducting membranes to PEMFC. *Int. J. Hydrogen Energy*, *37*(11), 9182-9192.
- Jose, J., Shehzad, F., & Al-Harathi, M. A. (2014). Preparation method and physical, mechanical, thermal characterization of poly(vinyl alcohol)/poly(acrylic acid) blends. *Polym. Bull.*, *71*(11), 2787-2802.
- Joseph, S., & Aluru, N. R. (2008). Why Are Carbon Nanotubes Fast Transporters of Water? *Nano Lett.*, *8*(2), 452-458.
- Kane, I. A., Clare, M. A., Miramontes, E., Wogelius, R., Rothwell, J. J., Garreau, P., & Pohl, F. (2020). Seafloor microplastic hotspots controlled by deep-sea circulation. *Science*, *368*(6495), 1140-1145.
- Keten, S., & Buehler, M. J. (2009). Asymptotic Strength Limit of Hydrogen Bond Assemblies in Proteins at Vanishing Pulling Rates. *Mrs Proceedings*,

102(12), 198301.

- Keten, S., Xu, Z., Ihle, B., & Buehler, M. J. (1998). *Nanoconfinement controls stiffness, strength and mechanical toughness of β -sheet crystals in silk*. Paper presented at the Scientific Symposium of Research Center for Medical Biotechnology, Copenhagen (Denmark), 20 Aug 1998.
- Keten, S., Xu, Z., Ihle, B., & Buehler, M. J. (2010). Nanoconfinement controls stiffness, strength and mechanical toughness of beta-sheet crystals in silk. *Nat Mater*, 9(4), 359-367.
- Kleinen, J., & Richtering, W. (2011a). Rearrangements in and Release from Responsive Microgel-Polyelectrolyte Complexes Induced by Temperature and Time. *J. Phys. Chem. B*, 115(14), 3804-3810.
- Kleinen, J., & Richtering, W. (2011b). Rearrangements in and Release from Responsive Microgel?Polyelectrolyte Complexes Induced by Temperature and Time. *J. Phys. Chem. B*, 115(14), 3804-3810.
- Konidari, M. V., Soulas, D. N., Papadokostaki, K. G., & Sanopoulou, M. (2012). Study of the effect of modified and pristine carbon nanotubes on the properties of poly(vinyl alcohol) nanocomposite films. *J. Appl. Polym. Sci.*, 125(S1), E471-E477.
- Krishnamoorthy, K., Kim, G.-S., & Kim, S. J. (2013). Graphene nanosheets: Ultrasound assisted synthesis and characterization. *Ultrason. Sonochem.*, 20(2), 644-649.
- Kubo, S., & Kadla, J. F. (2003). The formation of strong intermolecular interactions in immiscible blends of poly(vinyl alcohol) (PVA) and lignin. *Biomacromolecules*, 4(3), 561-567.
- L F, S., Brown, M. G., & Richmond, G. L. (2001). Water at hydrophobic surfaces: weak hydrogen bonding and strong orientation effects. *Science (New York, N.Y.)*, 5518(292), 908-912.
- Lavine, M. S., Waheed, N., & Rutledge, G. C. (2003). Molecular dynamics simulation of orientation and crystallization of polyethylene during

- uniaxial extension. *Polymer*, 44(5), 1771-1779.
- Lee, E. H., Gao, M., Pinotsis, N., Wilmanns, M., & Schulten, K. (2006). Mechanical Strength of the Titin Z1Z2-Telethonin Complex. *Structure (London)*, 14(3), 497-509.
- Lee, S., & Mattice, W. L. (1999). A "phantom bubble" model for the distribution of free volume in polymers. *Comput. Theor. Polym. Sci.*, 9(1), 57-61.
- Lee, S. M., Pippel, E., Gösele, U., Dresbach, C., Qin, Y., Chandran, C. V., . . . Knez, M. (2009). Greatly Increased Toughness of Infiltrated Spider Silk. *Science*, 324, 488-492.
- Lefèvre, T., Rousseau, M.-E., & Pérolet, M. (2007). Protein Secondary Structure and Orientation in Silk as Revealed by Raman Spectromicroscopy. *Biophys. J.*, 92(8), 2885-2895.
- Li, J., Jin, S.-H., Lan, G.-C., Xu, Z.-S., Wang, L.-T., Wang, N., & Li, L.-J. (2019). Research on the Glass Transition Temperature and Mechanical Properties of Poly(vinyl chloride)/Dioctyl Phthalate (PVC/DOP) Blends by Molecular Dynamics Simulations. *Chin. J. Polym. Sci.*, 37(8), 834-840.
- Li, J., Li, Y., Niu, S., Liu, J., & Wang, L. (2017). Synthesis of a new "green" sponge via transesterification of dimethyl carbonate with polyvinyl alcohol and foaming approach. *J. Porous Mater.*, 24(6), 1595-1604.
- Li, J., Li, Y., Song, Y., Niu, S., & Li, N. (2017). Ultrasonic-assisted synthesis of polyvinyl alcohol/phytic acid polymer film and its thermal stability, mechanical properties and surface resistivity. *Ultrason. Sonochem.*, 39, 853-862.
- Li, J., Zhang, P., Chen, L., Li, G., Chen, H., Jia, C., . . . Song, P. (2020). Strong, tough and healable elastomer nanocomposites enabled by a hydrogen-bonded supramolecular network. *Compos. Commun.*, 22, 100530.
- Li, L., Xu, X., Liu, L., Song, P., Cao, Q., Xu, Z., . . . Wang, H. (2021). Water governs the mechanical properties of poly(vinyl alcohol). *Polymer*, 213, 123330.

- Li, Y., & Yao, S. (2017). High stability under extreme condition of the poly(vinyl alcohol) nanofibers crosslinked by glutaraldehyde in organic medium. *Polym. Degrad. Stab.*, *137*, 229-237.
- Ling, Z., Ren, C. E., Zhao, M.-Q., Yang, J., Giammarco, J. M., Qiu, J., . . . Gogotsi, Y. (2014). Flexible and conductive MXene films and nanocomposites with high capacitance. *Proc. Natl. Acad. Sci. U. S. A.*, *111*(47), 16676-16681.
- Liu, H., Chen, F., Liu, B., Estep, G., & Zhang, J. (2010). Super Toughened Poly(lactic acid) Ternary Blends by Simultaneous Dynamic Vulcanization and Interfacial Compatibilization. *Macromolecules*, *43*(14), 6058-6066.
- Liu, T., Peng, X., Chen, Y. N., Bai, Q. W., Shang, C., Zhang, L., & Wang, H. (2018). Hydrogen-Bonded Polymer–Small Molecule Complexes with Tunable Mechanical Properties. *Macromol. Rapid Commun.*, *39*(9), 1800050.
- Lyon, L. A., Meng, Z., Singh, N., Sorrell, C. D., & John, A. S. (2009). Thermoresponsive microgel-based materials. *Chem. Soc. Rev.*, *38*, 865-874.
- Ma, X. F., Xiao, J. J., Yin, K. L., & Xiao, H. M. (2005). Molecular dynamics simulation on mechanical properties of TATB/PCTFE composite material. *Chin. J. Chem. Phys.*, *18*(1), 55-58.
- Marcussvanberg, B. (1997). RESEARCH NOTE An improved leap-frog rotational algorithm. *Mol. Phys.*, *92*(6), 1085-1088.
- Masoomi, M. Y., & Morsali, A. (2012). Applications of metal-organic coordination polymers as precursors for preparation of nano-materials. *Coord. Chem. Rev.*, *256*(23-24), 2921-2943.
- Medhekar, N. V., Ramasubramaniam, A., Ruoff, R. S., & Shenoy, V. B. (2010). Hydrogen Bond Networks in Graphene Oxide Composite Paper: Structure and Mechanical Properties. *ACS Nano*, *4*(4), 2300-2306.
- Monti, F., Fu, S. Y., Iliopoulos, I., & Cloitre, M. (2008). Doubly Responsive Polymer-Microgel Composites: Rheology and Structure. *Langmuir*, *24*(20), 11474-11482.
- Mora-Barrantes, I., Rodríguez, A., Ibarra, L., González, L., & Valentín, J. (2011).

- Overcoming the disadvantages of fumed silica as filler in elastomer composites. *J. Mater. Chem.*, *21*(20), 7381-7392.
- Morimune, S., Kotera, M., Nishino, T., Goto, K., & Hata, K. (2011). Poly(vinyl alcohol) Nanocomposites with Nanodiamond. *Macromolecules*, *44*(11), 4415-4421.
- Müller-Plathe, F. (1998). Diffusion of water in swollen poly(vinyl alcohol) membranes studied by molecular dynamics simulation. *J. Membrane Sci.*, *141*(2), 147-154.
- Müller-Plathe, F. (1998). Microscopic dynamics in water-swollen poly(vinyl alcohol). *J. Chem. Phys.*, *108*(19), 8252-8263.
- Nagel, C., Schmidtke, E., Günther-Schade, K., Hofmann, D., Fritsch, D., Strunskus, T., & Faupel, F. (2000). Free Volume Distributions in Glassy Polymer Membranes: Comparison between Molecular Modeling and Experiments. *Macromolecules*, *33*(6), 2242-2248.
- Ni, F., Wang, G., & Zhao, H. (2018). The effects of urea and caprolactam on the molecular mechanisms and elastic modulus of Polyvinyl alcohol (PVA): a molecular dynamics simulation study. *J. Mech. Behav. Biomed.*, *87*, 10-18.
- Odegard, G. M., Jensen, B. D., Gowtham, S., Wu, J., He, J., & Zhang, Z. (2014). Predicting mechanical response of crosslinked epoxy using ReaxFF. *Chem. Phys. Lett.*, *591*, 175-178.
- Olsen, J. V., Kirkegaard, P., Pedersen, N. J., & Eldrup, M. (2007). PALSfit: A new program for the evaluation of positron lifetime spectra. *Phys. Status Solidi C*, *4*(10), 4004-4006.
- Otsuka, E., & Suzuki, A. (2010). A simple method to obtain a swollen PVA gel crosslinked by hydrogen bonds. *J. Appl. Polym. Sci.*, *114*(1), 10-16.
- Pan, F., Peng, F., & Jiang, Z. (2007). Diffusion behavior of benzene/cyclohexane molecules in poly(vinyl alcohol)-graphite hybrid membranes by molecular dynamics simulation. *Che. Eng. Sci.*, *62*(3), 703-710.
- Paradossi, G., Finelli, I., Natali, F., Telling, M. T. F., & Chiessi, E. (2011). Polymer

- and Water Dynamics in Poly(vinyl alcohol)/Poly(methacrylate) Networks. A Molecular Dynamics Simulation and Incoherent Neutron Scattering Investigation. *Polymers*, 3(4), 1805.
- Park, O.-K., & Lee, J. H. (2018). Carbon nanotube-poly(vinyl alcohol) hybrid aerogels: Improvements in the surface area and structural stability by internal morphology control. *Composites Part B*, 144, 229-236.
- Poly (vinyl alcohol)(pva)-based polymer membranes*. (2009). New York: Nova Science Publishers.
- Porter, D., Vollrath, F., & Shao, Z. (2005). Predicting the mechanical properties of spider silk as a model nanostructured polymer. *European Physical Journal E Soft Matter*, 16(2), 199.
- Potts, J. R., Dreyer, D. R., Bielawski, C. W., & Ruoff, R. S. (2011). Graphene-based polymer nanocomposites. *Polymer*, 52(1), 5-25.
- Prajapati, G. K., Roshan, R., & Gupta, P. N. (2010). Effect of plasticizer on ionic transport and dielectric properties of PVA-H₃PO₄ proton conducting polymeric electrolytes. *J. Phys. Chem. Solids*, 71(12), 1717-1723.
- Priemel, T., Degtyar, E., Dean, M. N., & Harrington, M. J. (2017). Rapid self-assembly of complex biomolecular architectures during mussel byssus biofabrication. *Nat. Commun.*, 8.
- Qiao, B., Zhao, X., Yue, D., Zhang, L., & Wu, S. (2012). A combined experiment and molecular dynamics simulation study of hydrogen bonds and free volume in nitrile-butadiene rubber/hindered phenol damping mixtures. *J. Mater. Chem.*, 22(24), 12339-12348.
- Raheem, M. A., Roy, A. S., & Prasad, M. V. N. A. (2016). Negative thermal coefficient behaviour, dielectric and mechanical properties of poly(vinyl chloride)/poly(vinyl alcohol) blends. *Compos. Commun.*, 1, 38-43.
- Rao, R. V., Rao, P. M., & Shridhar, M. H. (2002). Effect of electron irradiation on P4VP/PTSA complex and P4VP/Phthalocyanine composites. *Nuclear Inst & Methods in Physics Research B*, 187(3), 331-339.

- Rief, & M. (1997). Reversible Unfolding of Individual Titin Immunoglobulin Domains by AFM. *Science*, 276(5315), 1109-1112.
- Ritchie, R. O. (2011). The conflicts between strength and toughness. *Nat. Mater.*, 10(11), 817-822.
- Rosa, A. D. L., Heux, L., Cavaille, J. Y., & Mazeau, K. (2002). Molecular modeling of the mobility of poly(allyl alcohol), PAA, and poly(vinyl alcohol), PVA. *Polymer*, 43(21), 5665-5677.
- Sacristan, B. J., & Mijangos, U. C. (2008). Influence of water content on structure and mobility of polyvinyl alcohol: a molecular dynamics simulation. *J. Chem. Phys.*, 129(15), 245.
- Sakurada, I. (1985). *Chemical Reactions of Polyvinyl Alcohol, International Fiber Science and Technology Series: Polyvinyl Alcohol Fibers*. New York: Marcel Dekker Inc.
- Samotus, B., & Schwimmer, S. (1962). Phytic Acid as a Phosphorus Reservoir in the Developing Potato Tuber. *Nature*, 194(4828), 578-579.
- Shen, X., Cao, L., Liu, Y., Dai, J., Liu, X., Zhu, J., & Du, S. (2018). How Does the Hydrogen Bonding Interaction Influence the Properties of Polybenzoxazine? An Experimental Study Combined with Computer Simulation. *Macromolecules*, 51(13), 4782-4799.
- Shi, L., & Han, Q. (2018). Molecular dynamics study of deformation mechanisms of poly(vinyl alcohol) hydrogel. *Mol. Simulat.*, 44(17), 1363.
- Shokuhi Rad, A., & Ebrahimi, D. (2017). Improving the Mechanical Performance and Thermal Stability of a PVA-Clay Nanocomposite by Electron Beam Irradiation. *Mech. Compos. Mater.*, 53(3), 373-380.
- Simões, M. M. D. S. G., & De Oliveira, M. G. (2010). Poly(vinyl alcohol) films for topical delivery of S -nitrosoglutathione: Effect of freezing–thawing on the diffusion properties. *J. Biomed. Mater. Res. Part B*, 93(2), 416-424.
- Smith, B. J., Swanton, D. J., Pople, J. A., Iii, H. F. S., & Radom, L. (1990). Transition structures for the interchange of hydrogen atoms within the

- water dimer. *J. Chem. Phys.*, 92(2), 1240-1247.
- Solercrespo, R. A., Gao, W., Mao, L., Nguyen, H. T., Roenbeck, M. R., Paci, J. T., . . . Espinosa, H. D. (2018). The Role of Water in Mediating Interfacial Adhesion and Shear Strength in Graphene Oxide. *ACS Nano*.
- Song, P., & Wang, H. (2020). High-Performance Polymeric Materials through Hydrogen-Bond Cross-Linking. *Adv. Mater.*, 32(18), 1901244.
- Song, P. A., Dai, J., Chen, G., Yu, Y., Fang, Z., Lei, W., . . . Chen, Z.-G. (2018). Bioinspired design of strong, tough, and thermally stable polymeric materials via nanoconfinement. *ACS Nano*, 12(9), 9266-9278.
- Song, P. A., & Wang, H. (2020). High-Performance Polymeric Materials through Hydrogen-Bond Cross-Linking. *Adv. Mater.*, 32(18).
- Song, P. A., Xu, Z., Dargusch, M. S., Chen, Z. G., Wang, H., & Guo, Q. (2017). Granular Nanostructure: A Facile Biomimetic Strategy for the Design of Supertough Polymeric Materials with High Ductility and Strength. *Adv. Mater.*, 29(46).
- Song, P. A., Xu, Z., & Guo, Q. (2013). Bioinspired Strategy to Reinforce PVA with Improved Toughness and Thermal Properties via Hydrogen-Bond Self-Assembly. *ACS Macro Lett.*, 2(12), 1100-1104.
- Song, P. A., Xu, Z., Lu, Y., & Guo, Q. (2015a). Bio-Inspired Hydrogen-Bond Cross-Link Strategy toward Strong and Tough Polymeric Materials. *Macromolecules*, 48(12), 3957-3964.
- Song, P. A., Xu, Z., Lu, Y., & Guo, Q. (2015b). Bioinspired strategy for tuning thermal stability of PVA via hydrogen-bond crosslink. *Compos. Sci. Technol.*, 118, 16-22.
- Sperling, L. H. (2005). *Introduction to physical polymer science*: John Wiley & Sons.
- Spreiter, Q., & Walter, M. (1998). Classical Molecular Dynamics Simulation with the Velocity Verlet Algorithm at Strong External Magnetic Fields. *J. Comput. Phys.*, 152(1), 102-119.

- Städler, B., Price, A. D., Chandrawati, R., Hosta-Rigau, L., Zelikin, A. N., & Caruso, F. (2009). Polymer hydrogel capsules: en route toward synthetic cellular systems. *Nanoscale*, *1*(1), 68-73.
- Su, J., Wang, Q., Su, R., Wang, K., Zhang, Q., & Fu, Q. (2008). Enhanced compatibilization and orientation of polyvinyl Alcohol/Gelatin composite fibers using carbon nanotubes. *J. Appl. Polym. Sci.*, *107*(6), 4070-4075.
- SulKowska, J. I., & Cieplak, M. (2007). Mechanical stretching of proteins—a theoretical survey of the Protein Data Bank. *J. Phys.: Condens. Matter*, *19*(28), 283201.
- Sun, H. (1998). COMPASS: An ab Initio Force-Field Optimized for Condensed-Phase Applications Overview with Details on Alkane and Benzene Compounds. *J. Phys. Chem. B*, *102*(38), 7338-7364.
- Sun, Y., & He, C. (2013). Biodegradable "Core-Shell" Rubber Nanoparticles and Their Toughening of Poly(lactides). *Macromolecules*, *46*(24), 9625-9633.
- Tamai, Y., Tanaka, H., & Nakanishi, K. (1996). Molecular dynamics study of polymer-water interaction in hydrogels. 1. Hydrogen-bond structure. *Macromolecules*, *29*(21), 6750-6760.
- Tamai, Y., Tanaka, H., & Nakanishi, K. (1996a). Molecular dynamics study of polymer-water interaction in hydrogels. 1. Hydrogen-bond structure. *Macromolecules*, *29*(21), 6750-6760.
- Tamai, Y., Tanaka, H., & Nakanishi, K. (1996b). Molecular Dynamics Study of Water in Hydrogels. *Mol. Simulat.*, *16*, 359-374.
- Tao, S. (1972). Positronium annihilation in molecular substances. *J. Chem. Phys.*, *56*(11), 5499-5510.
- Tasaki, K. (1996). Poly (oxyethylene)- water interactions: a molecular dynamics study. *J. Am. Chem. Soc.*, *118*(35), 8459-8469.
- Tesei, G., Paradossi, G., & Chiessi, E. (2012). Poly(vinyl alcohol) oligomer in dilute aqueous solution: a comparative molecular dynamics simulation study. *J. Phys. Chem. B*, *116*(33), 10008-10019.

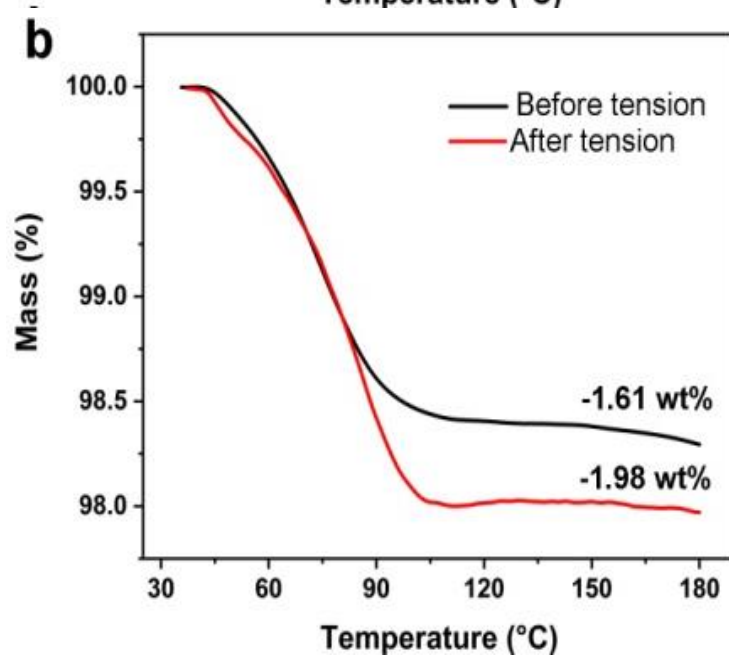
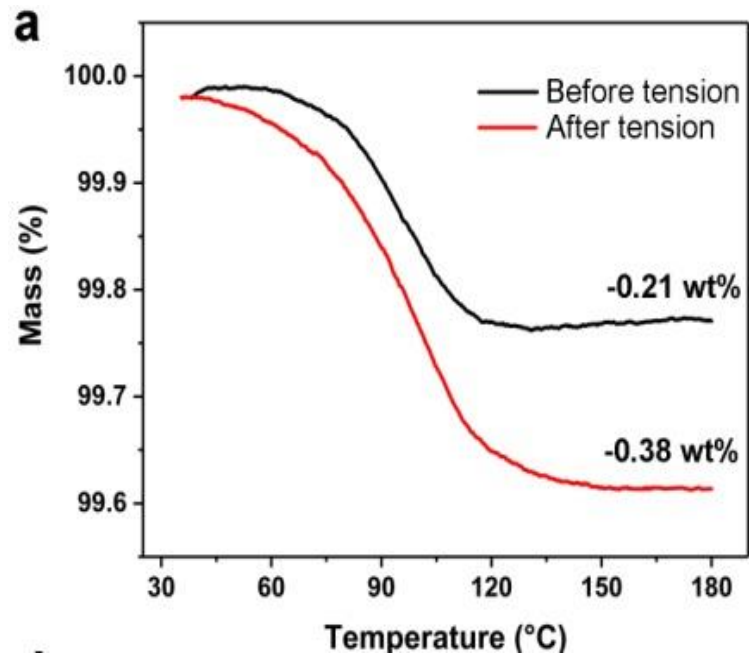
- Theodorou, D. N., & Suter, U. W. (1986). Atomistic Modeling of Mechanical Properties of Polymeric Glasses. *Macromolecules*, 19(1), 139-154.
- Tudorachi, N., Cascaval, C. N., Rusu, M., & Pruteanu, M. (2000). Testing of polyvinyl alcohol and starch mixtures as biodegradable polymeric materials. *Polym. Test.*, 19(7), 785-799.
- Verlet, L. (1967). Computer "Experiments" on Classical Fluids. I. Thermodynamical Properties of Lennard-Jones Molecules. *Health Phys.*, 22(1), 79-85.
- Voronova, M. I., Surov, O. V., Guseinov, S. S., & Zakharov, A. G. (2016). Thermal stability of composites of polyvinyl alcohol with nanocrystalline cellulose in its acid and neutralized forms. *Compos. Commun.*, 2, 15-18.
- Wan, S., Peng, J., Li, Y., Hu, H., Jiang, L., & Cheng, Q. (2015). Use of Synergistic Interactions to Fabricate Strong, Tough, and Conductive Artificial Nacre Based on Graphene Oxide and Chitosan. *ACS Nano.*, 9(10), 9830-9836.
- Wang, J., Cheng, Q., Lin, L., Chen, L., & Jiang, L. (2013). Understanding the relationship of performance with nanofiller content in the biomimetic layered nanocomposites. *Nanoscale*, 5, 6356-6362.
- Wang, Y., Nakanishi, H., Jean, Y., & Sandreczki, T. (1990). Positron annihilation in amine-cured epoxy polymers—pressure dependence. *J. Polym. Sci., Part B: Polym. Phys.*, 28(9), 1431-1441.
- Wei, Q., Zhang, Y., Wang, Y., & Yang, M. (2017). A molecular dynamic simulation method to elucidate the interaction mechanism of nano-SiO₂ in polymer blends. *J. Mater. Sci.*, 52(21), 12889-12901.
- Wolf, R. M., & Suter, U. W. (1984). Conformational characteristics of poly(vinyl alcohol). *Macromolecules*, 17(4), 669-677.
- Wu, C. (2010). Cooperative behavior of poly(vinyl alcohol) and water as revealed by molecular dynamics simulations. *Polymer*, 51(19), 4452-4460.
- Wu, C., & Xu, W. (2007). Atomistic simulation study of absorbed water influence on structure and properties of crosslinked epoxy resin. *Polymer*, 48(18),

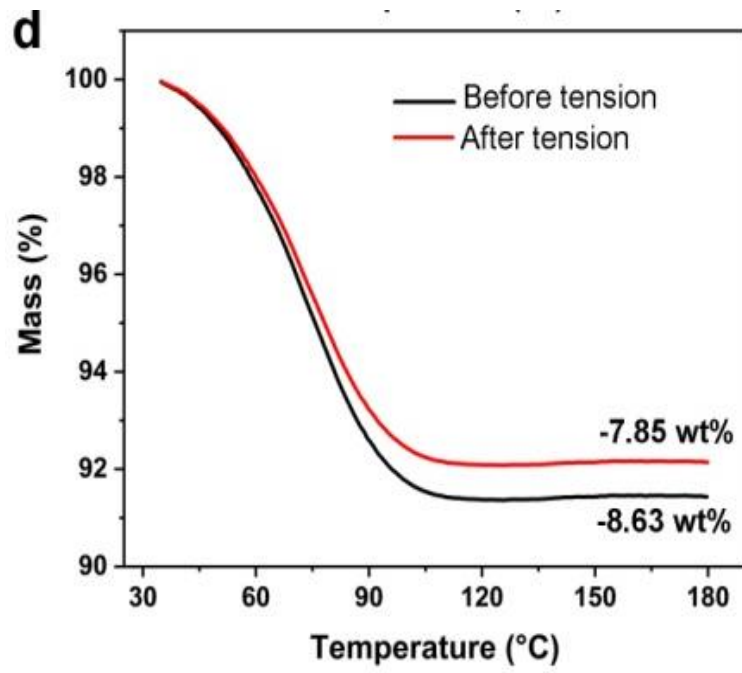
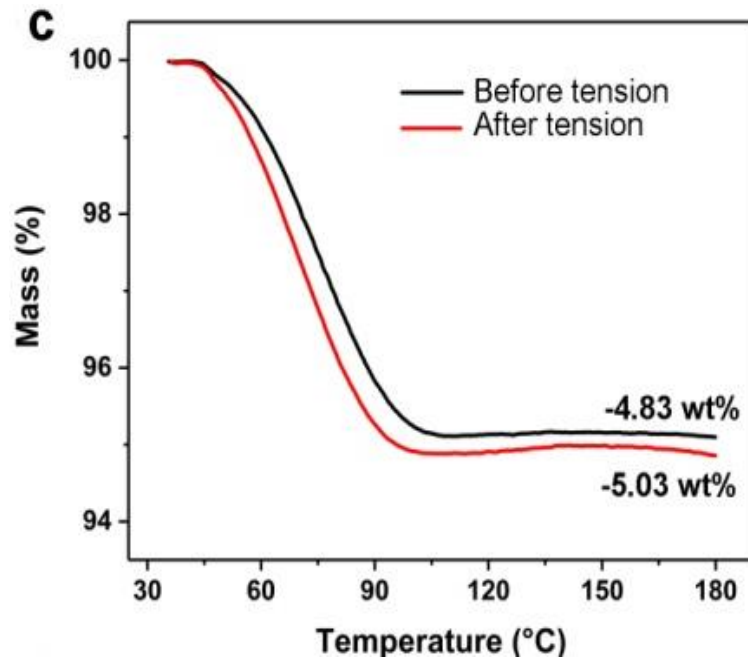
5440-5448.

- Wu, H., Yu, G., Pan, L., Liu, N., McDowell, M. T., Bao, Z., & Cui, Y. (2013). Stable Li-ion battery anodes by in-situ polymerization of conducting hydrogel to conformally coat silicon nanoparticles. *Nat. Commun.*, *4*.
- Wu, S., Guo, Q., Kraska, M., Stuehn, B., & Mai, Y.-W. (2013). Toughening Epoxy Thermosets with Block Ionomers: The Role of Phase Domain Size. *Macromolecules*, *46*(20), 8190-8202.
- Wu, W., Tian, H., & Xiang, A. (2012). Influence of Polyol Plasticizers on the Properties of Polyvinyl Alcohol Films Fabricated by Melt Processing. *J Polym Environ*, *20*(1), 63-69.
- Xiang, Y. Z., Yao, F. C., Jia, D. M., & Dong, X. (2009). Effect of a Complex Plasticizer on the Structure and Properties of the Thermoplastic PVA/Starch Blends. *Polym. Plast. Technol. Eng.*, *48*(5), 489-495.
- Xie, Q., Fu, K., Liang, S., Liu, B., Lu, L., Yang, X., . . . Lü, F. (2018). Microstructure and thermomechanical properties of crosslinked epoxy composite modified by nano-SiO₂: A molecular dynamics simulation. *Polymers*, *10*(7), 801.
- Yang, W., He, X., Luzi, F., Dong, W., Zheng, T., Kenny, J. M., . . . Ma, P. (2020). Thermomechanical, antioxidant and moisture behaviour of PVA films in presence of citric acid esterified cellulose nanocrystals. *Int. J. Biol. Macromol.*, *161*, 617-626.
- Yao, L., Haas, T. W., Guiseppi-Elie, A., Bowlin, G. L., Simpson, D. G., & Wnek, G. E. (2003). Electrospinning and Stabilization of Fully Hydrolyzed Poly(Vinyl Alcohol) Fibers. *Chem. Mater.*, *15*(9), 1860-1864.
- Yao, X., Shamsaei, E., Chen, S., Zhang, Q. H., de Souza, F. B., Sagoe-Crentsil, K., & Duan, W. (2019). Graphene oxide-coated Poly(vinyl alcohol) fibers for enhanced fiber-reinforced cementitious composites. *Composites Part B*, *174*, 107010.
- Yin, Y., Li, J., Liu, Y., & Li, Z. (2010). Starch crosslinked with poly(vinyl alcohol)

- by boric acid. *J. Appl. Polym. Sci.*, 96(4), 1394-1397.
- Zelikin, A. N., Price, A. D., & Stadler, B. (2010). Poly(Methacrylic Acid) Polymer Hydrogel Capsules: Drug Carriers, Sub-compartmentalized Microreactors, Artificial Organelles. *Small*, 6(20), 2201-2207.
- Zhang, X., Liu, T., Sreekumar, T., Kumar, S., Moore, V. C., Hauge, R. H., & Smalley, R. E. (2003). Poly (vinyl alcohol)/SWNT composite film. *Nano Lett.*, 3(9), 1285-1288.
- Zhang, X., Liu, W., Yang, D., & Qiu, X. (2019). Biomimetic Supertough and Strong Biodegradable Polymeric Materials with Improved Thermal Properties and Excellent UV-Blocking Performance. *Adv. Funct. Mater.*, 29(4), 1806912.
- Zhao, W., Li, M., Fang, T., Yu, Y., Su, Y., & Deng, W. (2016). The molecular simulation of the miscibility, mechanical properties and physical cross-linking behavior of the poly(vinyl alcohol)/poly(acrylic acid) composited membranes. *Mol. Simulat.*, 42(11), 927-935.
- Zhao, X., Zhang, Q. H., Chen, D. J., & Lu, P. (2011). Enhanced Mechanical Properties of Graphene-Based Poly(vinyl alcohol) Composites (vol 43, pg 2357, 2010). *Macromolecules*, 44(7), 2392-2392.
- Zhou, Q., Zhao, Y., Dang, H., Tang, Y., & Zhang, B. (2019). Antibacterial Effects of Phytic Acid against Foodborne Pathogens and Investigation of Its Mode of Action. *J. Food Prot.*, 82(5), 826-833.
- Zhou, Y., Ding, C., Qian, X., & Ankey, X. (2015). Further improvement of flame retardancy of polyaniline-deposited paper composite through using phytic acid as dopant or co-dopant. *Carbohydr. Polym.*, 115, 670-676.
- Zidan, H. M. (2003). Structural properties of CrF₃- and MnCl₂-filled poly(vinyl alcohol) films. *J. Appl. Polym. Sci.*, 88(5), 1115-1120.
- Zidan, H. M., Abdelrazek, E. M., Abdelghany, A. M., & Tarabiah, A. E. (2018). Characterization and some physical studies of PVA/PVP filled with MWCNTs. *J. Mater. Res. Technol.*

APPENDIX A





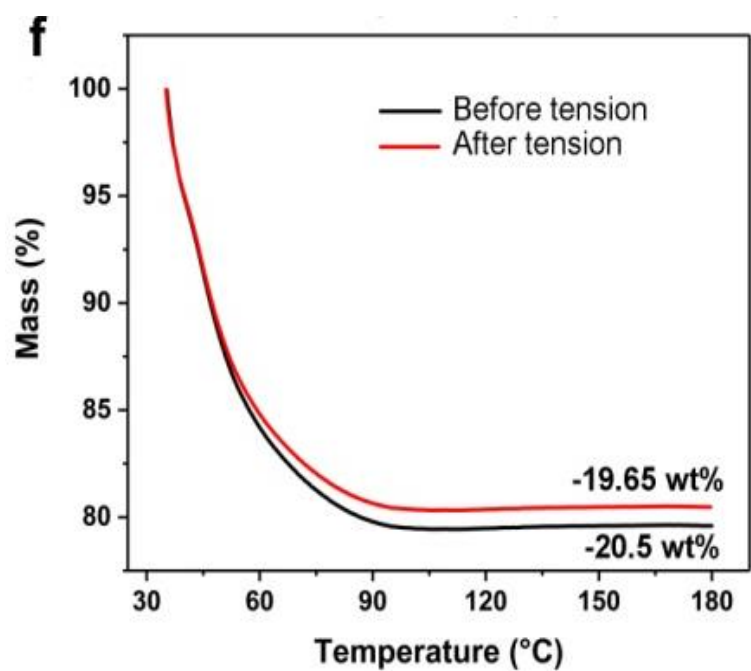
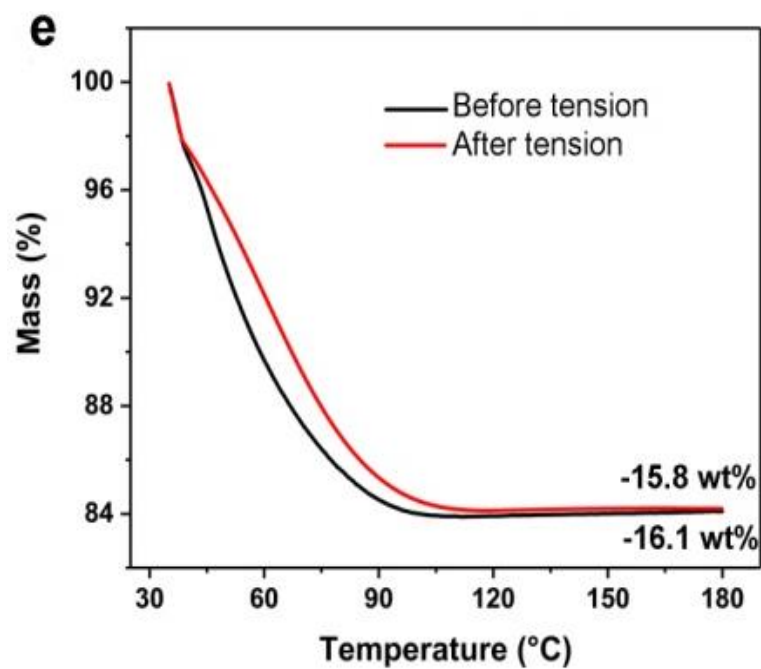


Figure AS1 TGA curves for as-prepared PVA films before and after tensile tests. The water content were calculated by the average value of the weight loss during two tests.

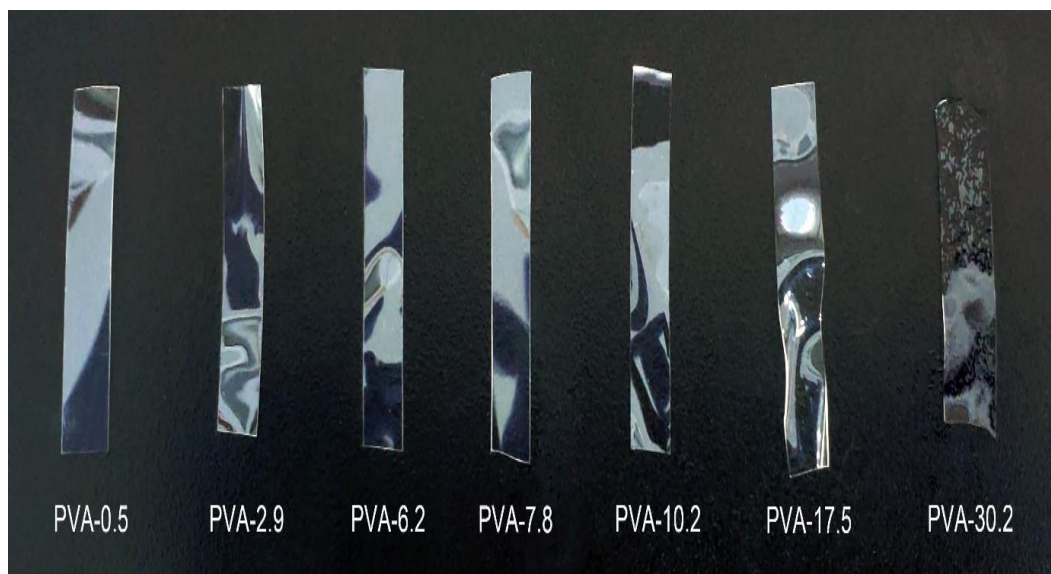


Figure AS2 Digital graphs of PVA with varied water content, showing the hydration of PVA.

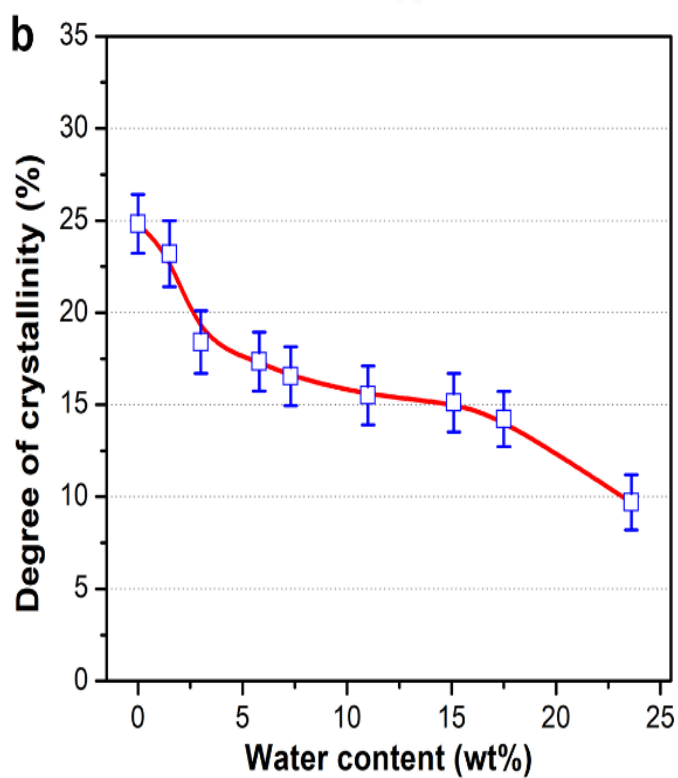
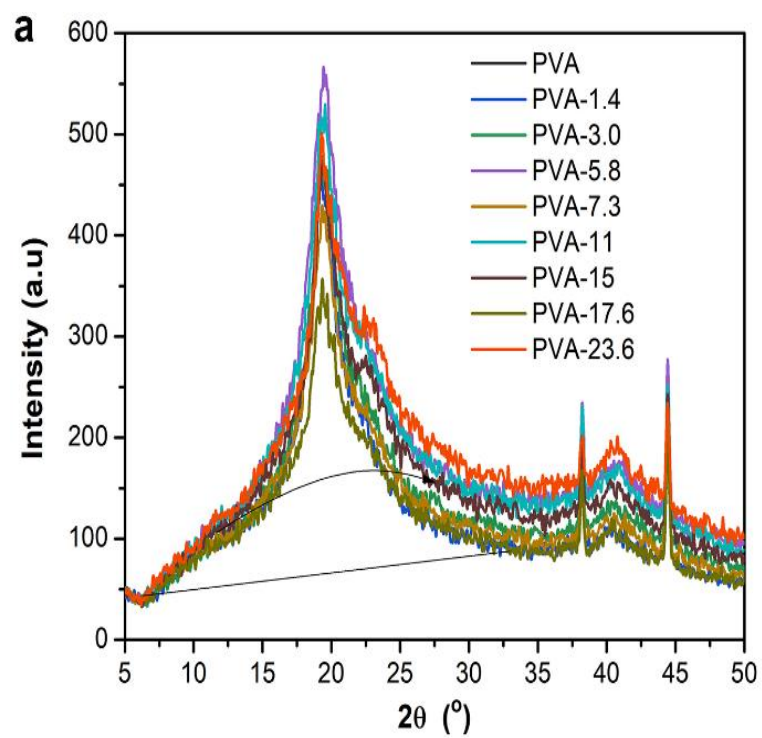


Figure AS3 a) XRD diffraction patterns and b) degree of crystallinity for PVA films with varied water content.

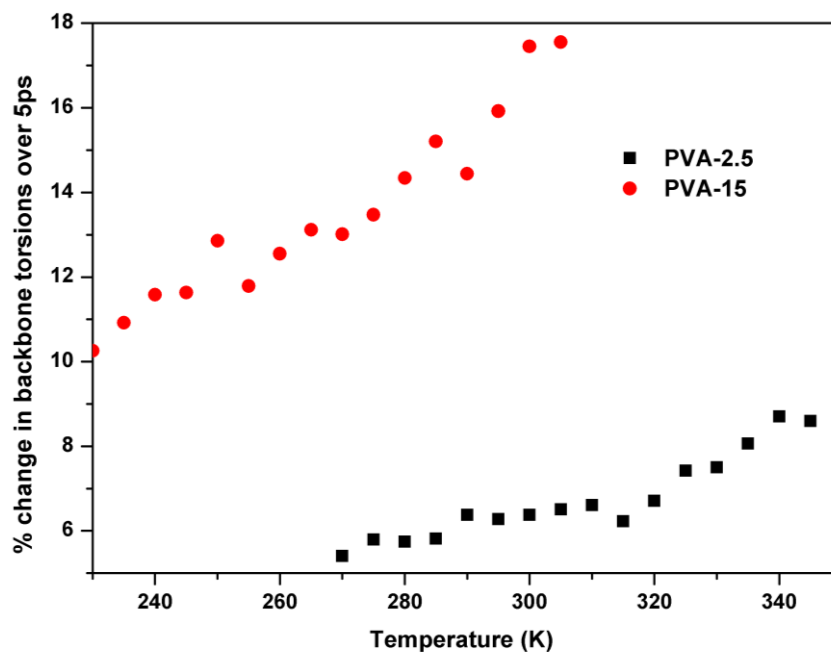
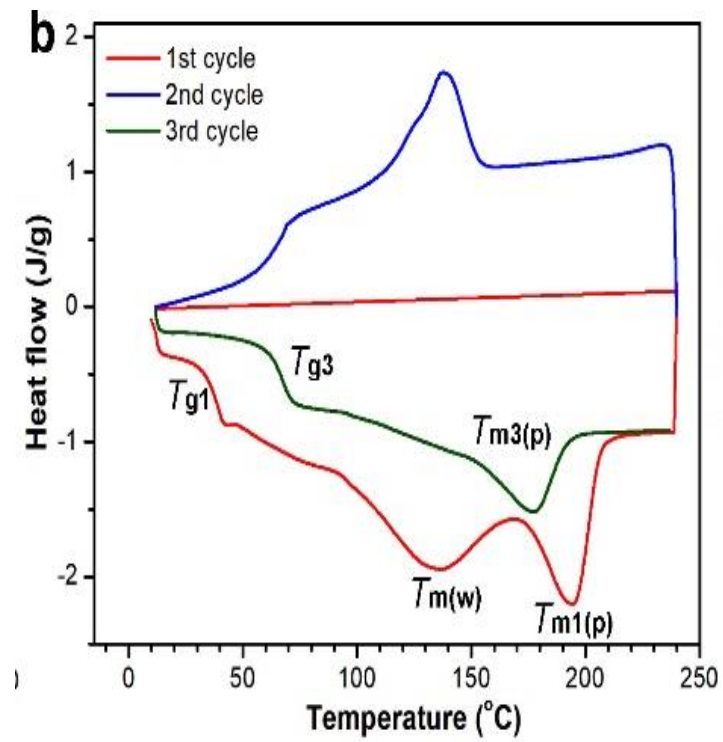
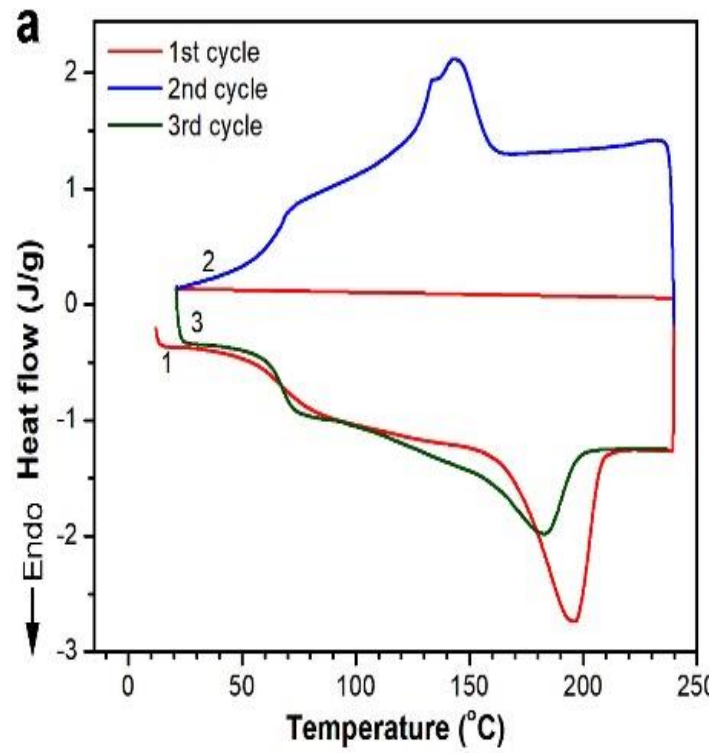
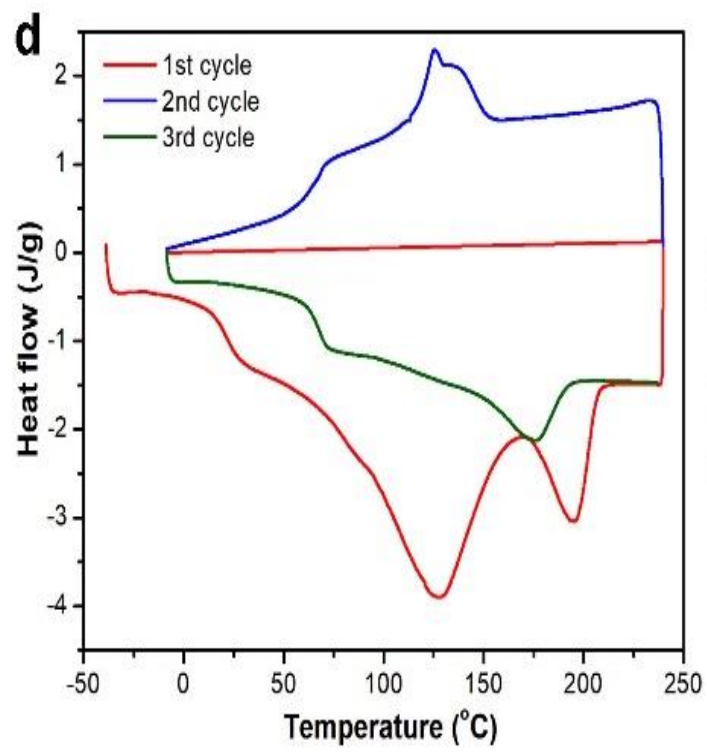
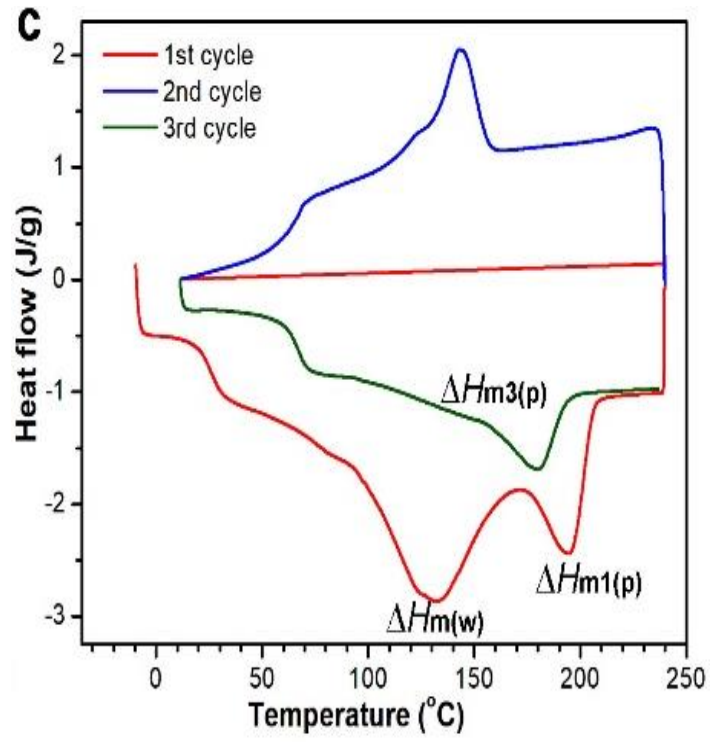


Figure AS4 Torsion changes of backbone as a function of temperature for 2.5% and 15% water content.





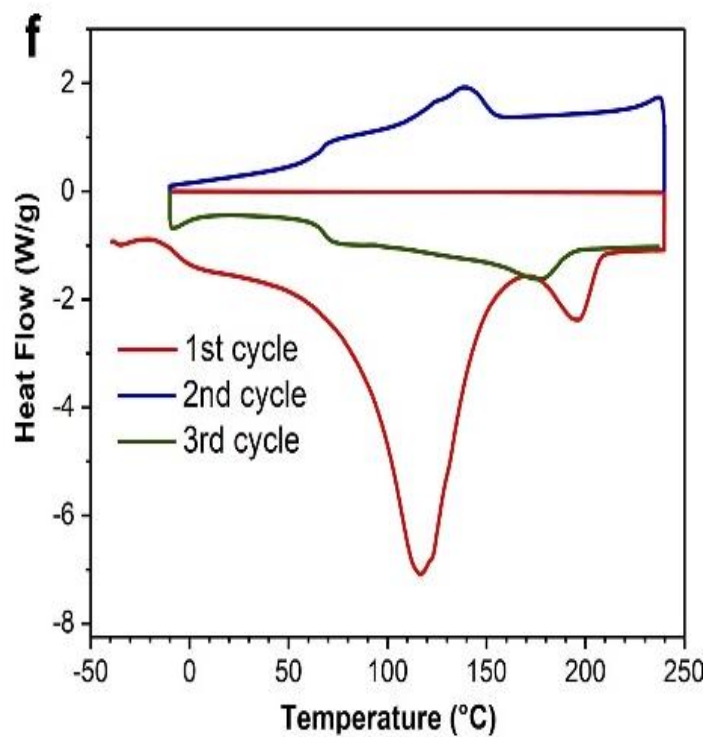
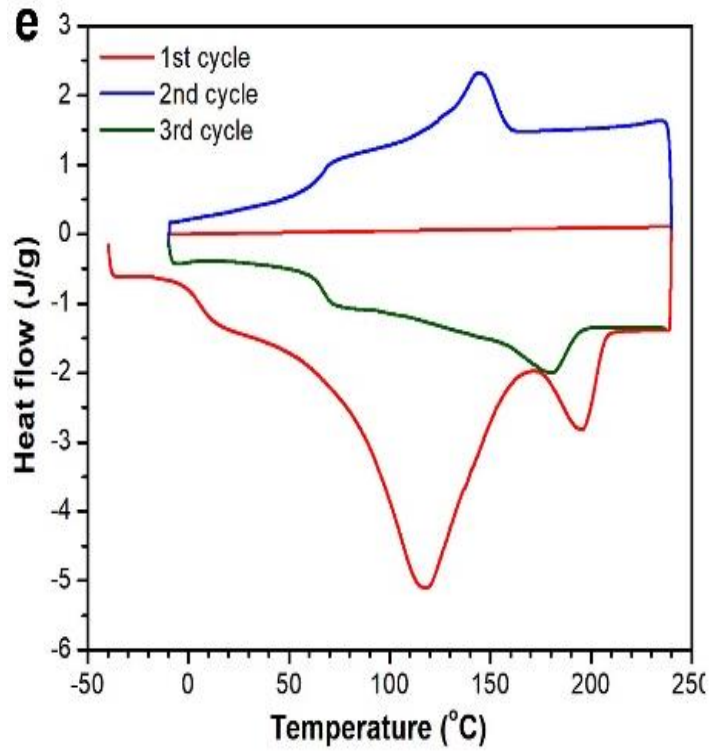
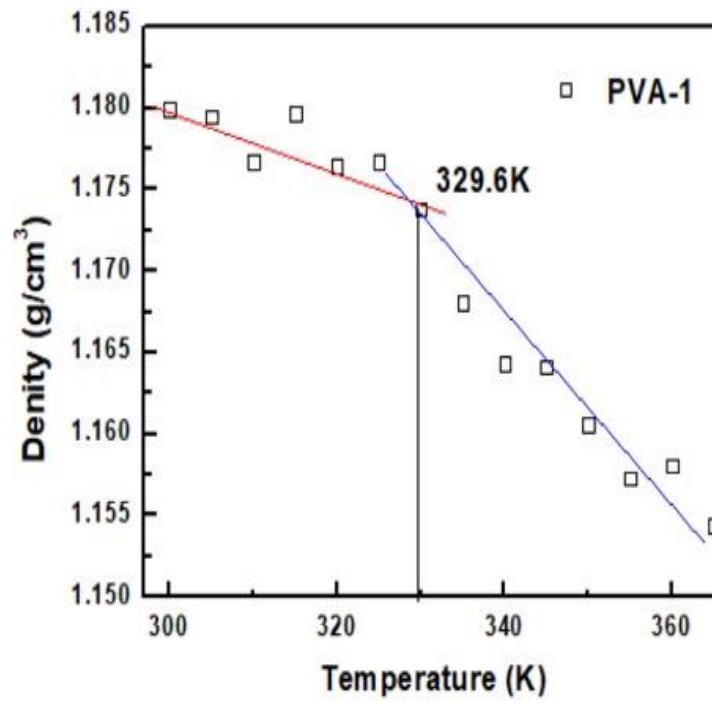
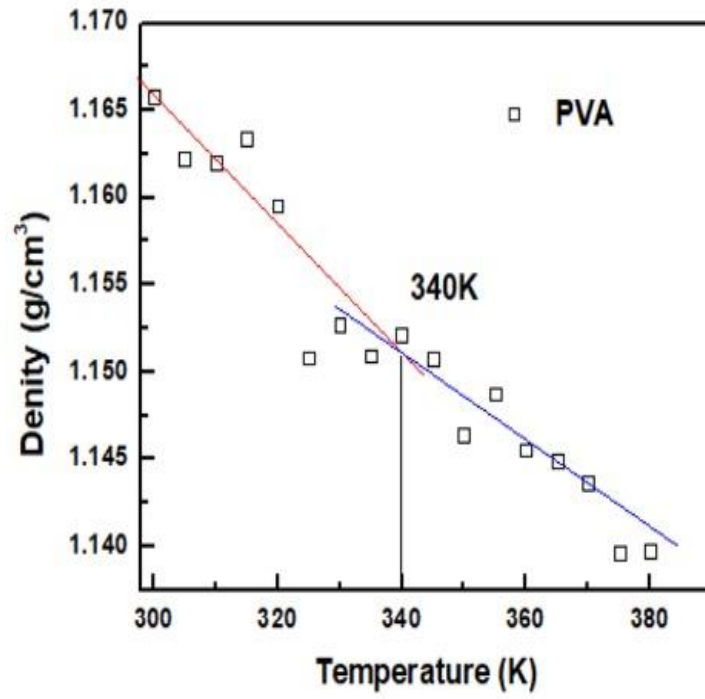


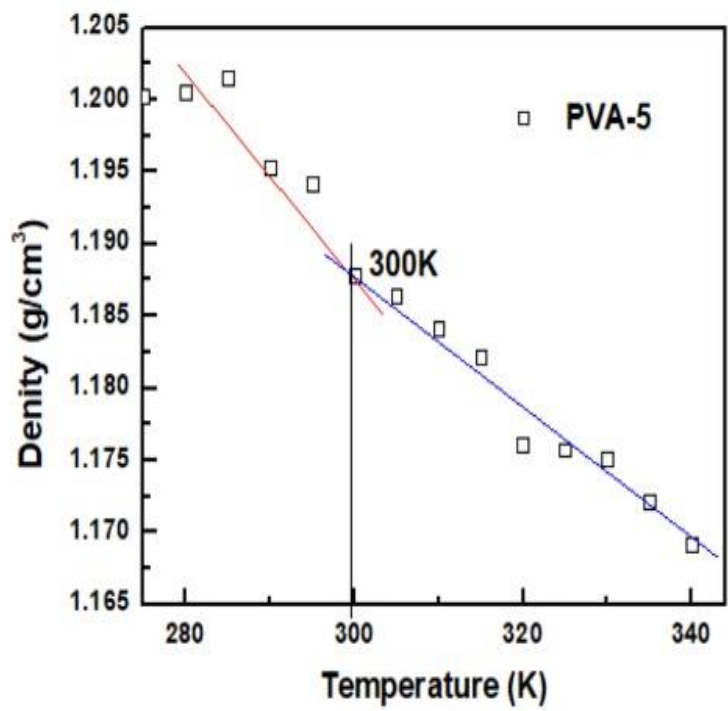
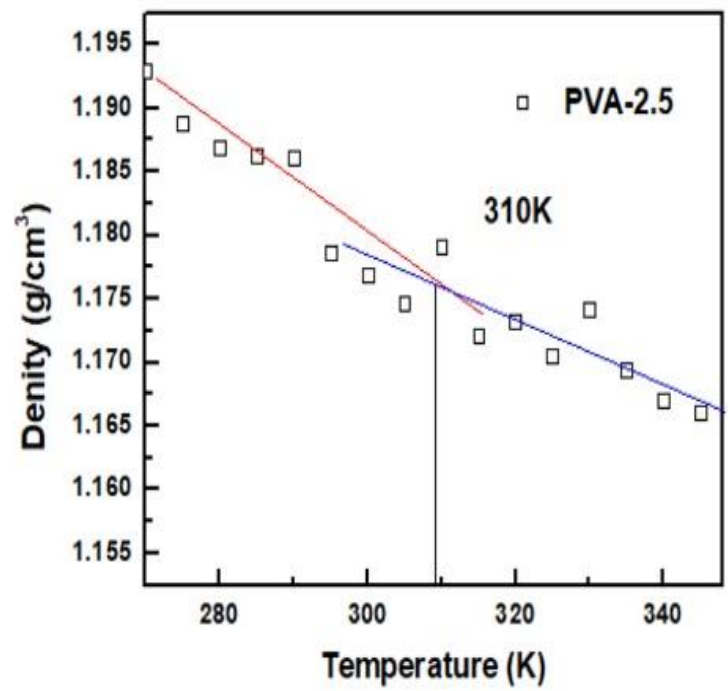
Figure AS5 DSC traces for a) PVA, b) PVA-1.8-, c) PVA-4.9, d) PVA-8.2, e) PVA-16 and f) PVA-20.

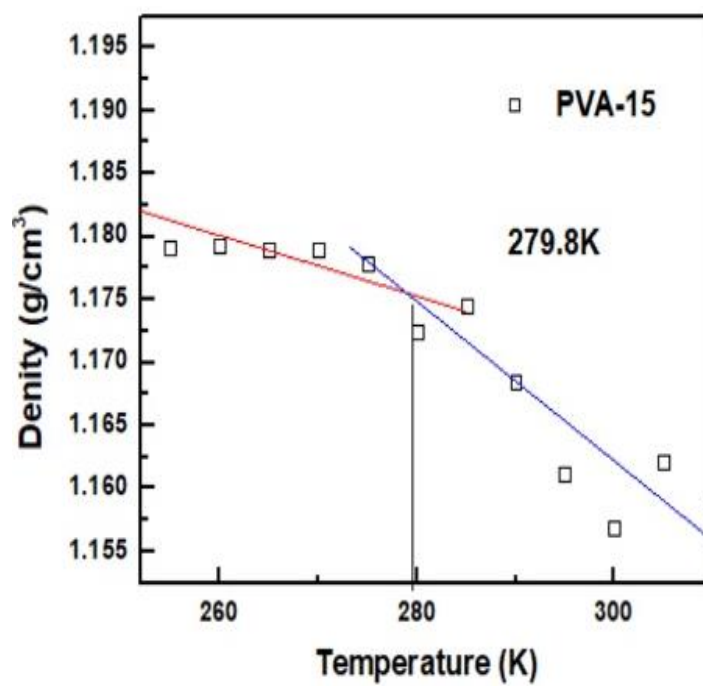
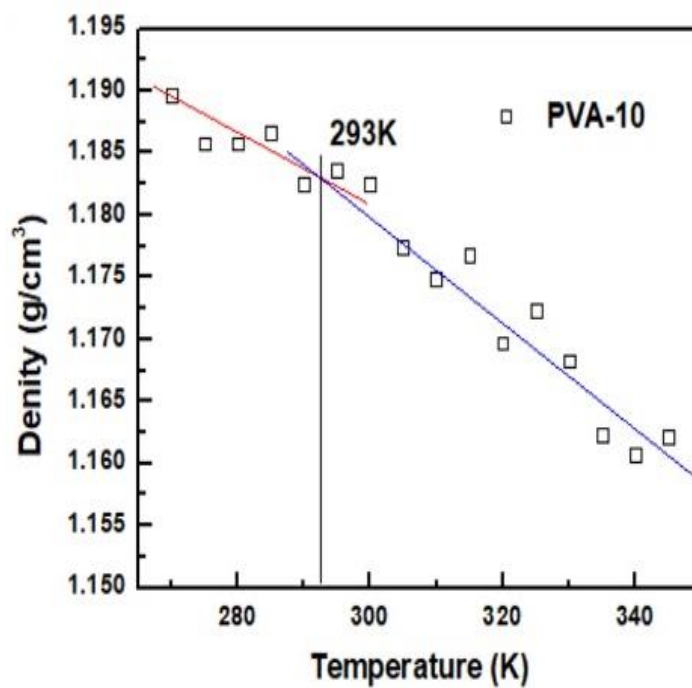
Table AS1 Detailed thermal properties data for PVA with varied water content obtained from DSC measurements.

Run	$T_{g(p)1}$ (°C)	$T_{m(w)}$ (°C)	$\Delta H_{m(w)}$ (J/g)	$T_{m(p)1}$ (°C)	$\Delta H_{m(p)1}$ (J/g)	χ_{c1} (%)	$T_{g(p)3}$ (°C)	$T_{m(p)3}$ (°C)	$\Delta H_{m(p)3}$ (J/g)	χ_{c3} (%)
PVA	66.8	-		196.0	33.2	24.0	67.4	182.8	22.7	16.4
PVA-1.8	38.132	136.1	23.6	194.8	21.5	15.5	67.0	177.2	21.9	15.8
PVA-2.8	32.9	134.5	33.5	194.9	20.1	14.5	67.4	178.3	21.3	15.4
PVA-4.9	25.2	132.0	54.0	194.7	19.3	13.9	66.9	180.0	21.2	15.3
PVA-6.5	22.3	28.2	4.4	93.3	19.3	3.9	66.7	77.5	2.6	15.6
PVA-8.2	20.4	127.6	90.6	195.3	21.3	15.4	66.7	76.4	18.3	13.2
PVA-16	4.60	117.8	161.1	195.4	20.4	14.7	66.6	180.2	19.3	13.9
PVA-20	-8.00	116.0	247.8	195.3	19.9	14.4	67.0	176.5	19.5	14.1

$T_{g(p)1}$ and $T_{g(p)3}$ refer to the T_g values of the PVA matrix obtained from the first and third cycles of DSC measurements, respectively; $\Delta H_{m(w)}$ is the melt enthalpy of water in the PVA; $T_{m(p)1}$ and $T_{m(p)3}$ are respectively the melting points of PVA obtained from the first and third cycles of DSC measurements; χ_{c1} and χ_{c3} , $\Delta H_{m(p)1}$ and $\Delta H_{m(p)3}$ refer to the melting enthalpy of PVA obtained from the first and third cycles of DSC measurements, respectively. The melting enthalpy (ΔH_f^0) of 100 % crystalline PVA was taken as 138.6 J/g (Su et al., 2008).







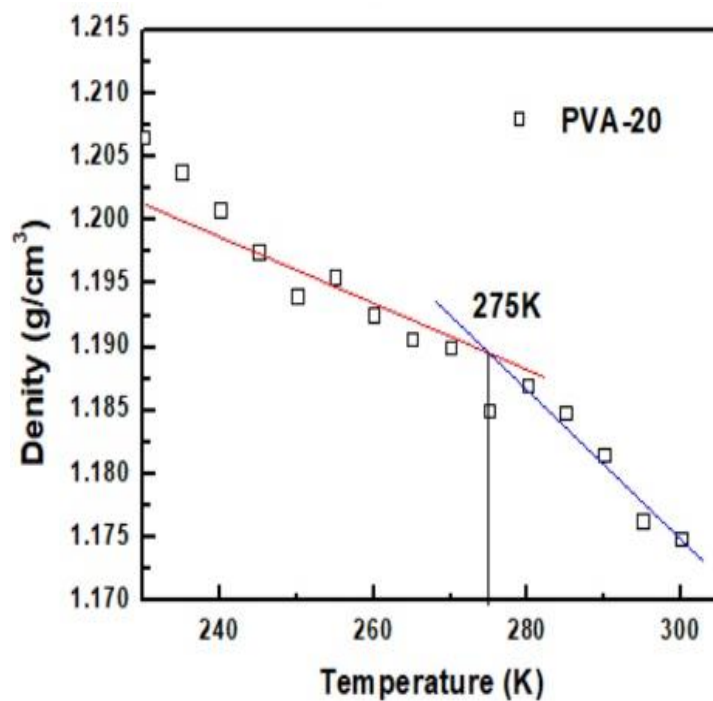


Figure AS6 The calculation of glass transition temperature (T_g) for PVA with varied water content by MD simulation.

Table AS2. T_g and FFV values for PVA with various water content calculated by the Gordon-Taylor equation (theoretical value) and MD simulation (simulated) as well as experimental values.

Run	T_g (K)		FFV (%)				
	Theoretical	Simulated	Simulated	Theoretical by the Fox-Flory theory	Experimental by PALS		
PVA	358	360	4.72	PVA	2.5	PVA	2.74
PVA-1.0	352	356	3.84	PVA-1.0	2.5	PVA-1.0	2.76
PVA-2.5	344	342	3.10	PVA-3	2.5	PVA-3	2.47
PVA-5.0	331	334	3.32	PVA-4.5	2.52	PVA-4.5	2.50
PVA-10	307	311	2.68	PVA-6	2.64	PVA-6	2.65
PVA-15	287	293	2.93	PVA-8	2.76	PVA-8	2.87
PVA-20	269	286	3.15	PVA-14	3.32	PVA-14	3.63
PVA-30			3.67	PVA-20	4.13		

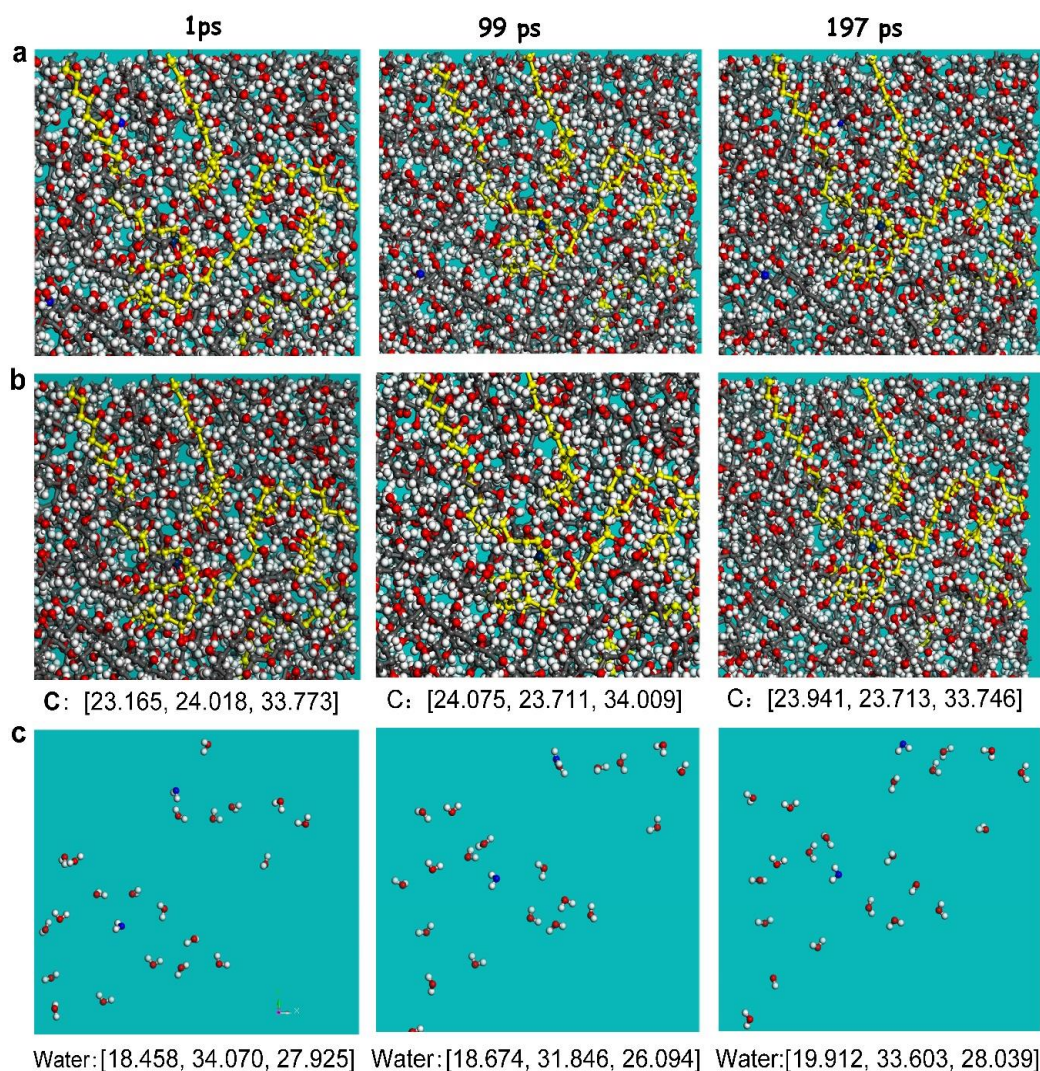


Figure AS7 Snapshots of MD simulation showing the moving trails for a) PVA-1.0, b) extracted PVA chains and c) extracted water molecules after 1ps, 99 ps and 197 ps. The main chain of one chosen PVA is marked in yellow with one carbon atom highlighted in dark blue for showing the movement of PVA chains. Two water molecules are marked in blue for monitoring their movement with time.

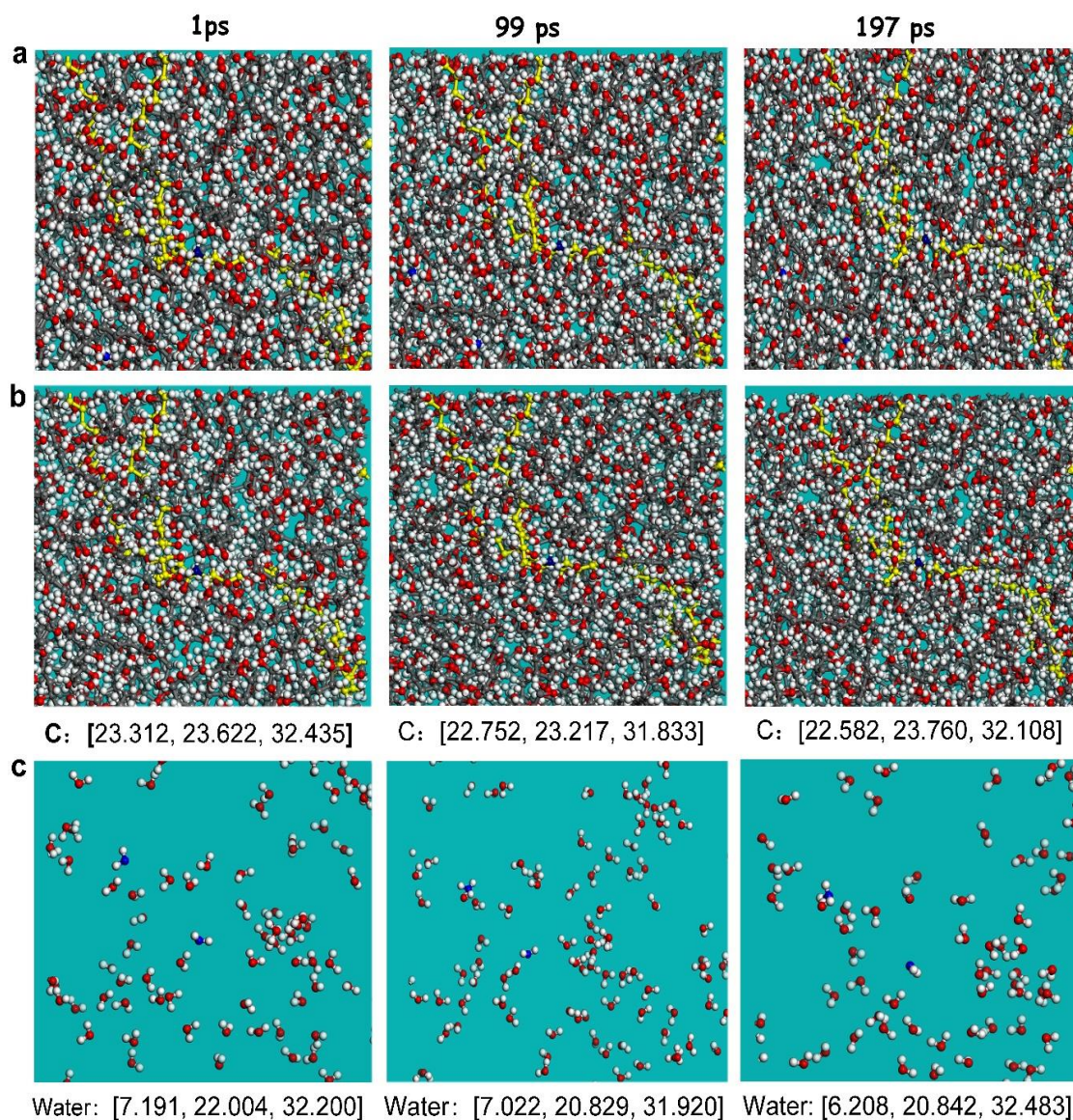


Figure AS8 Snapshots of MD simulation showing the moving trails for a) PVA-5.0, b) extracted PVA chains and c) extracted water molecules after 1ps, 99 ps and 197 ps. The main chain of one chosen PVA is marked in yellow with one carbon atom highlighted in dark blue for showing the movement of PVA chains. Two water molecules are marked in blue for monitoring their movement with time.

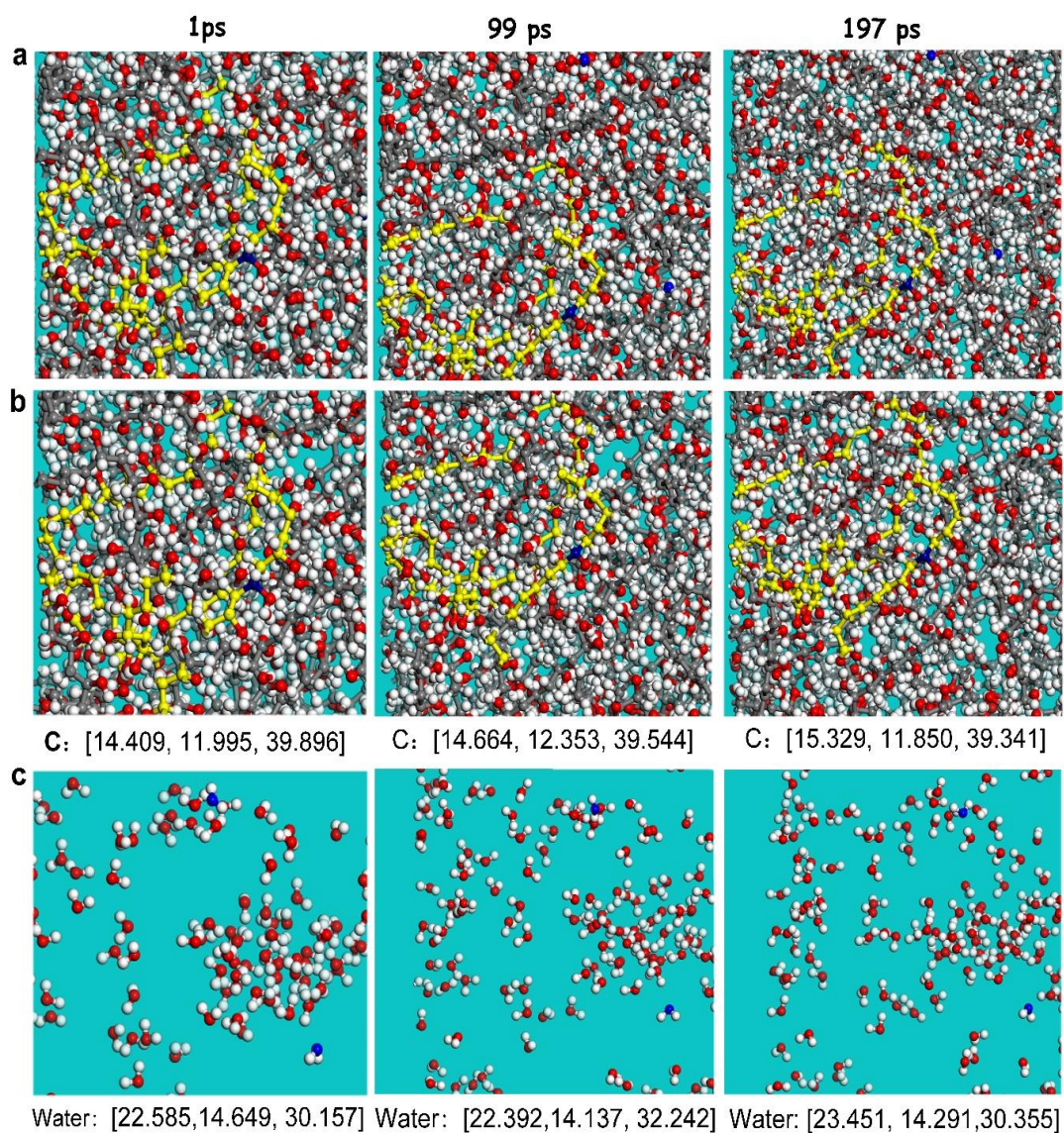


Figure AS9 Snapshots of MD simulation showing the moving trails for a) PVA-10, b) extracted PVA chains and c) extracted water molecules after 1, 99 and 197 ps. The main chain of one chosen PVA is marked in yellow with one carbon atom highlighted in dark blue for showing the movement of PVA chains. Two water molecules are marked in blue for monitoring their movement.

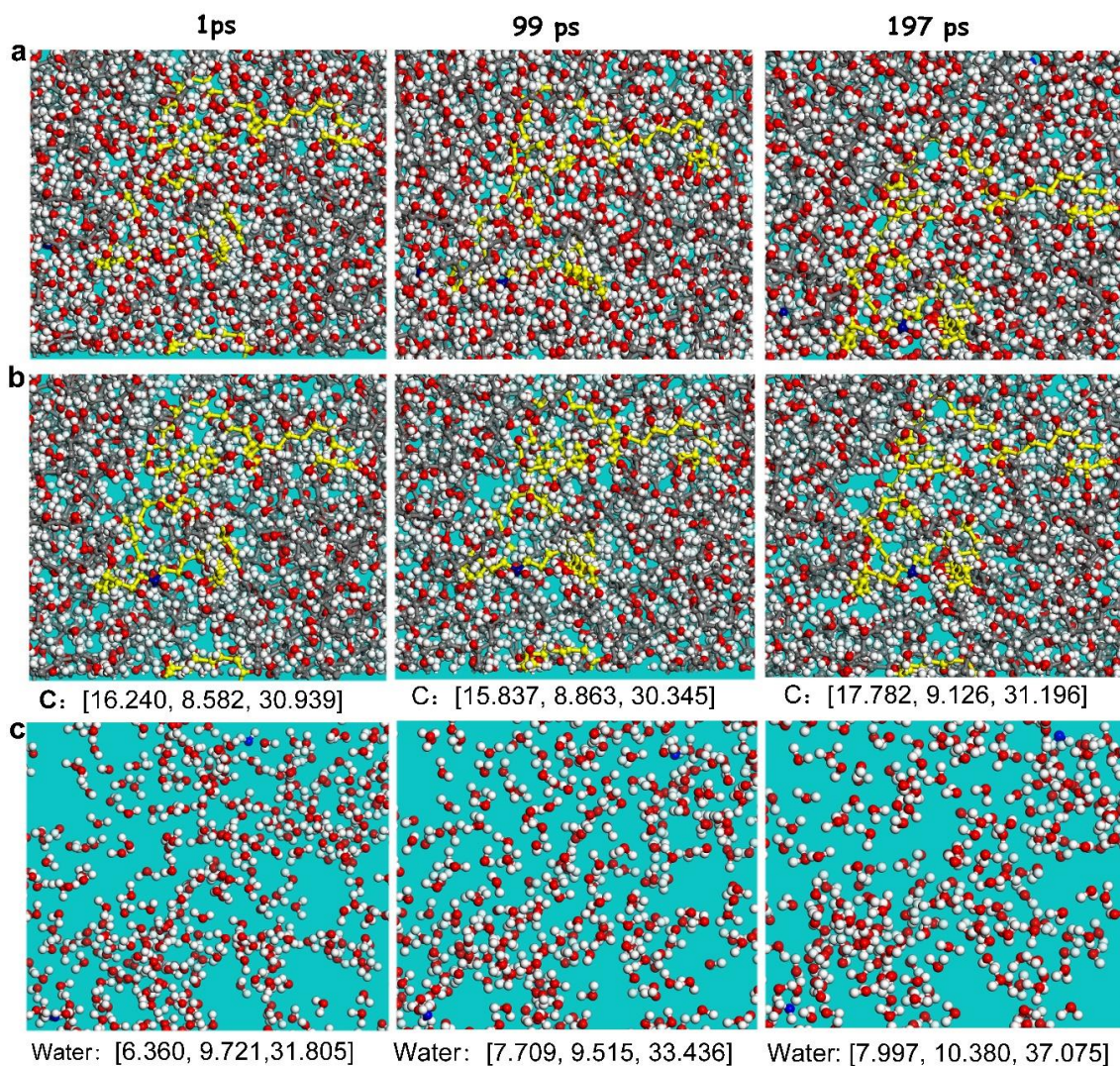
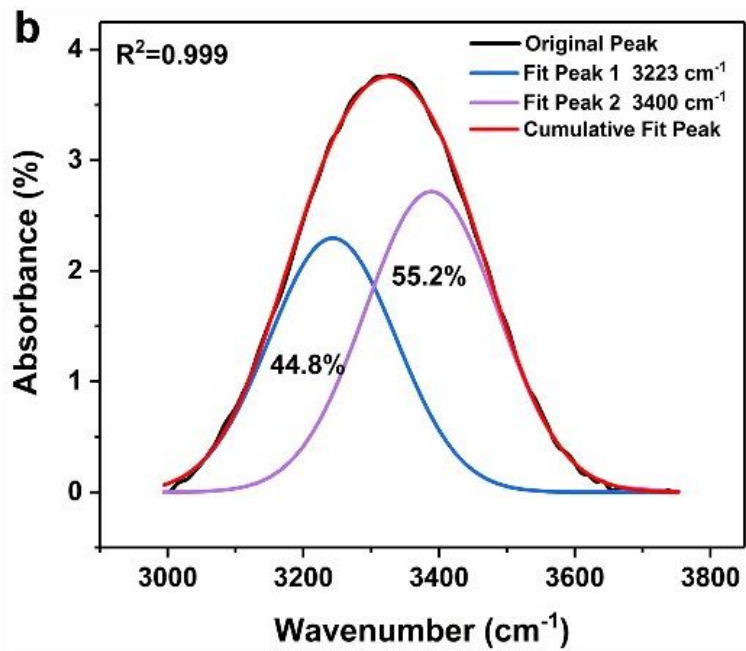
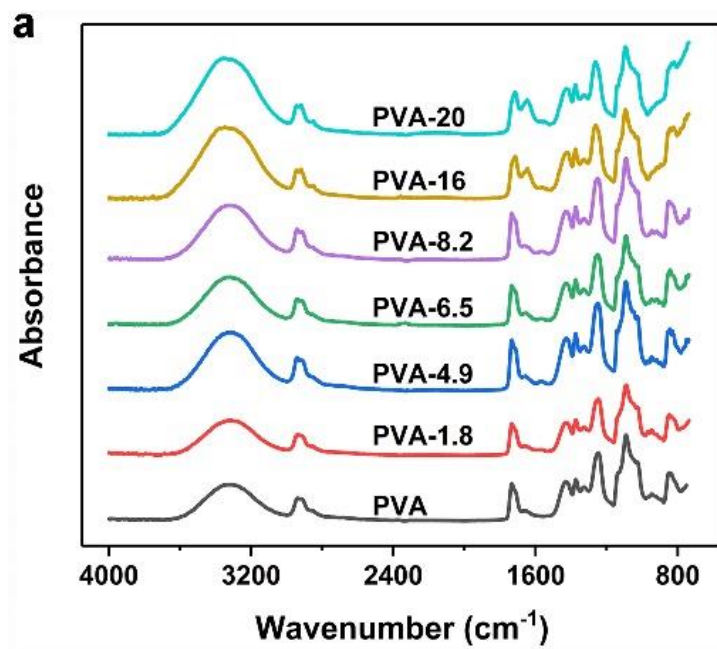
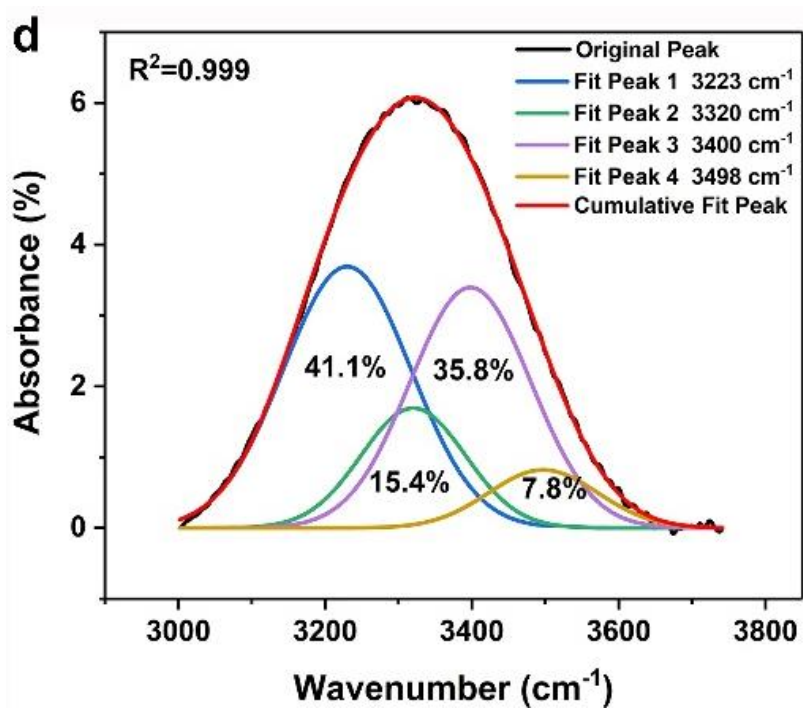
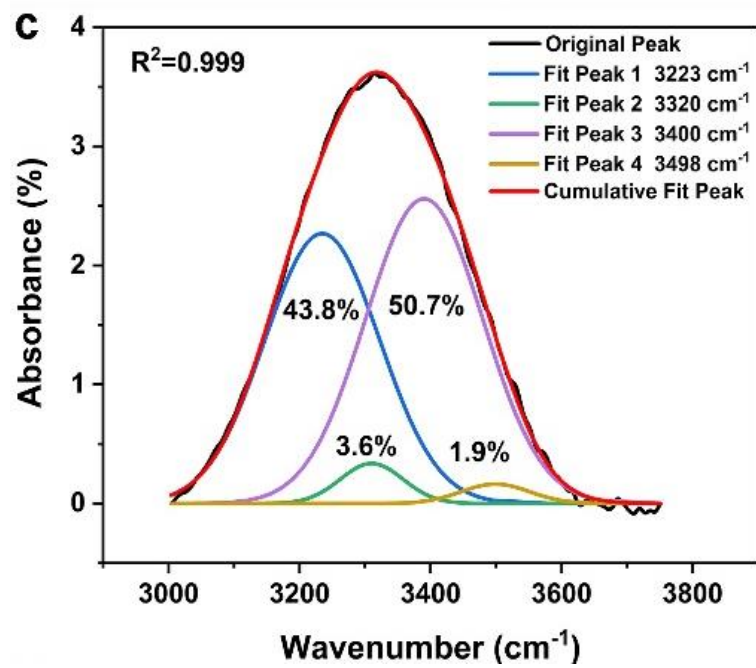
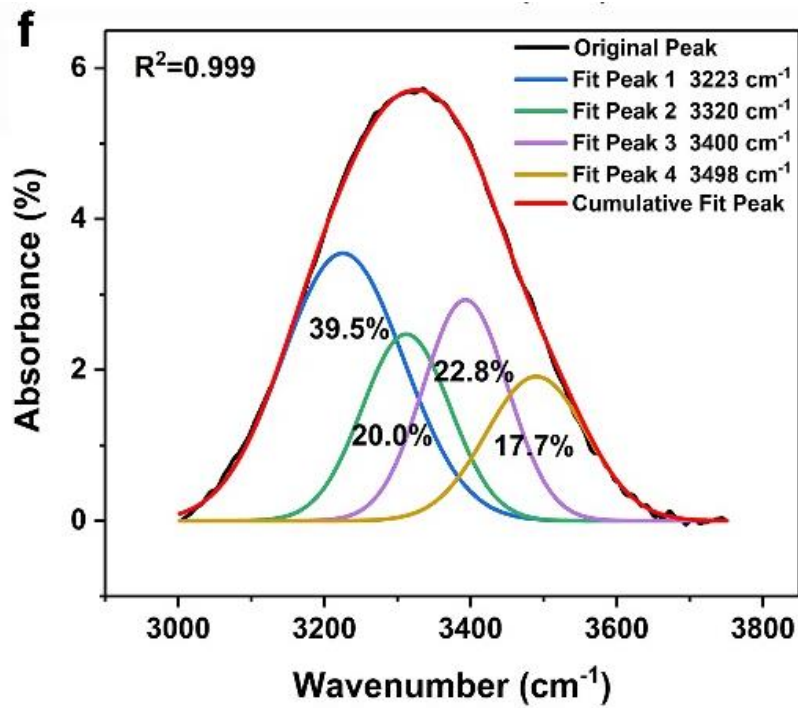
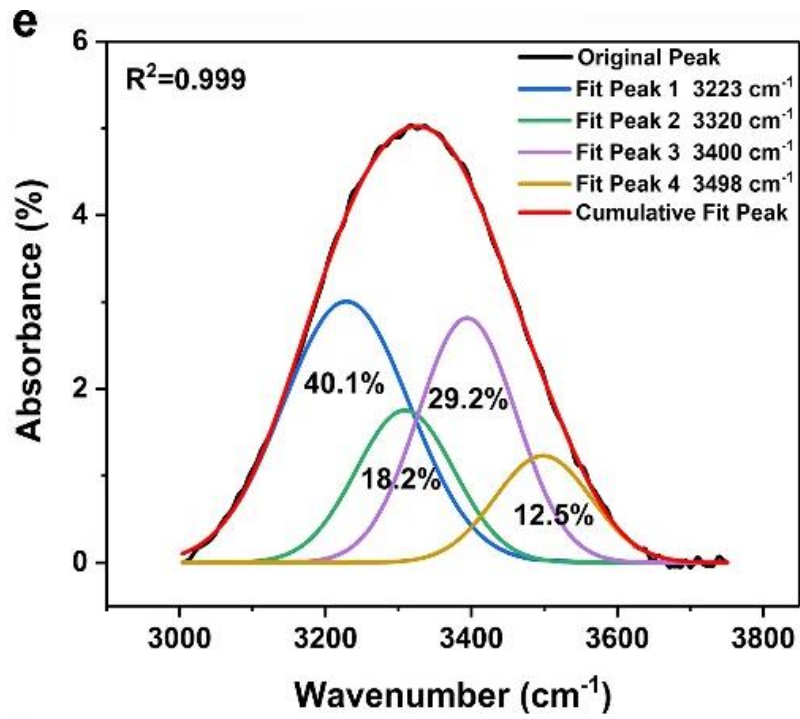


Figure AS10 Snapshots of MD simulation showing the moving trails for a) PVA-20, b) extracted PVA chains and c) extracted water molecules after 1, 99 and 197 ps. The main chain of one chosen PVA is marked in yellow with one carbon atom highlighted in dark blue for showing the movement of PVA chains. Two water molecules are marked in blue for monitoring their movement with time.







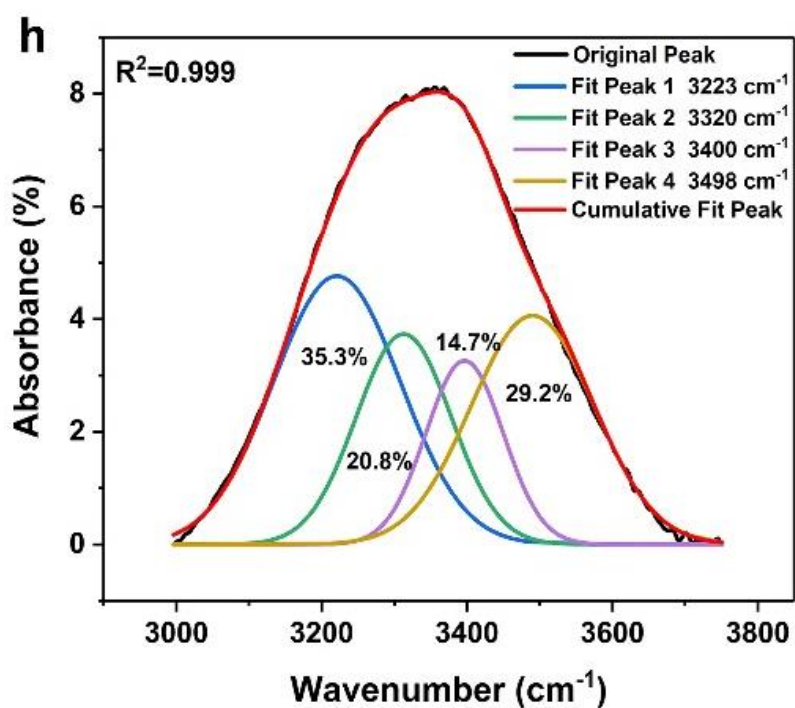
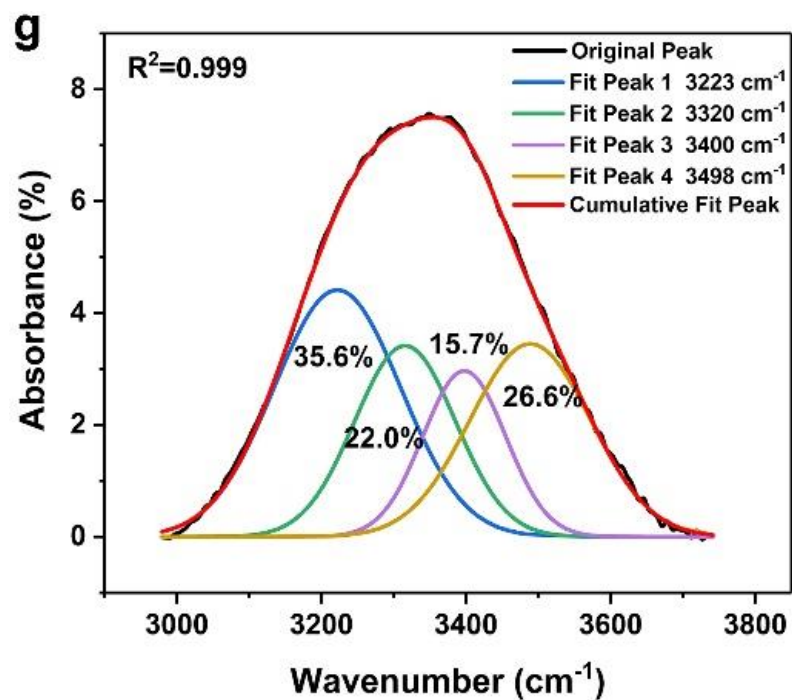


Figure AS11 a) ATR-IR of PVA films with various water content, ATR-IR spectra in the range of 3000-3800 cm^{-1} for b) PVA, c) PVA-1.8, d) PVA-4.9, e) PVA-6.5, f) PVA-8.2, g) PVA-16 and h) PVA-20.

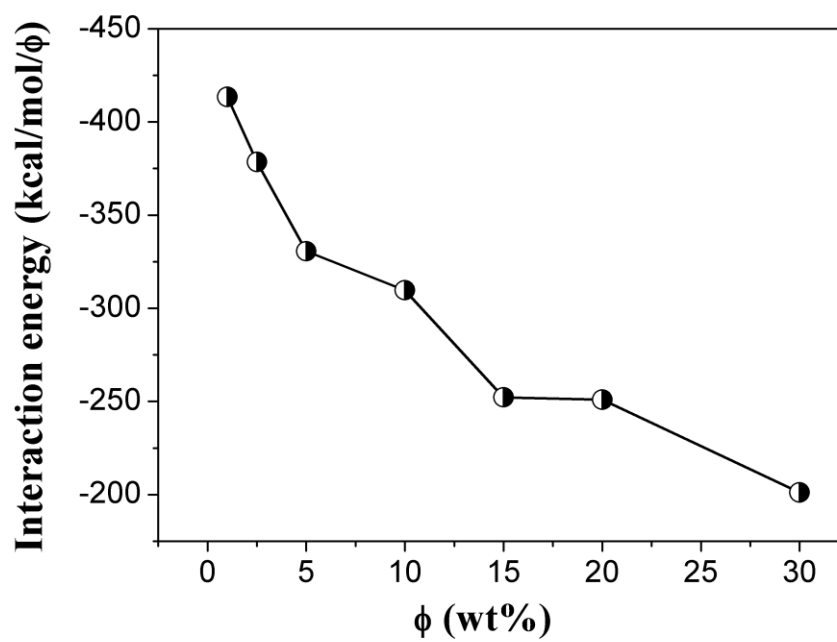


Figure AS12 Interaction energy between the water and PVA chains normalized by the water concentration calculated by MD, showing that the interactions energy decreases with increased water content.

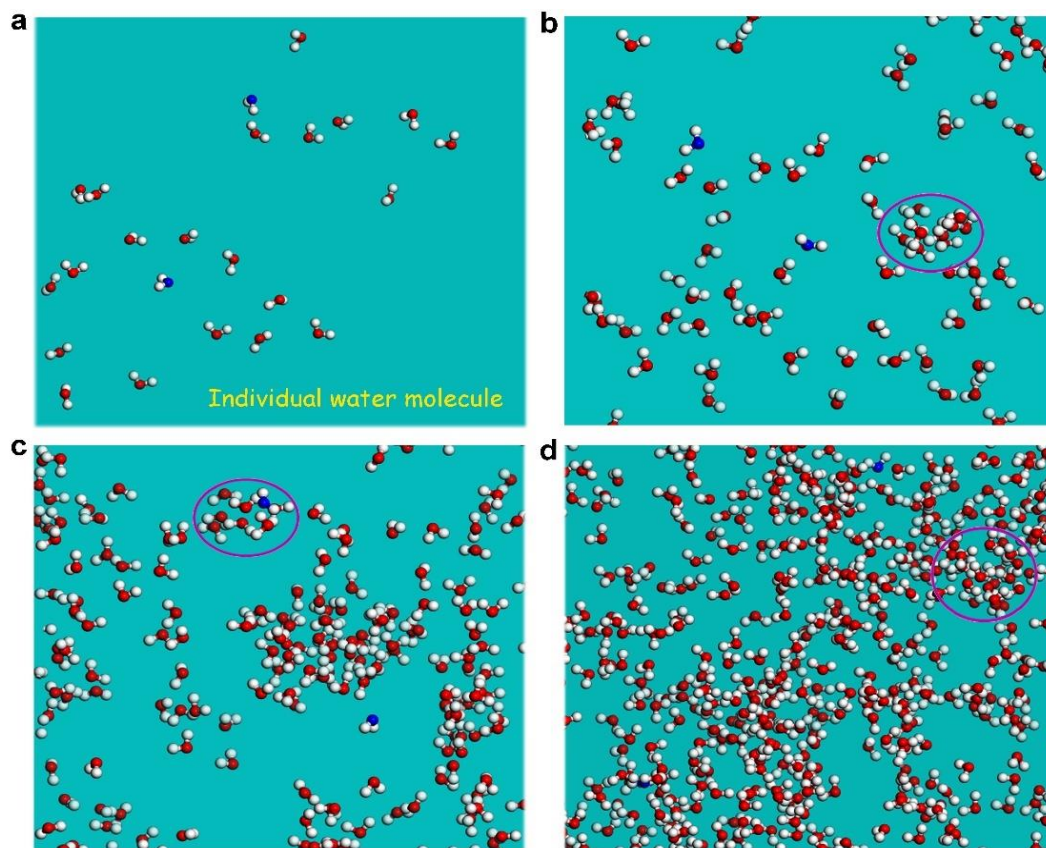


Figure AS13 Snapshots of illustration for the dispersion of water molecules within the PVA matrix. a) PVA-1.0, b) PVA-5.0, c) PVA-10, and PVA-20. When the water content is very low, such as 1 wt%, all water molecules individually disperse, some small water clusters (cycled in dark pink) begin to appear with increased water content, especially at contents above 10 wt%. Water molecules almost form a 3D physical network when the water content is above 20 wt%.

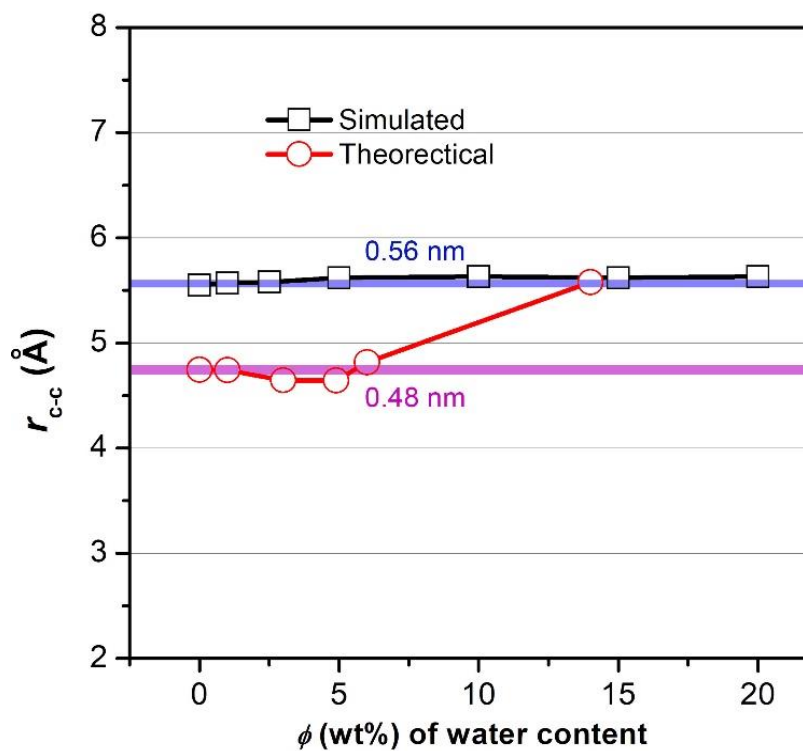
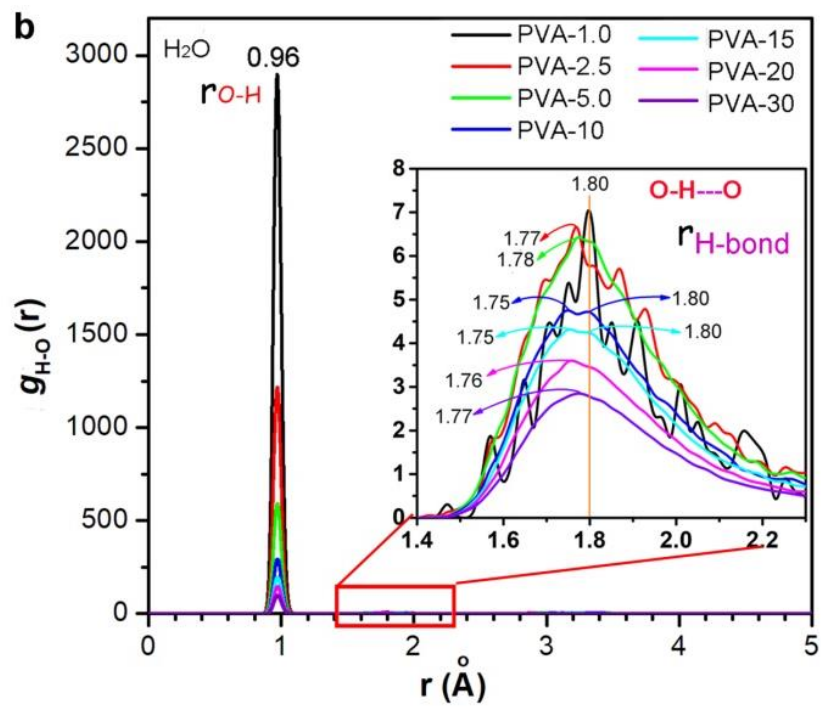
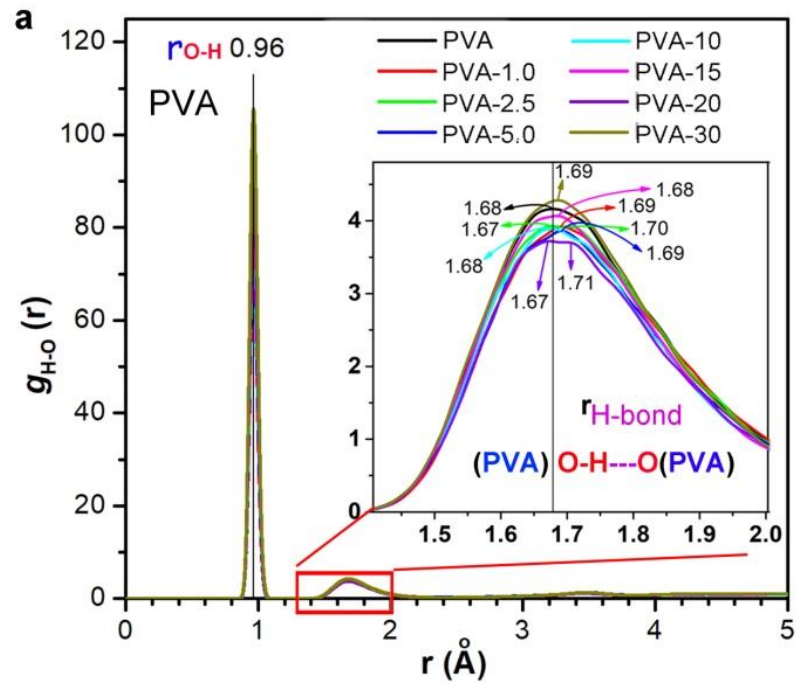


Figure AS14 Distances between PVA chains by MD and by theoretical calculation from the average diameter of free volume holes during PALS tests. The distance between PVA chains slightly increases with increasing water content, but remains a distance range of 0.46-0.56 nm.



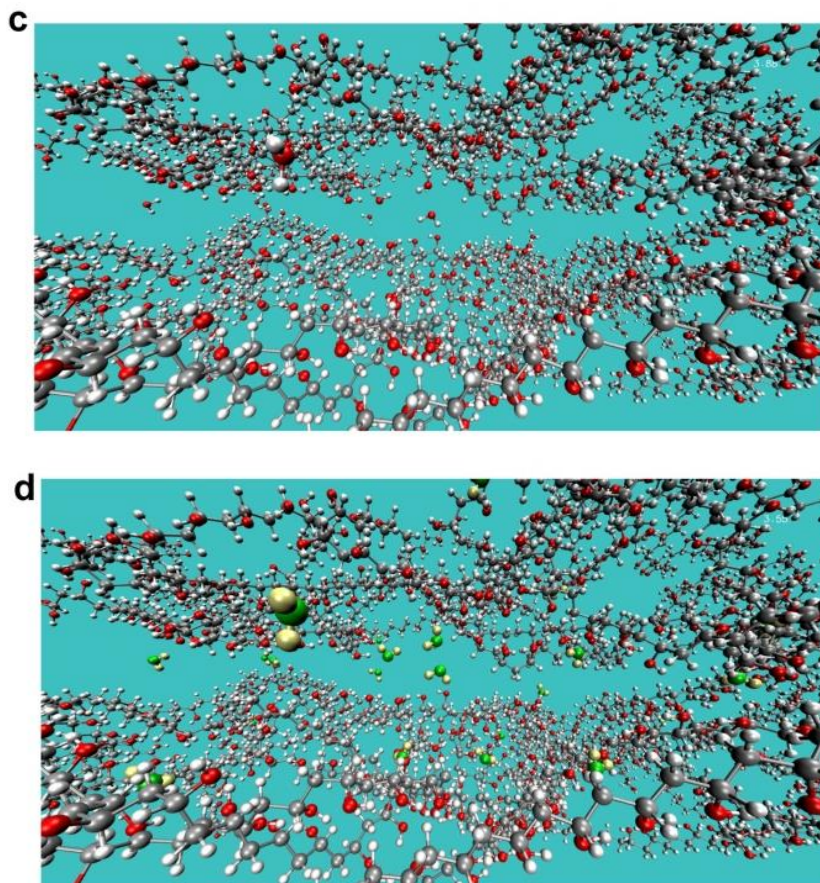


Figure AS15 Radial distribution functions (RDFs) of samples with various water content showing intermolecular distance for a) $g_{H-O}(r)$ in PVA chains, b) $g_{O-H}(r)$ in water molecules.

Illustration for c) dry PVA and d) PVA-water systems.

APPENDIX B

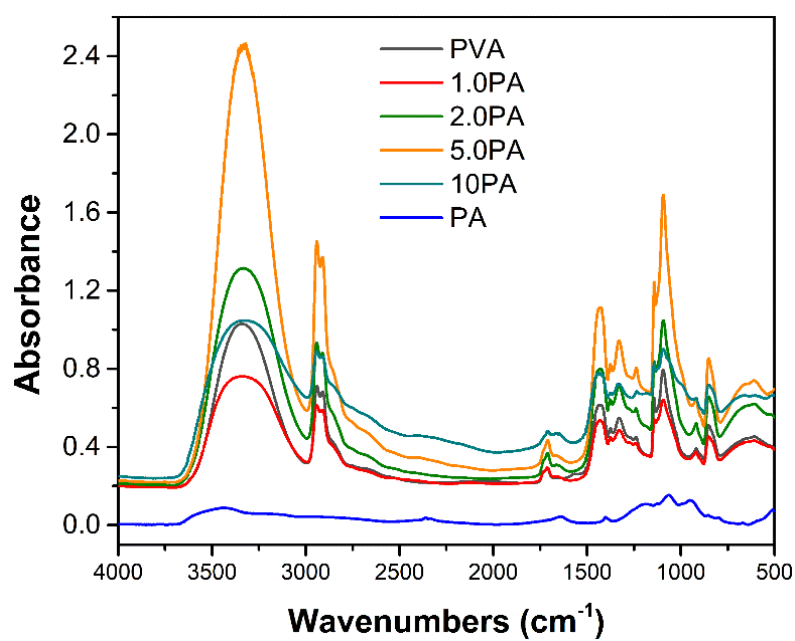


Figure BS1 IR spectra of PVA, PA and their composites.

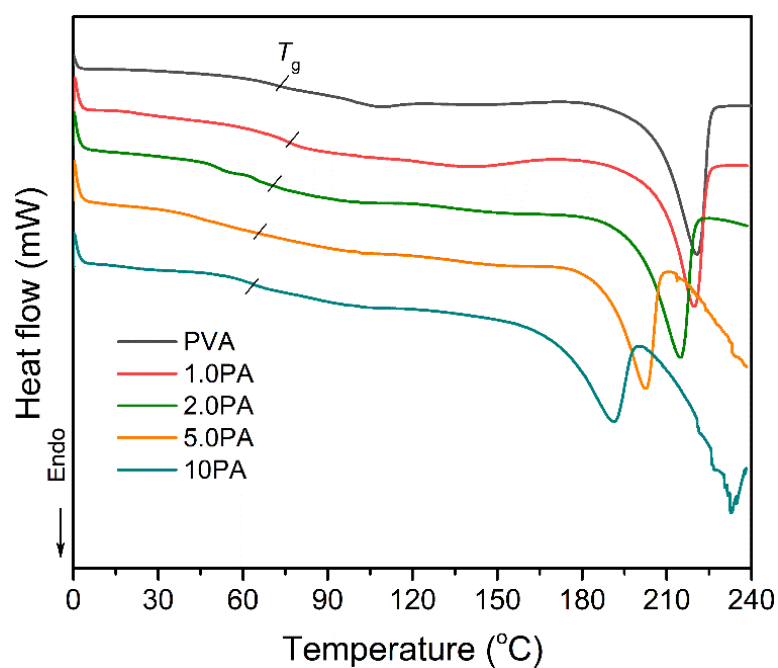


Figure BS2 DSC curves of PVA and its composites based on PA.

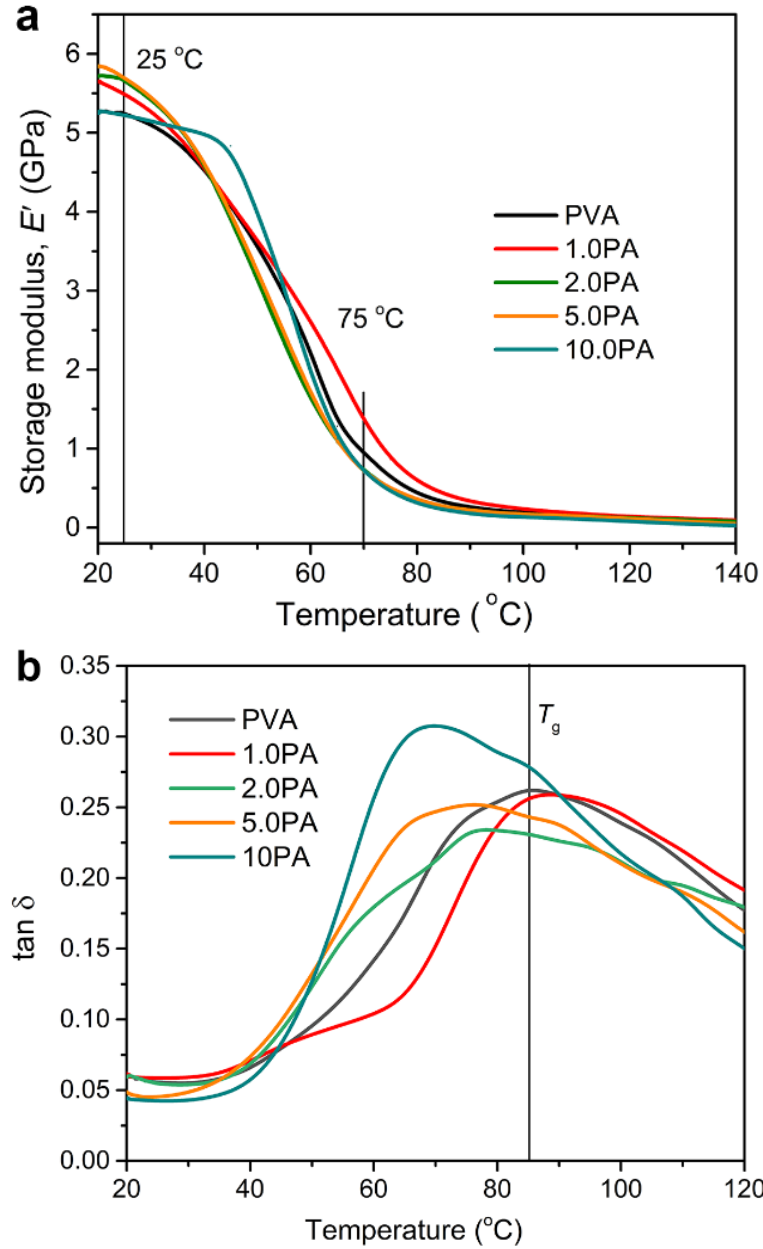


Figure BS3 Temperature dependence of a) storage modulus (E') and b) loss factor of PVA and its PA composite films.

Table BS1 Glass transition temperature (T_g) of PVA and its PA composites obtained by DSC, DMA, and MD simulations.

Run	T_g (°C)		
	By DSC	By DMA	By MD
PVA	72.8	85	
PVA †			74.0
1.0PA	75.6	88.9	
1.5PA †			78.0
2.0PA	69.1	79.2	
2.9PA †			70.0
4.3PA †			65.0
5.0PA	64.6	75.8	
9.6PA †			63.0
10PA	62.3	70.4	

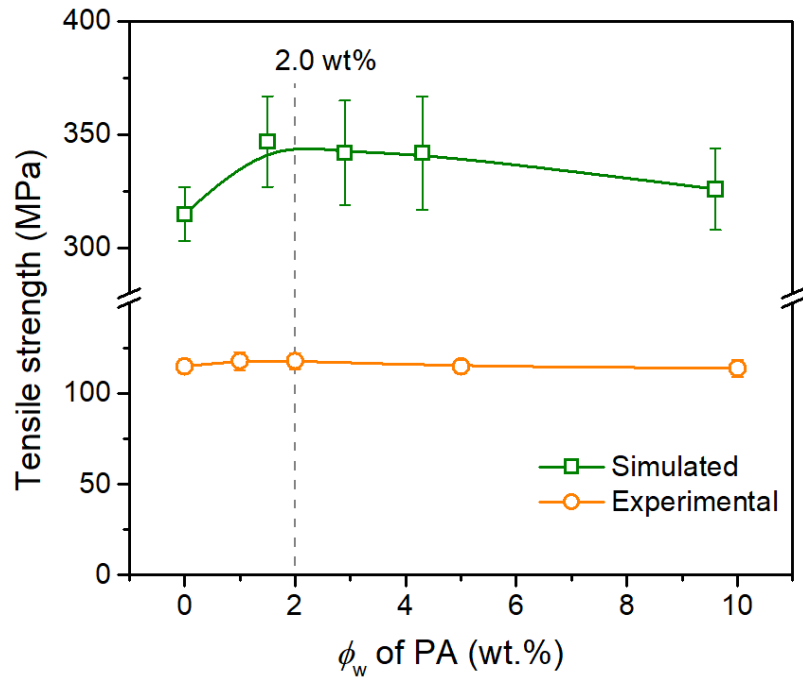


Figure BS4 Tensile strength of PVA and its composites as a function of the PA concentration.